Spring 2011

Synthesis and characterization of nanocrystalline and mesoporous zeolites

Anton Petushkov
University of Iowa

SYNTHESIS AND CHARACTERIZATION OF NANOCRYSTALLINE AND MESOPOROUS ZEOLITES

by

Anton Petushkov

An Abstract

Of a thesis submitted in partial fulfillment
of the requirements for the Doctor of
Philosophy degree in Chemistry
in the Graduate College of
The University of Iowa

May 2011

Thesis Supervisor: Professor Sarah C. Larsen

ABSTRACT

Mesoporous aggregates of nanocrystalline zeolites with MFI and BEA frameworks have been synthesized using a one-pot and single structure directing agent. The effect of different reaction conditions, such as temperature, time, pH and water content, on the particle size, surface area and mesopore volume has been studied. Nanocrystalline and mesoporous ZSM-5, β and Y zeolites were modified with different transition metals and the resulting single- and double metal containing catalyst materials were characterized. Nanocrystalline Silicalite-1 zeolite samples with varying particle size were functionalized with different organosilane groups and the cytotoxic activity of the zeolite nanocrystals was studied as a function of particle size, concentration, organic functional group type, as well as the type of cell line. Framework stability of nanocrystalline NaY zeolite was tested under different pH conditions. The synthesized zeolites used in this work were characterized using a variety of physico-chemical methods, including powder X-ray diffraction, Solid State NMR, nitrogen sorption, electron microscopy, Inductively Coupled Plasma – Optical Emission Spectroscopy and X-ray Photoelectron Spectroscopy.

Abstract Approved: _____
Thesis Supervisor

_____
Title and Department

_____
Date

SYNTHESIS AND CHARACTERIZATION OF NANOCRYSTALLINE AND MESOPOROUS ZEOLITES

by

Anton Petushkov

A thesis submitted in partial fulfillment
of the requirements for the Doctor of
Philosophy degree in Chemistry
in the Graduate College of
The University of Iowa

May 2011

Thesis Supervisor: Professor Sarah C. Larsen

Graduate College
The University of Iowa
Iowa City, Iowa

CERTIFICATE OF APPROVAL

_____

PH.D. THESIS

_____

This is to certify that the Ph.D. thesis of

Anton Petushkov

has been approved by the Examining Committee
for the thesis requirement for the Doctor of Philosophy
degree in Chemistry at the May 2011 graduation.

Thesis Committee: _____
Sarah C. Larsen, Thesis Supervisor

_____
Edward G. Gillan

_____
Vicki H. Grassian

_____
Amanda J. Haes

_____
Aliasger K. Salem

To my parents.

The most exciting phrase to hear in science, the one that heralds the most discoveries, is not 'Eureka!' but 'That's funny'

Isaac Asimov.

ACKNOWLEDGMENTS

First and foremost, I want to thank my parents for supporting my decision to pursue a career in chemistry, and for all the moral support and advices that they were giving to me during my stay in graduate school.

I want to express my deepest gratitude to Dr. Sarah Larsen for being the best research advisor I could only dream of. I truly enjoyed being her student. Thanks to Dr. Larsen I had an opportunity to work on a number of interesting research projects and learn so much about the zeolite chemistry. She has always been very open to any questions and concerns I had. Dr. Larsen's guidance of my research work has been invaluable.

I want to thank Dr. Aliasger Salem for the collaborative work on the zeolite cytotoxicity study and Dr. Christopher Brooks from Honda Research Institute for funding and collaborative study of zeolite nanocrystals as catalysts. These research projects allowed me to learn about very different aspects of the materials I was working with. The later work on a review of silica based materials cytotoxicity further broadened my knowledge and allowed me to learn about the risks associated with handling the zeolite materials. As I was reading the literature on zeolites, I was more and more amazed by the multitude of their applications and the beauty of these materials.

I truly appreciate working with Stacey Zones, Tracy Davis, Anna Jackowski and Lun-Teh Yien during my internship in Chevron Energy Technology Company. Thanks to them I had the most positive experience of working in industrial chemistry environment and I learned tremendously much from them about the preparation and use of zeolite catalysts. My special thanks to Bi-Zhen Zhang who made this internship possible and Charles Wilson, and Robert Saxton for sponsoring it and being great supervisors.

The two people I learned a lot about NMR from are Santhana Velupillai from the Chemistry Department and Dr. Sarah Burton from Pacific North National Laboratory.

They gave me numerous tips on different aspects of using NMR instruments and interpreting data and I truly appreciate their time and effort to teach me so much.

I am thankful to Jonas Baltrusaitis for being patient with me and teaching me to use SEM and TEM. Electron microscopy is not just a very useful method in zeolite study, but also one of the most entertaining, and thanks to Jonas I had a lot of great time using the instruments.

I want to thank my group mates Anamika, Beth, Will, Karna, Ashish, Nicholas, Yulia, and Paul for making my stay in the group enjoyable. I learned a lot from senior and junior group members alike and I appreciate the time we spent together in the lab and out of it. My special thanks to Ram, who helped me to get acquainted with the lab and start the research.

I had a chance to work and mentor several brilliant undergraduate students Suhyoung Yoon, Jasmine Freeman and Giorvanni Merilis, who helped me tremendously with the research. I truly enjoyed teaching these students everything I knew and helping them with all aspects of their research work.

Last but not the least I want to thank my friends Natalia, Alexei, and Sung-Wan, who helped me to settle in Iowa and who I spent great time with. And of course my very very special thanks to Yulia Skvortsova, a fantastic friend and brilliant scientist, who has always been an example for me and who gave me numerous important career advices. I am truly proud to be her friend.

ABSTRACT

Mesoporous aggregates of nanocrystalline zeolites with MFI and BEA frameworks have been synthesized using a one-pot and single structure directing agent method. The effect of different reaction conditions, such as temperature, time, pH and water content on the particle size, surface area and mesopore volume has been studied. Nanocrystalline and mesoporous ZSM-5, β and Y zeolites were modified with different transition metals, and the resulting single- and double metal-containing catalyst materials were characterized. Nanocrystalline Silicalite-1 zeolite samples with varying particle size were functionalized with different organosilane groups and the cytotoxic activity of the zeolite nanocrystals was studied as a function of particle size, concentration, organic functional group type, as well as the type of cell line. Framework stability of nanocrystalline NaY zeolite was tested under different pH conditions. The synthesized zeolites used in this work were characterized using a variety of physicochemical methods, including powder X-ray diffraction, solid state NMR, nitrogen sorption, electron microscopy, inductively coupled plasma – optical emission spectroscopy and X-ray photoelectron spectroscopy.

TABLE OF CONTENTS

LIST OF TABLES

Table

LIST OF FIGURES

Figure

CHAPTER 1

INTRODUCTION

1.1 Zeolites – from discovery to synthesis and application

The first discovery of a zeolite is dated back to 1756 when a Swedish mineralogist Axel Cronstedt observed that heating of the naturally occurring mineral stilbite resulted in its fusion and release of water. Based on this property, Cronstedt named the material zeolite, literally a “boiling stone” from the Greek ζέω (zeō), meaning "boil" and λίθος (lithos), meaning "stone".

It was not until a century later, when synthesis of analcime type zeolite was reported by St Claire Deville in 1862, and was followed by synthesis of several more zeolite structures in the subsequent years. Systematic studies of zeolite synthesis began in the twentieth century and the number of discovered zeolite structures has been growing ever since. Currently, there are about 200 unique zeolite frameworks that have been identified, and over 40 naturally occurring zeolite frameworks are known.

A classical definition of zeolite is a crystalline aluminosilicate with a three-dimensional framework structure that forms uniformly sized pores of molecular dimensions. However, other elements, such as titanium,[1, 2] boron,[3, 4] gallium,[5] germanium,[6] tin,[7] as well as cobalt and manganese[8] have been successfully incorporated into the zeolite framework. Aluminophosphate and silicoaluminophosphate zeolites are a separate family of zeolite materials, some of them with frameworks that do not have aluminosilicate analogs.[9]

One of the most commonly used methods for synthesis of zeolites is hydrothermal treatment (HT). Hydrothermal treatment of zeolites typically occurs in closed autoclave systems, where a mixture of silicon and aluminum sources, structure directing agents, and sources of other elements in water is treated at an elevated temperature and pressure (T > room temperature, P > 1 bar). The upper limit of temperatures is usually around 180 ^{o}C

and is often times dictated by the stability of organic template under reaction conditions. The reaction mixture can be heated in static mode or be stirred at a specific rate. The stirring mode is an important factor for synthesis of some zeolite structures,[10] and on a larger production scale, stirring is crucial for appropriate heat transfer.

Zeolites are commonly synthesized in a highly basic medium in order to facilitate the dissolution of silicon precursors, which sharply decreases at lower pH values. The range of pH values used in synthesis ranges from 11 to 14. The OH^- anions from alkaline and organic structure directing agent hydroxides also act as a mineralizer during the zeolite synthesis. An alternative source of mineralizer instead of hydroxide anions was discovered by Flanigen and Patton, who used fluoride anions to facilitate zeolite synthesis.[11] The fluoride anions were then used by other research groups to synthesize different zeolite structures previously synthesized under hydroxide conditions.[12, 13]

Organic structure directing agents (SDA) have a profound role in zeolite synthesis. The zeolite framework is formed around the organic molecules, so their shape controls the type of zeolite framework formed during the synthesis. The SDAs containing one or two quaternary ammonium groups have found the most widespread use for zeolite synthesis.

In all silica zeolites, the overall charge of the surface is zero, and the formula unit of the material is SiO_2. Introduction of aluminum or another element with valence less than 4 creates a deficiency of positive charge, which needs to be compensated. In high silica zeolites, where the amount of negatively charged surface sites is low, the positive charge on the organic structure directing agent can act as a counter ion. However, the SDA molecules are typically bulky and as the amount of negatively charged sites increases, inorganic cations of alkali metals need to be added to the reaction mixture in order to compensate the excess of negative charge on the surface. This way ion-exchange sites are created on the surface of the zeolite and can be exchanged by a variety of different cations to modify the zeolite properties (Figure 1). Replacing an alkali cation by

a proton is one of the important modifications from the practical standpoint, as it creates Brønsted acidic sites on the zeolite surface (Figure 2A). The degree of acidity depends on the zeolite framework and proximity to other acid sites.[14] Thermal dehydration of zeolites results in release of water and creation of Lewis acid site (Figure 2B).

Acid sites on the zeolite surface exhibit catalytic activity towards a large number of reactions. One of the first catalytic applications of zeolites was in the petrochemical industry, where faujasite zeolite replaced amorphous aluminosilicates in the fluid catalytic cracking (FCC) process.[15] Many more types of zeolite have found catalytic application for hydrocracking, hydroisomerization, catalytic dewaxing, and other reactions. The combination of acid site strength with the pore size and profile offer unique environment around the acid sites that can be tuned for specific catalytic applications. The petrochemical industry is not the only one using zeolite-based catalysts.

Zeolites are being used in the automotive industry in catalytic converter systems for decreasing emission levels of nitrogen oxides (NOx). In a typical three-way catalytic converter metal-exchanged zeolite catalyzes reduction of NOx into nitrogen by using hydrocarbons present in the exhaust fumes as a reducing agent.[16] Finally, zeolite catalysts are evaluated in the pharmaceutical industry for fine chemical synthesis.[17]

The interest in decreasing the zeolite crystal size for applications in catalysis and adsorption lies in microporosity of zeolites. The size of micropores in zeolites does not exceed 15 angstroms, and for the majority of zeolite frameworks is around 5-6 angstroms in diameter. The small pore size poses diffusion limitations in the case of large crystals. Decreasing the crystal size not only shortens the diffusion path lengths but also increases the fraction of the external surface area relative to the total surface area of the zeolite.[18] Active sites located on the external surface are substantially easier to access than the active sites inside the zeolite pore network.[19] The number of synthesized nanoscale

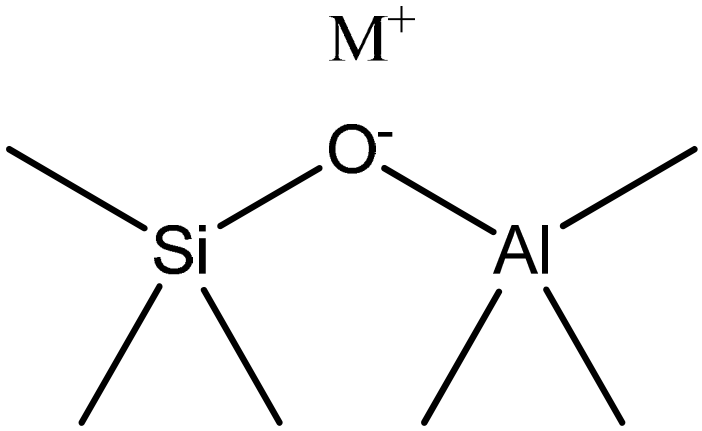

Figure 1. Ion-exchange site on zeolite surface.

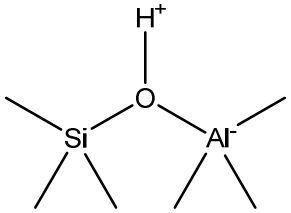

Brønsted
acid site

A

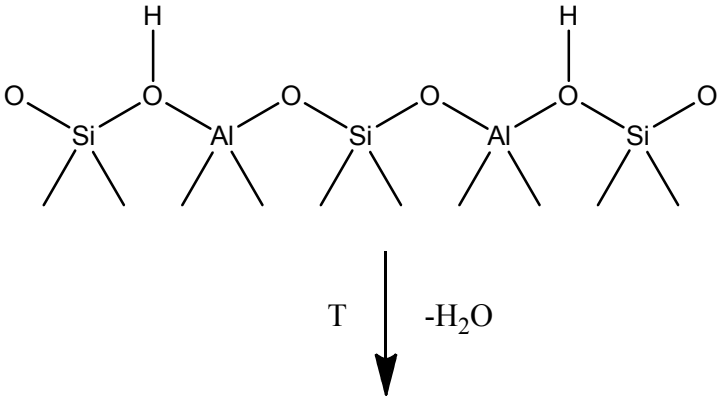

Lewis
acid site

B

Figure 2. Brönsted (A) and Lewis (B) acids sites on zeolite surface.

zeolite structures is limited to LTL,[20] LTA,[21] FAU,[22] GIS,[23] and MOR.[24] Nanoscale MFI (ZSM-5, Silicalite-1)[25-28], BEA[29-31] and FAU[32-34] zeolites have been studied the most widely due to a wide range of reaction conditions leading to the desired framework type.

The model of MFI framework is shown in Figure 3A. MFI zeolite has a relatively high framework density of 18.3 T atoms / nm^3 and a three-dimensional pore system with two intersecting 10-ring pores (Figure 3B). BEA type zeolite is a mixture of several polymorphs of which Polymorph A is the most representative (Figure 4A). BEA zeolite has a significantly lower framework density than MFI zeolite, 15.3 T atoms / nm^3. The three- dimensional pore network consists of two non-intersecting 12-ring pores (Figure 4B). Zeolite Y is a low framework density zeolite (13.3 T atoms / nm^3) with an open pore structure consisting of 12-ring pores with diameter of 7.4 Å that connect supercages of approximately 13 Å in diameter (Figure 5).

Hsu and coworkers reported rapid synthesis of Silicalite-1 (MFI framework) nanocrystals using a two step synthesis route, which consisted of synthesis gel aging at 80 ^{o}C for 10-12 hours followed by rapid crystallization at 170 ^{o}C.[26] The authors noted that reducing the amount of water in the synthesis gel is one of the main factors leading to formation of nanocrystals. Mohamed et al. studied the effect of crystallization times on synthesis of nanosized ZSM-5 and concluded that the zeolite achieved maximum crystallinity after 55 hours. However, it should be noted that crystallization times and crystal growth rates depend on a variety of factors, such as the aging, stirring mode, and the nature of silicon and aluminum sources.[35, 36] Nanocrystalline ZSM-5 zeolites with particle sizes of 15 and 60 nm were synthesized by Song and coworkers by varying the water to silica ratio.[27]

Different approaches to obtaining nanocrystalline zeolite beta were described by several authors.[29-31] Larger amounts of structure directing agent and the use of TEOS instead of fumed silica promote formation of smaller crystals. The type of the structure directing

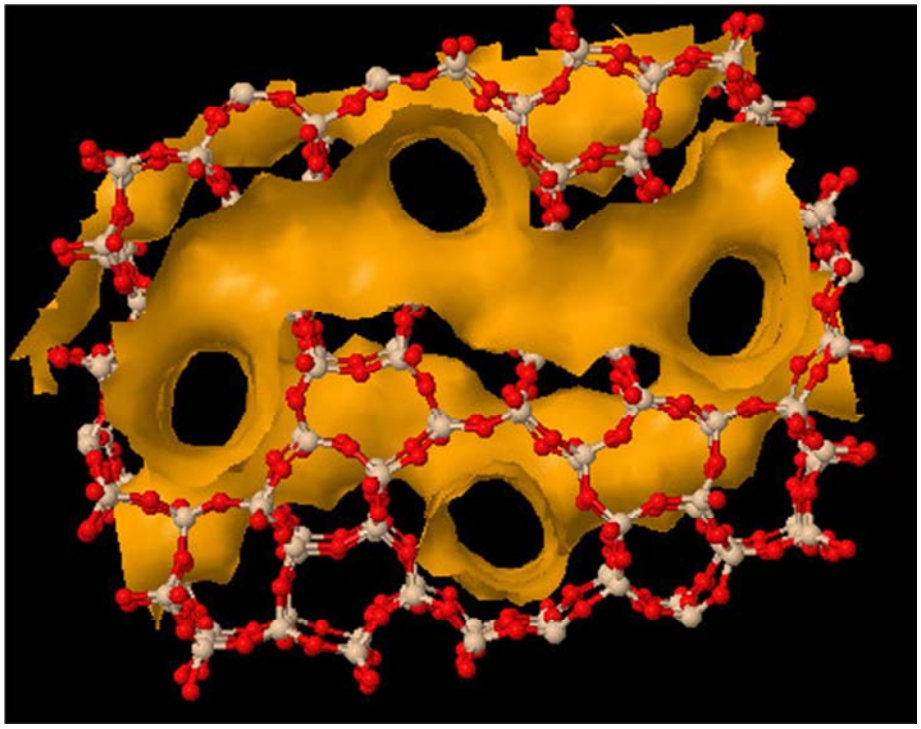

Figure 3. MFI framework type model with pore surface highlighted in yellow (A), and pore profile with diameter in Angstroms (B).

Source: http://www.iza-structure.org

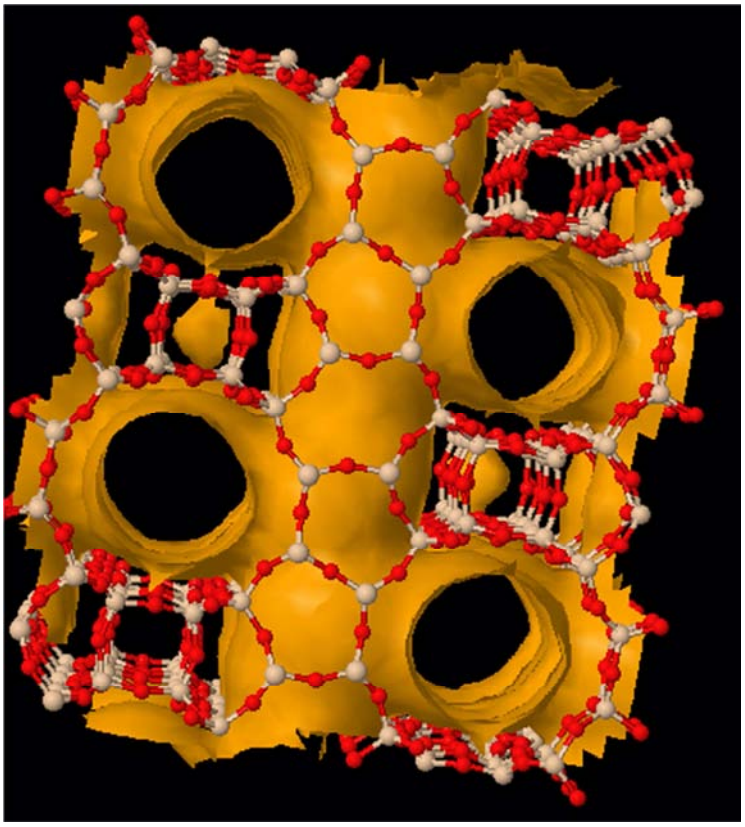

A

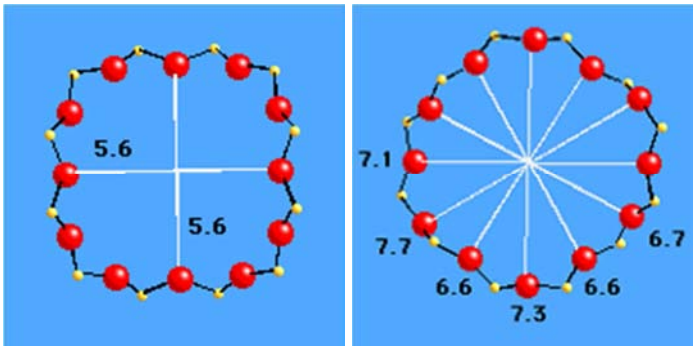

B

Figure 4. BEA framework type model with pore surface highlighted in yellow (A), and pore profile with diameter in Angstroms (B).

Source: http://www.iza-structure.org

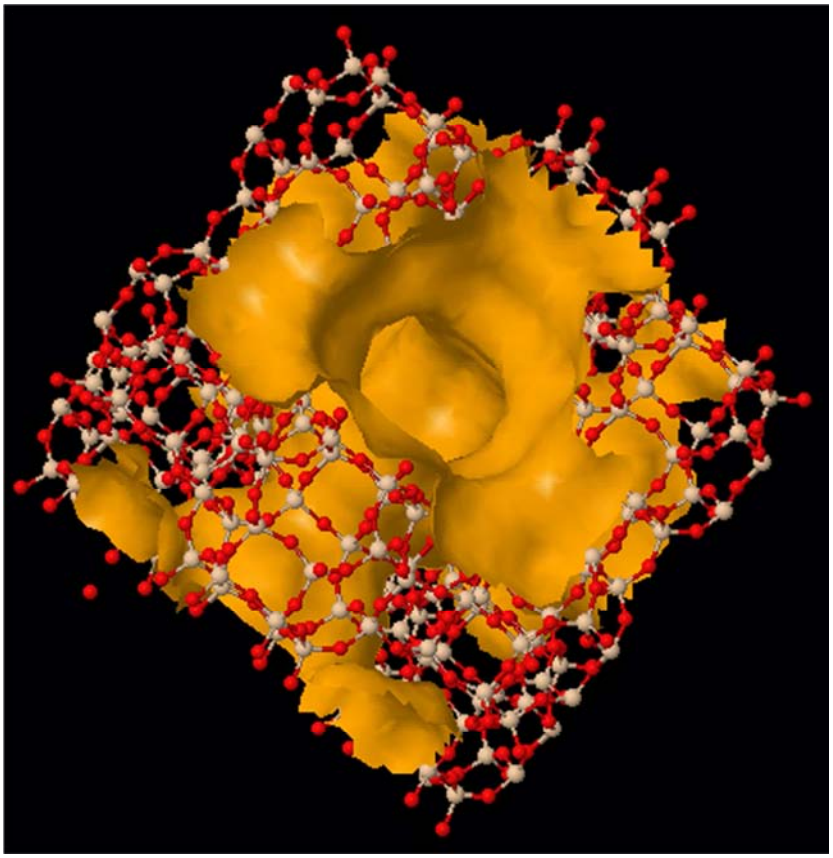
A

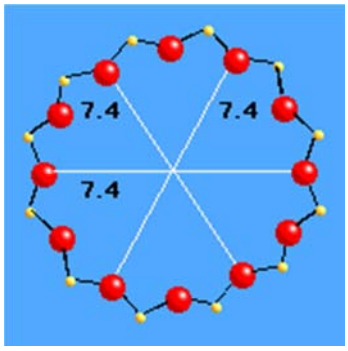

B

Figure 5. FAU framework type model with pore surface highlighted in yellow (A), and pore profile with diameter in Angstroms (B).

Source: http://www.iza-structure.org

agent was also found to affect the crystal size. Smaller crystals were obtained using 4,4`-trimethylenebis(N-methyl, N-benzyl-piperidinium) dihydroxide than in the case of tetraethylammonium hydroxide. Hassanni and coworkers synthesized zeolite L nanocrystals with an average size of approximately 50 nm and controlled the particle size by changing the crystallization time.[20] Covarrubias and coworkers synthesized ZSM-2 zeolite (intergrown EMT / FAU) particles of ~100 nm in size and evaluated the acidity.[37] Tago and coworkers obtained mordenite nanoparticles with ca. 80 nm size by using Polyoxyethylene-(15)-oleylether surfactant and showed that the particle size and morphology can be controlled by changing the concentration of the surfactant.[24] Jung and coworkers reported synthesis of titanosilicate TS-1 (MFI framework) nanoparticles under 100 nm in size and used them to make transparent zeolite films.[38] Yang and coworkers studied the synthesis of zeolite A in presence of a platinum complex and concluded that increasing the platinum content results in a smaller crystal size, and at ~4 wt. % platinum the crystals become nanoscale.[21]

1.2 Metal Exchanged Zeolites: Synthesis and Application.

Modification of zeolites with different metals is a widely used practice for making materials with a wide range of applications.[39-44] Metals located in the zeolite pores exist in different forms depending on the application requirements:

1. Elemental;[45]
2. Cationic;[41, 42, 46]
3. Oxide;[44, 47]

The two most commonly used methods for introducing metals into zeolites are ion-exchange and wet impregnation. The ion-exchange process typically consists of immersion of a zeolite in the solution containing the target metal ions followed by separation of the solid material. Ion-exchange is repeated multiple times in order to achieve the maximum degree of substitution by the target metal cations. Lastly, the solid

material is extensively washed to remove of the excess of the metal salt located inside the zeolite pores. Despite the wide use of ion-exchange, there are cases when this approach is not effective and does not provide sufficient metal loadings. Such cases include the low exchange capacity typical for high silica zeolites,[48] zeolites without ion exchange sites,[49] and the use of neutral or negatively charged metal complexes.[50, 51]

In these cases, the wet impregnation technique is required for achieving the desired amounts of metal. Wet impregnation of zeolites is usually done using small volumes (100-150 % relative to the volume of the solid is common) of solutions containing the target amount of metal. The resulting slurries are allowed to equilibrate and uniformly distribute the solution across the zeolite surface followed by removal of solvent, for example by rotary evaporation. Because of the absence of a washing step, controlling the concentration of metal in the zeolite is straightforward. However, there is a caveat associated with the impregnation technique. There have been reports indicating that wet impregnation results in larger degree of metal particle aggregation.[52] In this case, the calcination and / or reduction procedure needs to be carefully considered. Kubo and coworkers showed that the temperature at which Pt-loaded zeolite 13Y was calcined prior to reduction affected the distribution of platinum clusters in the material.[53] Nie and coworkers employed a deposition precipitation method for loading zirconium into zeolite-beta and achieved better dispersion than in the case of wet impregnation.[54]

Preparation of zeolite catalysts containing two or more metals adds another level of complexity associated with achieving the homogeneity of bimetallic clusters and controlling the ratio between the metals. In the case of high alumina zeolites, the ion-exchange can be carried out simultaneously or successively. In high silica zeolites, which have low exchange capacity, the ion-exchange process is competitive and it is more difficult to control the final ratio between the metals.

The majority of metal-loaded zeolites are used in different catalytic processes. Li and coworkers prepared cesium-impregnated zeolite X and evaluated the catalytic

activity of the material for the isomerization of butane.[55] The authors proposed that cesium exists in the form of oxycarbonate form. Loiha and coworkers studied the hydrogenation of toluene using a bimetallic Pt-Pd-loaded zeolite beta catalyst.[56] Conversion of citral into menthol using a Zr-loaded zeolite beta was studied by Nie and coworkers.[54] Multiple studies of deNOx activity were conducted for Fe-ZSM-5,[57] Pd-ZSM-5,[58] Ag/Na-ZSM-5,[59] and Cu-ZSM-5 zeolites.[60]

One of the less conventional applications of metal containing zeolites include their use for hydrogen storage.[61, 62] Hydrogen storage capacity of several alkaline and alkaline-earth metal exchanged low silica zeolites was studied by Langmi et al.[61] The authors concluded that the metal loading, which depends on the exchange capacity of zeolites, correlated with hydrogen uptake. It was hypothesized that the metal ions act as adsorption sites for hydrogen molecules. Ramirez-Cuesta used inelastic neutron scattering to investigate hydrogen molecules adsorbed on copper-exchanged ZSM-5 zeolite.[62]

1.3 Surface Modification of Zeolite Surface.

Surface modification of zeolites with different organic groups is a powerful technique for tuning zeolite properties such as hydrophobicity,[63] surface charge,[64] prevention of irreversible aggregation,[65] and reactivity[66, 67 68] for a variety of applications, such as fluorometric analysis,[69] gas separation,[70] fluorescent materials[71] and for environmental applications.[67] Modification of zeolite surfaces with organosilanes or organic groups occurs through reaction between silanol groups and organic molecules.[72] Silanization reactions in non-aqueous solutions involve several steps.[73] First, organosilane molecules physisorb on the surface of zeolites. Then, residual water molecules present on the zeolite surface facilitate hydrolysis of silanes. The surface silanol groups then react with OH groups on the silane via an SN_2 mechanism and their condensation occurs resulting in the release of a water molecule (Figure 6).

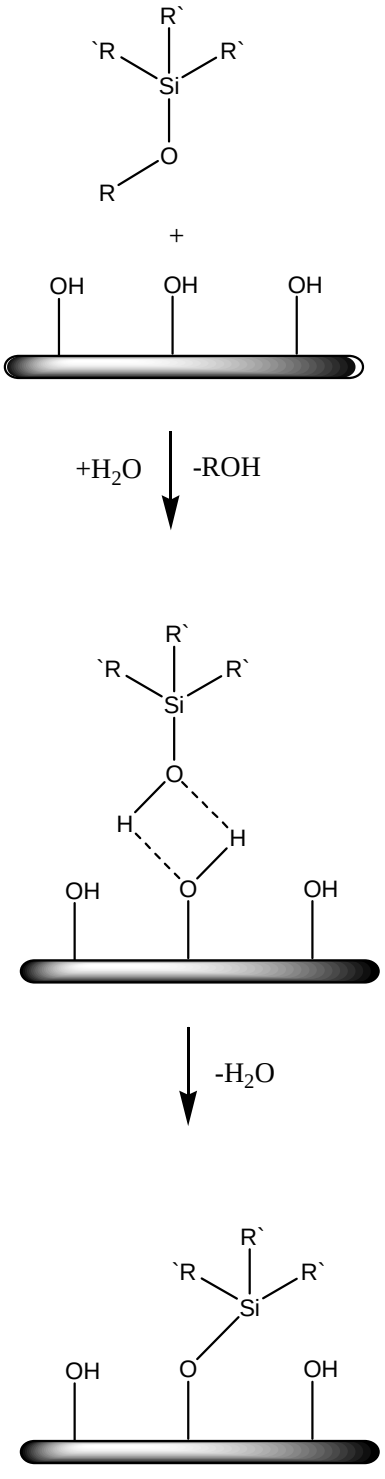

Figure 6. Scheme of zeolite surface functionalization.

The external surface of zeolites possesses a large number of silanol groups, whose concentration depends on the zeolite type. 2.3 terminal OH groups / nm^2 of external surface were found for NaY zeolite.[74] For MFI type zeolite the silanol group concentration on the external surface is approximately 4 OH / nm^2.[75] The internal surface of zeolites originates from the presence of micropores. In the case of defect free zeolites, no silanol groups are present in the pore network.[76] Zeolites synthesized under hydroxide conditions typically have numerous defects on the pore walls and thus allow for internal surface modification.[75] While the amount of silanol groups on the internal surface depends on the number of defects, the amount of available external surface per unit mass dictates the maximum theoretically attainable surface concentration of organic groups.[75]

Another important factor that influences the surface concentration of silanol groups is calcination, which is required for removal of structure directing agent molecules from the zeolite pore network. Zhuravlev showed that the silanol groups can collapse and form siloxane groups under high temperature conditions.[77] This conversion is reversible, and the siloxane groups can be rehydroxylated back into silanol groups.

Molecular size of the silanes also needs to be taken into account. Larger bulky molecules may render some of the silanol groups inaccessible for silanization.[78] Silane molecules that can form multiple bonds, e.g. 3-aminopropyltriethoxysilane (APTES), can anchor to the zeolite surface forming bonds with more than one silanol group, thus decreasing the total maximum concentration of organosilane. In this case, alternatives like 3-aminopropyldimethyl-methoxysilane (APDMMS) can be used, since APDMMS only has one methoxy group than can interact with the surface.

Surface functionalization with alkylamine or alkylthiol groups opens doors to further functionalization. Smaiehi et al. showed that zeolite-beta nanoparticles' functionalization with aminoalkyl groups can be used for further functionalization with more complex organic moieties with fluorescent properties.[65] Zhan and coworkers used a alkylamine functionalized nanosized faujasite crystals for poly(ethylene glycol) methyl

ether grafted polymethacrylate (PEGPMA) polymer, which has a potential application as a solid polymer electrolyte.[79]

Sen and coworkers developed an optically active material, in which the surface of nanoscale zeolite Y particles was functionalized with mercaptopropyl groups that served as anchors for gold nanoparticles, and an organic dye located in the pore network of the zeolite.[80]

1.3 Thesis overview

The research work described in this thesis focuses on studying the synthesis conditions and properties of new zeolite based materials with improved properties. Chapter two of the thesis describes the characterization techniques used in the studies including the background information about these methods used, as well as some practical aspects of sample preparation for the analysis.

Synthesis of mesoporous zeolites with two different frameworks and the experimental conditions required for obtaining high mesoporosity and external surface area are described in Chapter 3. One goal of the research was to find a simple and fast way to synthesize zeolite nanocrystals assembled into mesoporous aggregates. Nitrogen adsorption isotherms were used to measure the surface area and pore volume of the synthesized mesoporous zeolites. Electron microscopy tools complement the data obtained using adsorption techniques and provide information about the size and morphology of mesoporous aggregates. It was shown that by adjusting the reaction parameters, the degree of mesoporosity and the crystal size can be changed. The morphology of mesoporous aggregates is different for ZSM-5 and β zeolites. Smaller primary crystals and larger aggregates were obtained for ZSM-5, while the difference between the primary crystal size and the aggregate size was smaller for zeolite β.

Preparation of catalyst materials using nanocrystalline and mesoporous ZSM-5, β and Y zeolites is discussed in Chapter 4. Several single- and double metal-exchanged

zeolite samples were prepared and the effect of metal loading was studied. Zeolites with significant difference in Si/Al ratio (for example ZSM-5 and Y) appear to have different selectivity during the ion-exchange process, so the ratio between the metal ions in the solutions needs to be carefully considered. The metal loadings constituted up to several weight percent and did not result in significant changes of accessible surface area and pore volume.

The increasing interest in using zeolite nanocrystals for biomedical applications poses questions about the zeolite toxicity and stability when it is introduced into a human body. Preparation, physico-chemical characterization and cytotoxicological study of silicalite-1 nanocrystals with three different particle sizes, three types of organic functional groups is shown in Chapter 5. Two types of cell lines were used in the study and the dosage of zeolite was varied as well. The study revealed a complex dependence of cytotoxic activity on the aforementioned parameters. Different types of cells have different maximum size limits of particles that can be internalized. Among other factors, the toxicity of carboxypropyl functionalized zeolite crystals was linked to an increased generation of reactive oxygen species.

Framework stability of NaY zeolite which has one of the most open pore networks and largest pore size is discussed in Chapter 6. Stability of NaY nanocrystals was studied as a function of pH, from near neutral pH of 7.4 to highly acidic pH of 1. The choice of the pH range was dictated by the values typical for cell and tissue pH as well as for gastrointestinal tract. The zeolite was shown to be stable with very small amounts of silicon and aluminum released in the aqueous solution at pH 7.4, while the increase of acidity results in lower framework stability due to hydrolysis of Al–O bonds.

Chapter seven describes the conclusions made in the course of the research work, as well as proposals for the future work on nanocrystalline and mesoporous zeolites.

CHAPTER 2.

PHYSICOCHEMICAL CHARACTERIZATION.

2.1 Powder X-ray Diffraction.

X-ray diffraction is a nondestructive technique that is widely used for structure determination of crystalline materials. The basis for X-ray diffraction is the property of electromagnetic radiation. When an X-ray beam propagates through a substance, three types of scattering occur:

1. Coherent scattering produces beams with the same energy as the incident beam;
2. Incoherent scattering produces beams with lower energy due to its partial loss;
3. Absorption of X-ray beams followed by electron emission;

While the two latter effects are typically not significant, coherent scattering is the primary source of X-ray beams scattered from periodic lattices in a crystal.[81]

Periodic lattices in crystals can be treated as semi-transparent mirrors, from which x-ray beams are reflected. In this case, reflection denotes an intensive beam resulting from constructive interference between the scattered X-ray beams. In Figure 7, one X-ray beam reflects from the upper plane and another X-ray beam reflects from the plane immediately below. The reflected X-ray beams will differ in their path length by the distance between the two planes, and the net difference between the planes can be calculated as:

$$AB + BC = 2d\sin(\theta) \qquad (1)$$

where θ is the glancing angle. Most of the X-rays reflecting from the planes will have the path length difference not equal to an integer number of their wavelength and therefore lead to a destructive interference. Those X-ray beams that have their path length difference equal to the integer number of their wavelength will result in a constructive

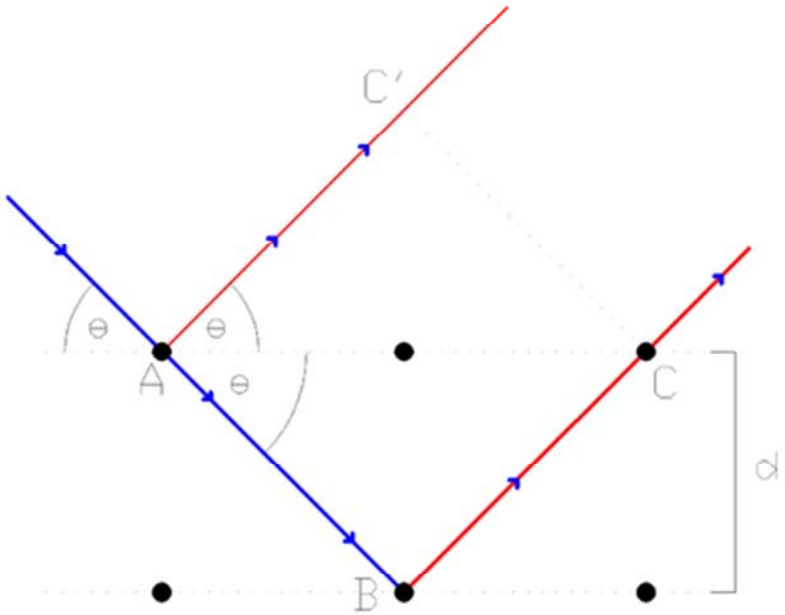

Figure 7.Representation of Braggs's law. The blue line represents the incident X-ray beam, while the red lines represent the scattered X-ray beams.

---

http://www.scientific-web.com/en/Physics/Optics/BraggsLaw.html

interference. In other words, a reflection should be observed when the glancing angle satisfies Bragg's law:

$$n\lambda = 2d\sin(\theta) \qquad (2)$$

Reflections with n = 2, 3, 4 are called second-, third-order and so on. Bragg's law can be rewritten as:

$$\lambda = 2d\sin(\theta) \qquad (3)$$

Therefore, by knowing the wavelength of the X-ray beam and the glancing angle, the distance between the lattice planes can be calculated.

X-ray diffraction is widely used for analysis of crystalline powders. Each crystalline material produces a pattern of reflections, which position (in 2θ degrees) reflects the distance between atomic planes in the crystals. The position and relative intensity of the lines in an X-ray diffraction pattern serve as a fingerprint for a given type of crystalline material. By comparing an X-ray diffraction pattern against the patterns collected for known crystalline compounds, the composition of the analyzed material can be determined.

In addition to phase determination, powder XRD patterns can be used to estimate the crystal size in a powder material.[82] As the particle size decreases, the reflections in the XRD pattern will be broadened. This correlation is used in Scherrer's equation to calculate the particle size τ:

$$\tau = \frac{K \cdot \lambda}{\beta \cdot \cos\theta} \qquad (4)$$

where K is the shape factor (K=1 for spherical particles), λ is the X-ray wavelength (1.5418Å in the case of Cu Ka radiation), β is the line width at half the maximum (FWHM), and θ is the Bragg angle. The particle size determined using Scherrer's equation should be used with caution, as multiple factors beside the crystallite size contribute to broadening of the reflections in XRD patterns. In the case of partially

intergrown crystallites Scherrer's equation underestimates the particle size when compared with electron microscopy analysis.

Another useful piece of information about the analyzed material that can be determined from a powder XRD pattern is its crystallinity. Materials that have a certain amount of amorphous impurity will have lower reflection intensities relative to a purely crystalline material. This way, an XRD can be collected for the analyzed material and for a highly crystalline external reference material of the same crystal structure. Then, after a background correction, the heights or areas or similar reflections of the analyzed material (I) and the reference (I_{ref}) can be compared and relative crystallinity (RC) calculated:

$$RC = \frac{I}{I_{ref}} \cdot 100\% \qquad (5)$$

Identical amounts of analyzed and reference material packed in a similar way in the sample holder need to be used for precise measurements of relative crystallinity. A standard procedure for measuring relative crystallinity of MFI type zeolite has been reported.[83] For relative crystallinity measurements of powders with larger sized crystals, peak height can be used. Nanoscale crystals exhibit peak broadening, and using the areas under respective peaks is preferred.

Figure 8, Figure 9, and Figure 10 show representative patterns of ZSM-5, Naβ, and NaY zeolites, respectively. The reflections filled in red are used for calculations of RC, and the insets contain the magnified reflections. The choice of reflections for relative crystallinity calculations is commonly based on their intensity, as the reflections with higher intensity provide a more accurate RC value. Another precaution is the absence of reflections from possible crystalline impurities, such as other zeolite phases or layered silicates that can overlap with the reflection chosen for RC measurement.

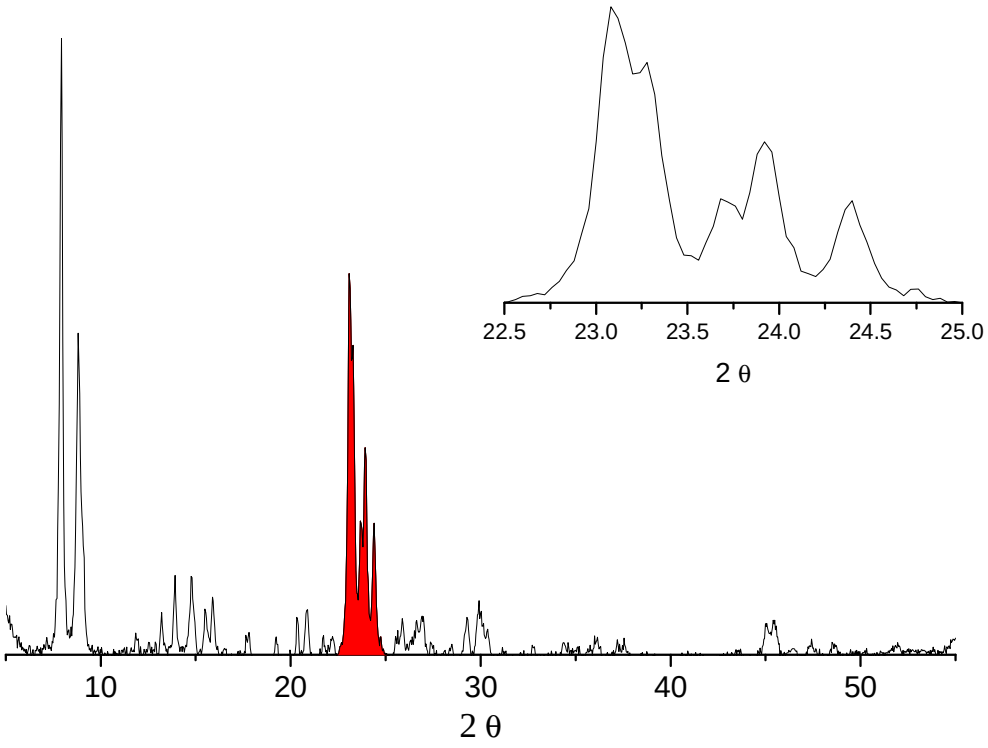

Figure 8. Representative pXRD pattern of ZSM-5 zeolite (MFI framework). The inset shows the range of 2θ integrated for relative crystallinity calculation.

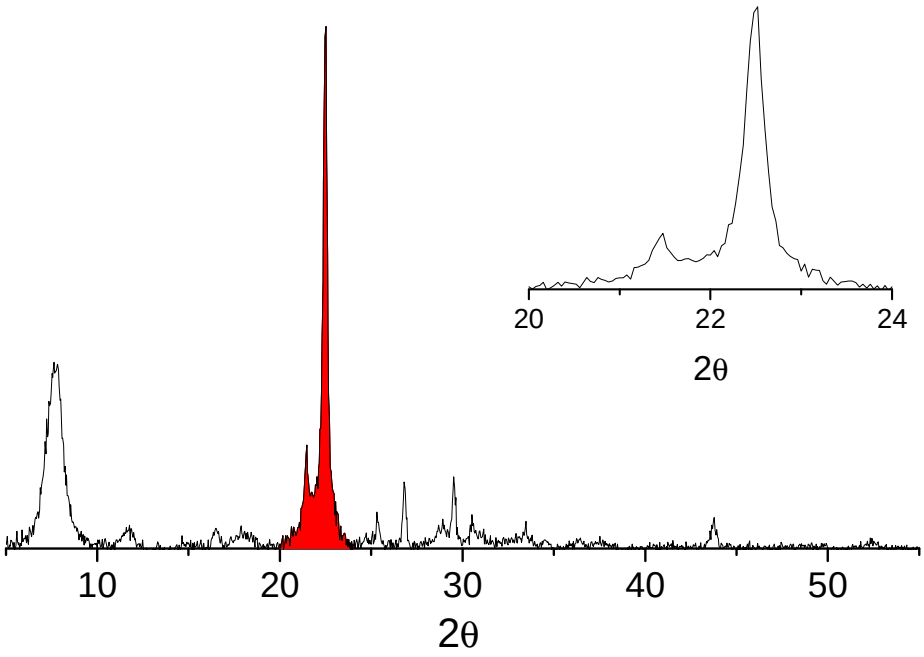

Figure 9. Representative pXRD pattern of Naβ zeolite (BEA framework). The inset shows the range of 2θ integrated for relative crystallinity calculation.

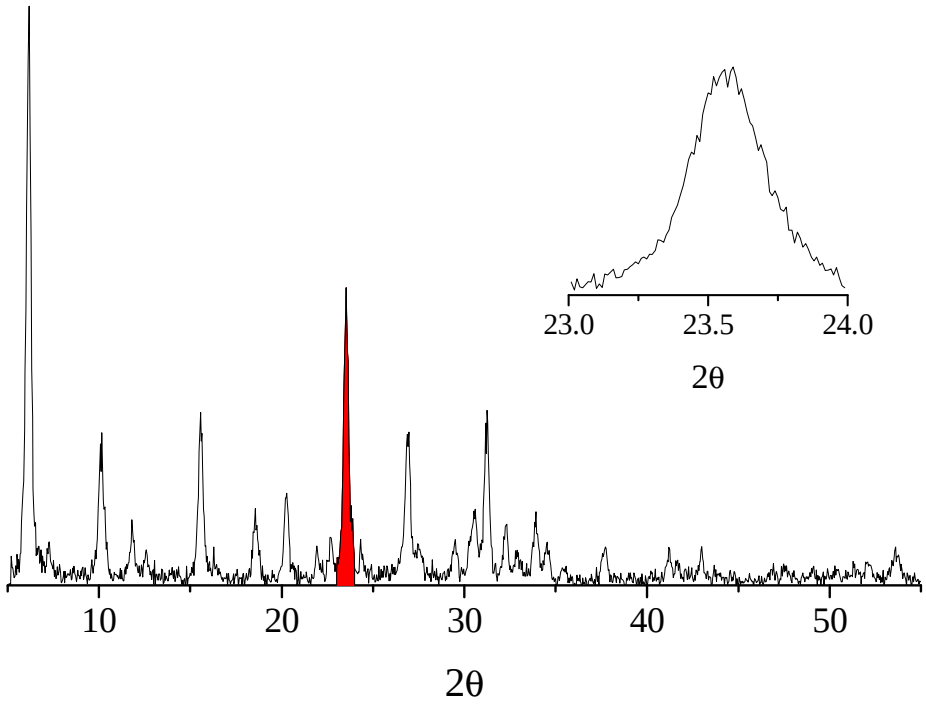

Figure 10. Representative pXRD pattern of NaY zeolite (FAU framework). The inset shows the range of 2θ integrated for relative crystallinity calculation

2.2 Nitrogen adsorption isotherms

Adsorption of gases on the surface of a porous material provides crucial information about the surface area, pore volume and pore size distribution. The basis for adsorption measurements is physisorption of gas molecules on the surface. Physisorption is a van der Waals type of interaction (dispersion or dipolar) between the adsorbate and the substrate. Physisorption interactions are weak, on the order of 20 $kJ \cdot mol^{-1}$, so the gas molecules easily adsorb and desorb from the surface, and the surface coverage increases at lower temperatures.

For surface area measurements, a BET isotherm, developed by Brunauer, Emmet and Teller is commonly used:[84]

$$\frac{V}{V_{mon}} = \frac{c \cdot z}{(1-z)((1-(1-c)z)} \qquad \text{with } z = \frac{p}{p_0} \tag{6}$$

where p and p_0 are the equilibrium and saturation pressures, V_{mon} is the volume of adsorbate required for forming a monolayer on the substrate surface, and c is the BET constant.

c is a constant which is large when the enthalpy of desorption for the surface is larger than the enthalpy of desorption of the liquid adsorbate:

$$c = \exp\left(\frac{E_1 - E_L)}{RT}\right) \tag{7}$$

where E_1 is the heat of adsorption of the first layer and E_L is the heat of adsorption of subsequent layers.

By knowing the volume of adsorbed gas, which is required to form a monolayer on the surface and the area which each gas molecule occupies, one can calculate the surface area. The adsorbates usually used for surface area measurements are nitrogen and argon that have a cross section of 0.162 nm^2 and 0.138 nm^2 respectively. In the case of zeolite materials, external and total surface areas are determined by collecting a BET

isotherm for the sample before and after calcination. Internal surface area can then be calculated as the difference between the total and external surface areas.

The micropore volumes of zeolites can be determined using a t-plot method, developed by Lippens and DeBoer.[85] This method consists of a comparison of the amount adsorbed with the statistical thickness of the adsorbed layer of a known reference isotherm at the same relative pressure.

The total pore volume is calculated by measuring the volume of nitrogen adsorbed at p/p_0 near unity. At this relative pressure, adsorbate is assumed to be condensed inside the pores of the zeolite. The measured total pore volume of zeolite is larger than the micropore volume due to condensation of adsorbate in the intercrystalline voids between zeolite crystals, or, in the case of hierarchical zeolite, in the mesopores. Thus the total pore volume is often assumed to be the sum of micropore and mesopore volumes in the case of hierarchical zeolite materials.

The distribution of pore volumes with respect to the pore size is called a pore size distribution. For pore size distributions, the pore geometry, such as cylindrical, spherical or slit shape, needs to be taken into account. BJH model for pore size distribution measurements assumes a cylindrically shaped pore. The BJH model assumes that condensation of adsorbate in pores of smaller diameter occurs at lower partial pressures and larger pores are filled with adsorbate as the pressure increases. Conversely, adsorbate desorbs from pores of larger size as the partial pressure decreases.[86]

A representative nitrogen sorption isotherm is shown in Figure 11. The first seven data points of the adsorption branch are used for BET surface area calculation. The highest adsorption point is used for calculations of the total pore volume. For pore size distribution modeling the adsorption, desorption or both curves can be used depending on the model. *t*-plot micropore volume calculation uses the low and mid-pressure section of the adsorption branch.

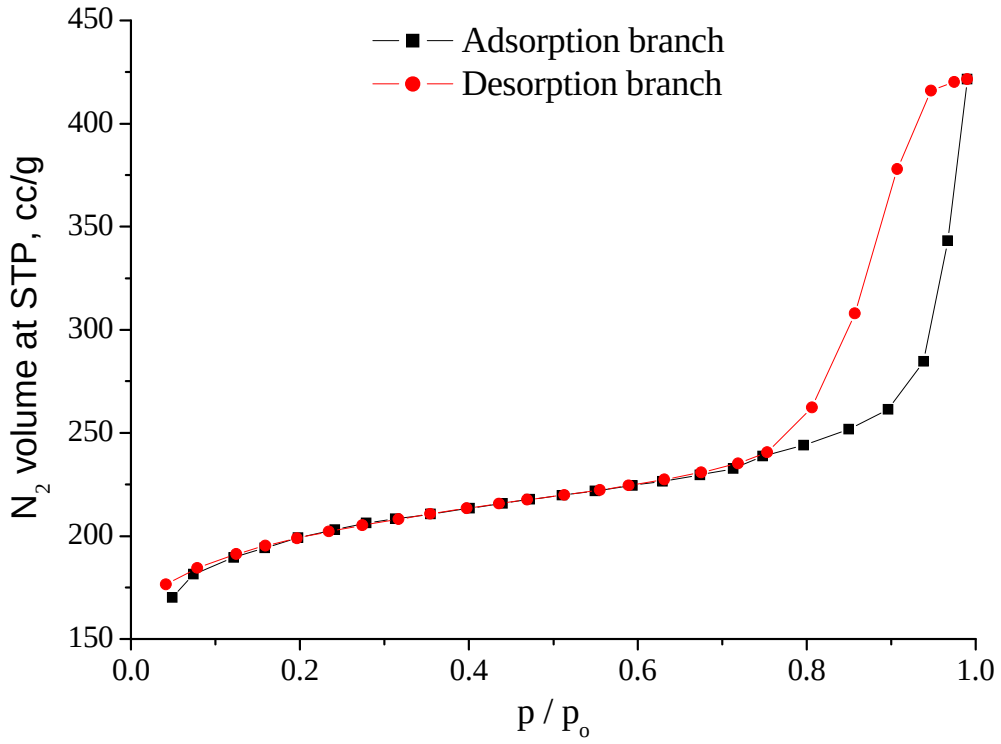

Figure 11. Representative nitrogen sorption isotherm on mesoporous zeolite (Naβ).

2.3 Solid State NMR

The spin quantum number I is a characteristic property of a nucleus. Spin quantum number can be an integer or a half integer depending on the number of protons and neutrons in the nucleus. When the number of both protons and neutrons is even, the nucleus has an I value of zero. The combination of odd numbers of protons and neutrons give an integer I value, whereas other combinations result in a half integer I value.

The number of possible spin orientations relative to an axis equals 2I + 1. Nuclei with an I value of 0 have one possible orientation and therefore their magnetic moment is zero, which makes them NMR inactive. Nuclei that have non-zero magnetic moment are NMR active although their NMR sensitivity can be substantially different.

Nuclear Magnetic Resonance Spectroscopy is a technique that studies properties of NMR active nuclei in molecules by applying a magnetic field and observing the frequency of the resonant electromagnetic field.

In the simplest case, a nucleus with I = 1/2 has two energy levels denoted as spin up and spin down (Figure 12). The energy difference between the two states is defined by the equation:

$$h\nu = \gamma\hbar B_0 \qquad (8)$$

where γ is the magnetogyric ratio of the nucleus, and B_0 is the strength of the magnetic field. As $\gamma \cdot \hbar \cdot B_0 / h$ is the Larmor frequency of a nucleus, the resonance condition will occur at $\nu = \nu_L$.

The local magnetic field around nuclei can differ from the applied magnetic field, as the applied magnetic field can induce electronic orbital angular momentum resulting in an additional magnetic field. The strength of this additional magnetic field is proportional to the applied field:

$$\delta B = -\sigma B_0 \qquad (9)$$

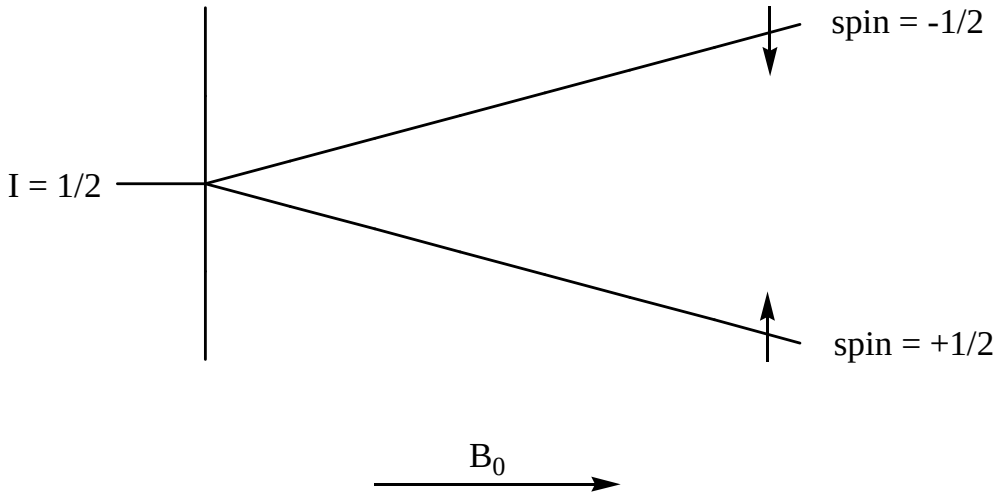

Figure 12. Energy level splitting diagram for a nucleus with I = 1/2.

where σ is the shielding constant. The shielding constant is affected by the local electronic environment around the nuclei. The important consequence is that nuclei in different environments will have slightly different resonance frequencies:

$$\nu_L = (1-\sigma)\frac{\gamma B_0}{2\pi} \qquad (10)$$

Because the resonance frequency depends on the strength of the applied magnetic field that is different from one instrument to another, it is more convenient to express it as a chemical shift, which is independent of the B_0 term:

$$\delta = \frac{(\nu - \nu_0)}{\nu_0} \cdot 10^6 \qquad (11)$$

where v_0 is the resonance frequency of a standard.

Most of the NMR studies of zeolites are conducted using solid samples, which causes difficulties with line resolution. Line broadening in NMR spectra results from direct magnetic interaction between the nuclear spins. This results in the presence of a local magnetic field with magnitude B_{loc} such that:

$$B_{loc} = \frac{\gamma \hbar \mu_0 m_I}{4\pi R^3} \cdot (1 - 3\cos^2\theta) \qquad (12)$$

This field is averaged to zero in the case of fast tumbling molecules in solution but is present in the case of solid samples. Another contributor to line broadening is chemical shift anisotropy due to different orientations of a molecule with respect to the magnetic field. Similarly, this anisotropy is averaged in solutions but present in the solid state and its degree varies with the angle between the principal axis of the molecule and the direction of the magnetic field according to term $(1 - 3\cos^2\theta)$.

The magic-angle spinning (MAS) NMR technique utilizes the fact that the $(1 - 3\cos^2\theta)$ term is equal to zero, when θ = 54.74°. Rapid spinning of the sample at the "magic" angle relative to the applied magnetic field eliminates broadening from both

dipole-dipole interactions and chemical shift anisotropy. The spinning speed has to be higher than the frequency width of the spectrum, otherwise spinning sidebands will be present.

There are a number of NMR active nuclei that are important in zeolite science. ^{29}Si (I = 1/2), ^{27}Al (I= 5/2), ^{11}B (I = 3/2), ^{19}F (I = 1/2) and ^{31}P (I=1/2) are the NMR active isotopes of the elements that can be present in the zeolite framework.

The chemical shift of these elements can provide information about whether they are a part of the framework or exist as extra-framework species.[87, 88] ^{1}H (I = 1/2), ^{13}C (I = 1/2), ^{15}N (I = 1/2) is used for studying:

1. Organic structure directing agents used in zeolite synthesis;[89]
2. Organic compounds used to determine the strength of acid sites in zeolites;[90]
3. Organic functional groups that can be grafted onto the zeolite surface.[91]

Examples of ^{29}Si and ^{27}Al MAS NMR spectra of zeolites are shown in Figures 13 and 14 respectively. 29-silicon MAS NMR provides information about silicon atoms with different environments. Silicon atoms located in the zeolite framework and connected to other silicon or aluminum atoms via oxygen bridges are named Q4 (or Q4Aln, where n is the number of adjacent aluminum atoms). Because the majority of silicon atoms in the zeolite have this environment, the respective peak located at -110 ppm is the most intense. Silicon atoms on the external surface of the zeolite or silicon atoms located at defect sites in the zeolite pores have one or more hydroxyl groups attached to them. These atoms are labeled as Q3, Q2 and Q1 for 1, 2 and 3 hydroxyl groups respectively. Q3 silicon atoms can be observed in zeolite, while there are usually too few Q2 and Q1 atoms to be seen. A weak chemical shift at -101 ppm in Figure 13 represents the Q3 silicon atoms in the sample. The intensity of the Q3 peak is proportional to the amount of the external surface, so it is more prominent in the case of zeolite nanoparticles than large crystals.

Surface functionalization of zeolites is commonly carried out using silanes that possess a target organic group. The chemical shift of silicon atoms in a silane can be significantly different from those in the zeolite framework. For example, the chemical shift at approximately -60 ppm in Figure 13 comes from 3-mercaproporylsilane groups present on the zeolite surface. The peaks arising from the presence of functional groups can be used to estimate the amount of silane in the material. This is done by integrating the silane peak and dividing the area by the sum of integrated intensities of all silicon atoms in the sample.

Example of ^{27}Al MAS NMR is shown in Figure 14. The chemical shifts are broadened due to the quadrupolar nature of ^{27}Al nuclei, but their position provides important information about the coordination state of aluminum atoms. Aluminum located in the zeolite framework is tetrahedrally coordinated and its chemical shift ranges from approximately 50 to 65 ppm depending on the environment. Higher amount of framework aluminum in the zeolite results in a downfield shift of the peak and vice versa. NaY zeolite is an example of high alumina zeolite and the chemical shift of framework aluminum is located at ~ 62 ppm (Figure 14). Zeolites can also contain extra-framework aluminum species, such as Al^{3+} acting as counter ions at the anionic sites on the zeolite surface. These atoms have octahedral coordination and their chemical shift appears around 0 ppm. Figure 14 also contains a chemical shift at ~ 30 ppm, which is typical for either pentacoordinated aluminum species or significantly distorted tetrahedrally coordinated aluminum.

Various external standards are used in MAS NMR experiments for different nuclei just like tetramethylsilane is used as a reference in ^{1}H solution NMR. The commonly used standards are TMS for ^{29}Si (0 ppm), 1 M solution of aluminum nitrate in water for ^{27}Al (0 ppm), and solid adamantane for ^{13}C (28.6 and 38 ppm).

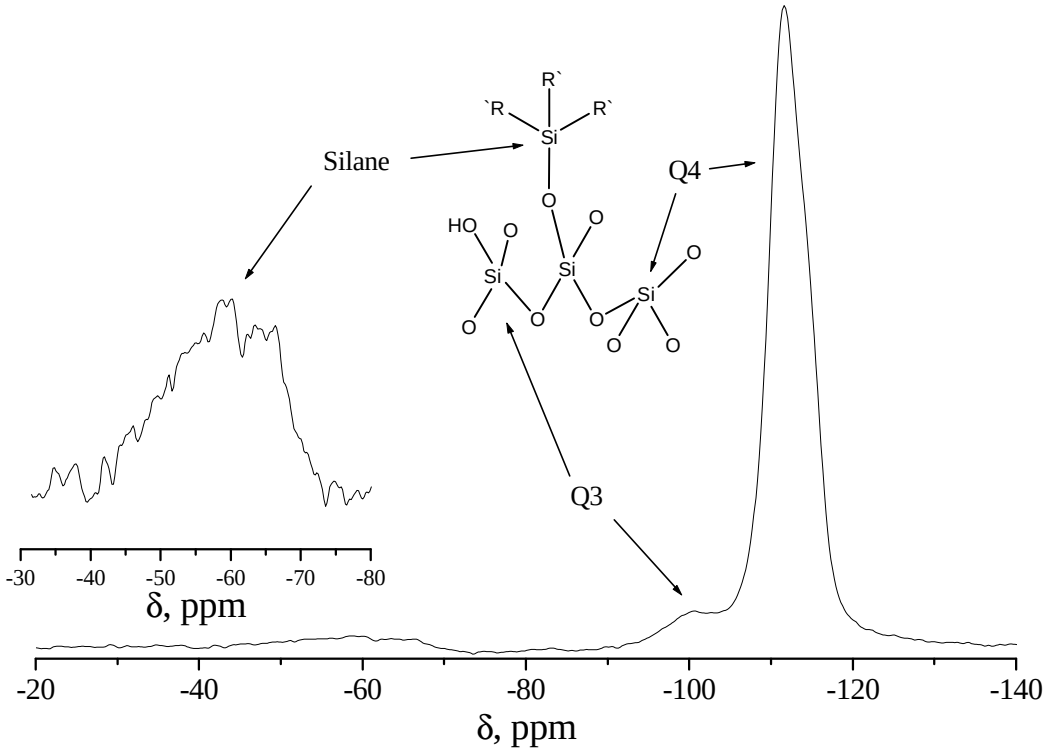

Figure 13. Representative ^{29}Si MAS NMR of Silicalite-1 zeolite grafted with mercapropropyl silane.

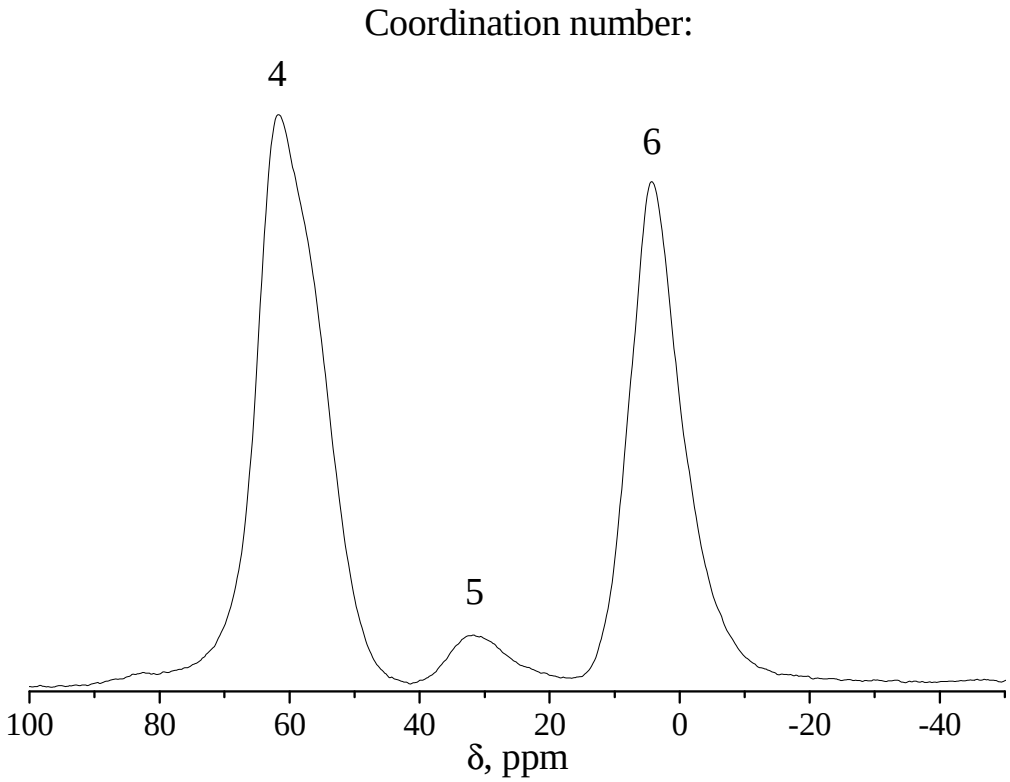

Figure 14. Representative ^{27}Al MAS NMR of NaY zeolite.

2.4 Inductively Coupled Plasma - Optical Emission Spectroscopy.

Elemental composition of zeolite materials can be quantified by using the Inductively Coupled Plasma - Optical Emission Spectroscopy (ICP-OES) technique. The basis for ICP-OES is using a high power radio frequency signal to generate an electromagnetic field in which a carrier gas (typically argon) is ionized and converted into a plasma state with temperatures of several thousand Kelvins. Then a studied solution is injected in the plasma beam and the atoms are excited and emit electromagnetic radiation, usually in UV and visible ranges. The emitted photons are then detected using a photomultiplier tube or a charge-coupled device (CCD) detector. In the resulting spectrum, the intensity of the wavelengths is compared with the intensities produced by standards with known concentrations of the studied element and its concentration in the analyzed solution is calculated.

For ICP-OES measurements, solid materials need to be dissolved first. In the case of zeolites, the solids are dissolved using a hydrofluoric acid solution, and then the solution is neutralized with boric acid to prevent the loss of silicon which forms volatile SiF_4. Standard solutions of the studied elements, are then prepared, either separately or, in case of their compatibility, in mixtures. The instrument is calibrated using the standards and the samples are then analyzed. A commonly used practice is to use replicates of sample solutions and calculate the average concentration of the elements. The lower limit of detectable concentrations (LOD) varies from one element to another. Lighter elements tend to have lower LODs, while heavier elements experience difficulties with line broadening and insufficient resolution.[92]

2.5 Scanning and Transmission Electron Microscopy

Electron microscopy (EM) is another powerful tool for studying zeolite materials. Parameters, such as particle size and shape, surface morphology, degree of aggregation

presence of other phases, distribution of metal or metal oxide clusters and more can be determined using scanning and transmission electron microscopes.

Electron microscopes operate using principles similar to those used in light microscopy. The advantage of EM is that the wavelength of electrons is much smaller than the wavelength of visible light, which results in much higher achievable resolutions and allow obtaining images of nanoscale specimen. The beam of electrons is generated using an electron gun and then passes through a series of magnetic lenses and apertures in order to obtain a well-focused beam, which “illuminates” the sample.

In transmission electron microscopy (TEM) the beam passes through the sample deposited on a thin metal grid typically coated with a thin layer of carbon and reaches the detector. The image collected in bright field imaging mode gives contrast information about the sample, in which thicker areas or areas with higher atomic number will be darker and vice versa. A representative TEM image is shown in Figure 15. The lattice fringes can be seen in the particles, and can be used to estimate the sample crystallinity. The choice of specimen support is important for high resolution TEM, since thicker support film decreases the resolution and may make lattice fringes difficult to detect. Good results are obtained using amorphous carbon films under 10nm in thickness or carbon lacey films, where the nanocrystals can be suspended on a carbon “net” with little or no background interference.

In scanning electron microscopy, the focused electron beam scans the specimen surface and backscattered or secondary electrons are then amplified and collected at the detector. Unlike TEM, scanning electron microscopy provides information about the surface morphology (Figure 16). Because the zeolite surface is nonconductive and consists of atoms with low atomic numbers, it tends to collect the charge gained from the electron beam. This results in the presence of artifacts in the image. This is why zeolite samples are sputter coated with a thin layer (several nanometers) of conductive material, typically gold or platinum. The presence of gold clusters on the zeolite surface may make

the surface morphology study more difficult in the case of nanocrystals. Therefore the balance between the surface conductivity and the conductive film thickness should be considered.

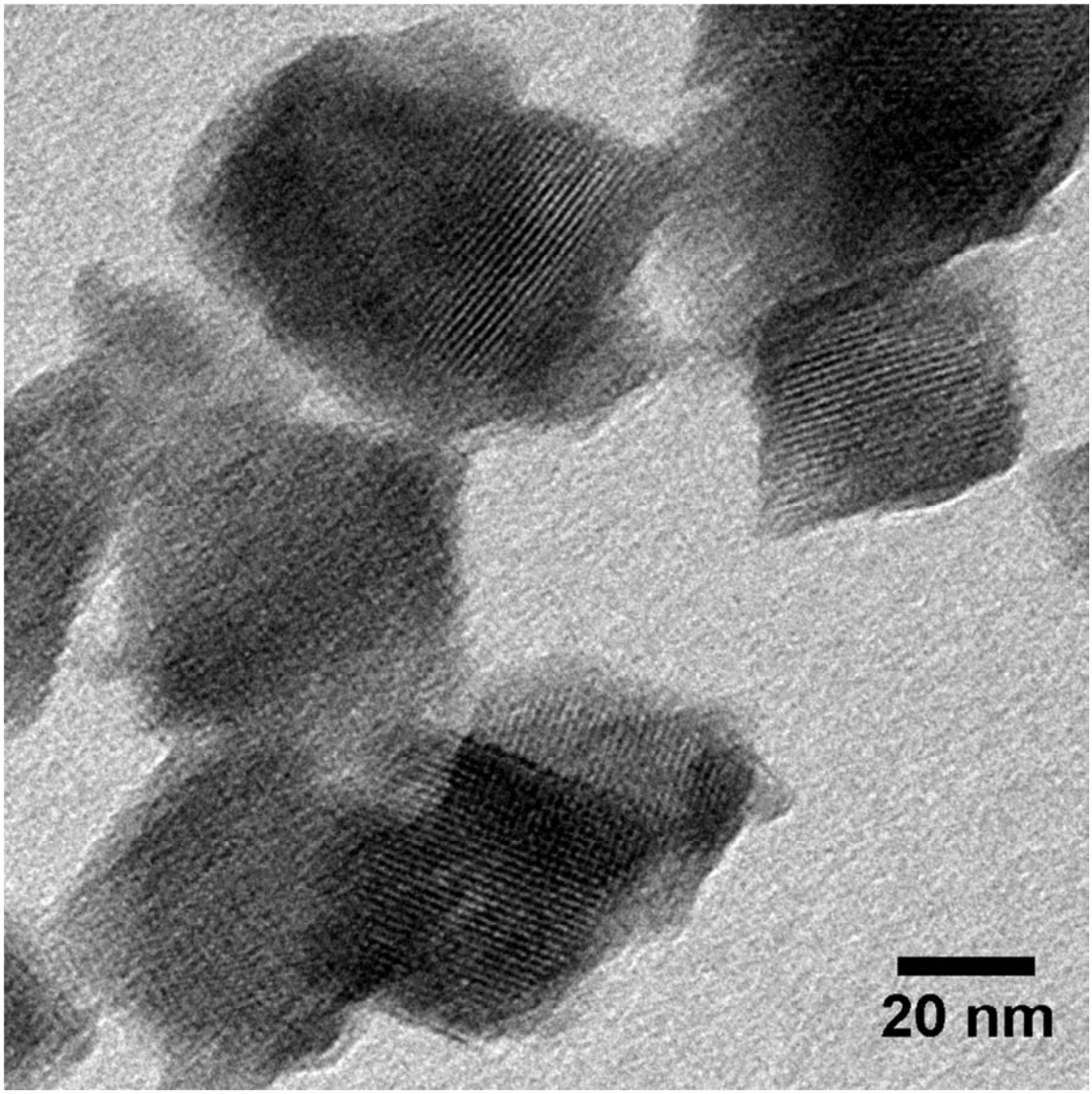

Figure 15. Representative TEM image of nanocrystalline zeolite (NaY).

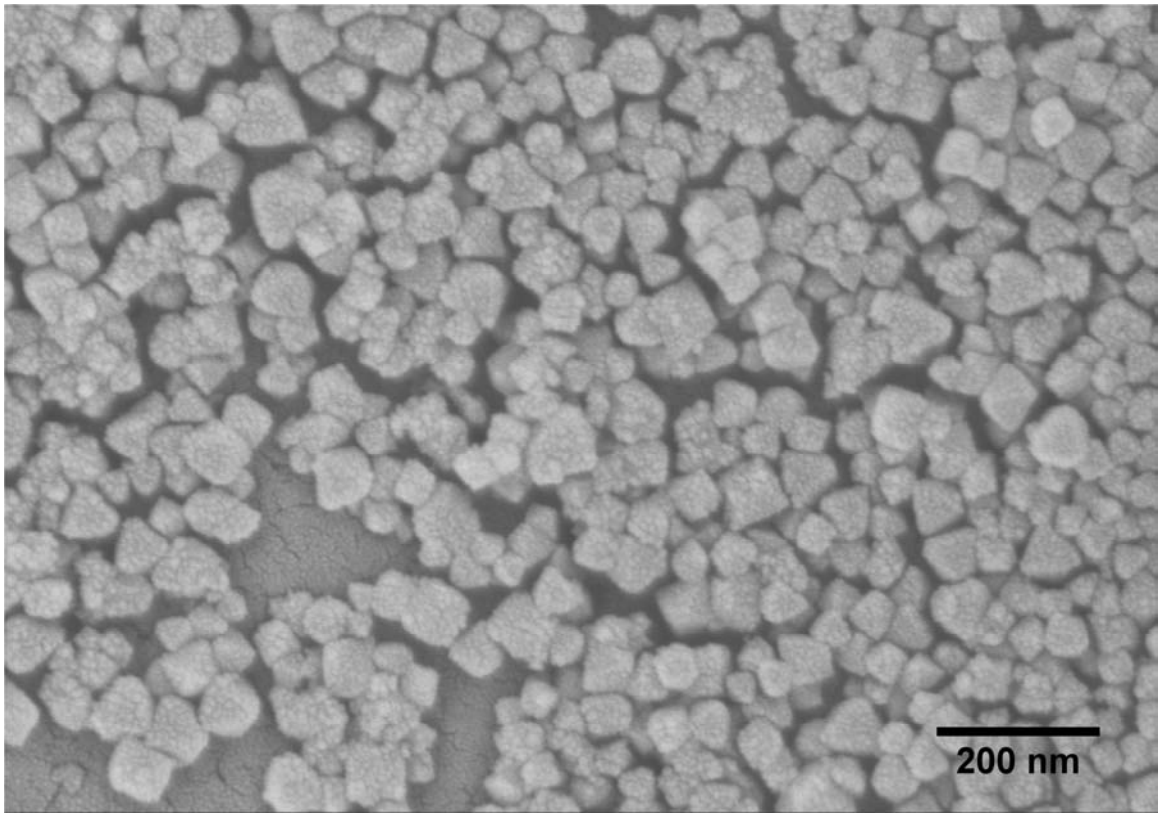

Figure 16. Representative SEM image of zeolite nanocrystals (NaY)

CHAPTER 3.

SYNTHESIS OF MESOPOROUS ZSM-5 AND β ZEOLITES

3.1 Abstract.

Development of new zeolite based materials is essential for a variety of applications in catalysis, separations and medicine. Increasing the specific surface area and decreasing the micropore diffusion path length in zeolites are important factors for improving the performance of zeolites in catalytic applications and these factors can be optimized by decreasing the zeolite particle size. Creation of a hierarchical zeolite material that possesses both micro- and mesopores with very large surface areas and improved mass transport properties is an effective solution. In this study, a facile approach to a one step synthesis of nanocrystalline ZSM-5 and β zeolites from a single template system in 12 to 24 hours at 140 ^{o}C and with high yield is presented. ZSM-5 zeolite crystals as small as 6 nm which form mesoporous aggregates of approximately 200 nm in diameter were synthesized using this method. Depending on the synthesis conditions, zeolite beta nanocrystals of approximately 20 to 150 nm in diameter or mesoporous aggregates of approximately 120 to 140 nm in diameter were prepared. The mesopore volume and size distribution showed a dependence on particle size such that smaller particles lead to higher mesopore volumes and narrower pore size distributions. The size of individual crystals, as well as mesopore surface area and pore volume can be controlled by adjusting the pH of the reaction mixture, as well as the hydrothermal treatment temperature and duration. In the case of zeolite beta synthesis, the concentration of the reaction mixture affected the crystal growth and the degree of aggregation.

3.2 Introduction.

High surface areas and ion exchange properties of zeolites, as well as tunable silicon to aluminum ratio (SAR) are desirable properties which lead to their use as

catalysts for a variety of different reactions. One of the most commonly used zeolites is ZSM-5, a zeolite with MFI type framework, 0.54 nm pore diameter and SAR that can be varied from 10 to several hundred. ZSM-5 zeolite is usually synthesized with sodium cations acting as counter ions for the negatively charged framework. Sodium ions can then be replaced with other cations capable of entering the pores during a post-synthesis modification of the zeolite. Zeolite beta is one of the most commonly used zeolites in a number of catalytic reactions. Zeolite beta possesses intersecting pore channels approximately 6.6 Å in diameter, which places them between ZSM-5 (5.6 Å pores) and faujasite (7.4 Å pores) zeolites. The silicon to aluminum ratio (SAR) in zeolite beta has been varied greatly, and lower Si/Al ratios have been found to favor a faster crystallization rate.[93]

ZSM-5 zeolite has traditionally been used in the petroleum industry for fluid catalytic cracking due to the presence of acidic sites on its surface.[15, 94-96] The ZSM-5 zeolite can be used in its H-form[15, 94] or after ion exchange with different metal ions, such as nickel[95] or zinc.[97] Pt- and Ir- exchanged ZSM-5 zeolites are used in catalytic hydroisomerization of n-alkanes.[98] Pt and Pd loaded β zeolite have been used for the selective hydrogenation of toluene with complete conversion and 100% selectivity under optimal conditions.[56] Modhera and coworkers studied hydroisomerization of 1-hexene over platinum loaded nanocrystalline zeolite-beta.[99] Nie et al. investigated the conversion of citral to menthol by Zr-loaded nanocrystalline zeolite beta. The use of zeolite beta resulted in a high yield as well as high diastereoselectivity towards the desired product.[54] Ding and coworkers reported that nanocrystalline zeolite beta with W-Ni catalyst had higher hydrodesulfurization, hydrodearomatization and hydrodenitrogenation activities than conventional micron-sized zeolite particles.[100]

In the catalysis community, there has been a great deal of interest in nanocrystalline zeolites due to potential improvements in catalytic activity resulting from increased surface areas and decreased diffusion path lengths.[18, 101] Several groups have

compared the catalytic activity of nanocrystalline ZSM-5 to conventional micron-sized crystals.[102-104] Nanocrystalline ZSM-5 zeolites with particle sizes ranging from 20 to 50 nm were compared to microcrystalline ZSM-5 with respect to catalytic activity in epoxide rearrangement reactions.[102] The authors found that the nanocrystalline ZSM-5 zeolites had a significantly higher conversion rate and selectivity towards the desired products than the micron-sized zeolite. Choi and coworkers showed that micropore-mesopore composite materials formed from ultrathin sheets of ZSM-5 exhibit improved catalytic activity for methanol-to gasoline conversion.[103] These composite materials were also more resistant to deactivation occurring due to coke deposition.[103, 105] Firoozi et al. showed that the use of nanocrystalline ZSM-5 resulted in a higher methanol to propylene conversion rate than for large ZSM-5 crystals.[104]

Catalytic activity of zeolites can be increased by decreasing their crystal size, which results in shorter diffusion paths in micropores and an external surface area constituting a larger fraction of the total surface area. Both factors allow an easier access of reactants to the active sites on the surface of the zeolite crystals. However, zeolite nanocrystals have been reported to be less stable than micron-sized crystals. Separation of nanocrystals from the reaction mixture is also more challenging than in the case of larger particles. Another disadvantage of extremely small crystals is an increased pressure drop in packed bed reactor systems. One of the ways to overcome these disadvantages is to synthesize hierarchical zeolitic material that consists of zeolite nanocrystals within larger size aggregates, such that mesopores constitute the inter-crystalline space. A graphical representation of mesoporous zeolite is shown in Figure 17, where micropores are shown in green and mesopores in blue. Different approaches to synthesis of hierarchical zeolite materials were summarized in a review by Pérez-Ramírez and coworkers.[106] Soler-Illia et al. discussed the fundamentals of zeolite synthesis and production of hierarchical zeolites.[107]

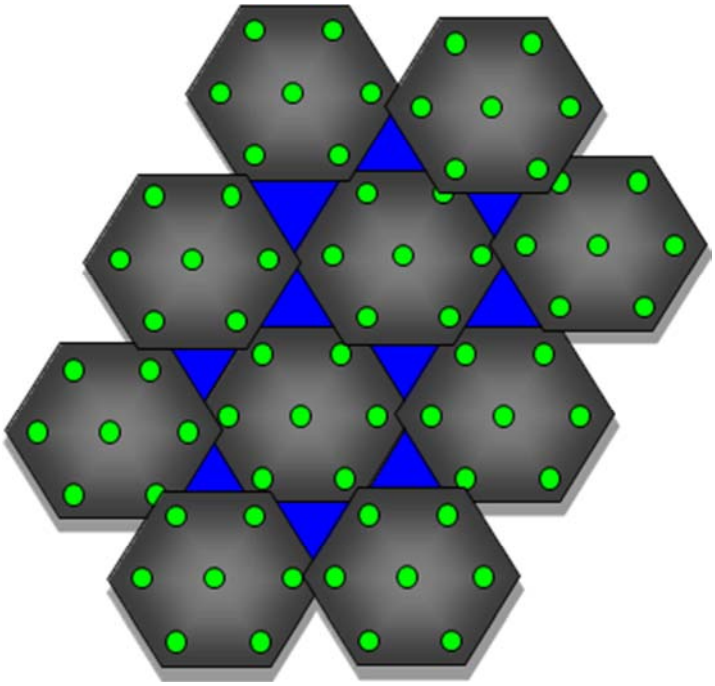

Figure 17. Graphical representation of mesoporous zeolite.

In a post-synthesis treatment, zeolite crystals several hundred nanometers in size were treated with sodium aluminate followed by acid treatment in order to create mesopores 4 to 15 nm in diameter.[108] Ogura used an aqueous sodium hydroxide solution in order to create mesopores in ZSM-5 crystals and concluded that the mesopore volume progressively increased with longer base treatment times.[109] Mesoporous β zeolite such as leaching of large crystals with acids,[110] as well as inorganic[111] and organic bases.[112, 113] During such treatments, selective desilylation or dealumination of the zeolite occurs leading to formation of mesopores. A method described by Mohr et al. described synthesis of mesoporous zeolites by synthesizing zeolite crystals first, then binding them with silica material and converting the silica binder into zeolite during the subsequent hydrothermal treatment.[114]

Another approach is to use a "hard template", when a porous material, such as carbon black or silica gel is used to assist in mesopore formation.[115-117] Tong and coworkers employed a silica monolith and converted the amorphous walls into Naβ zeolite, while using carbon as a transitional template and meso/macropore formation agent.[115] Valtchev et al. used a silica containing vegetal template (Equisetum arvense leaves and stems) in order to synthesize a hierarchical zeolite material containing micro, meso and macropores.[116] Lei and coworkers synthesized micro-mesoporous zeolite beta by modifying a bimodal pore silica gel with zeolite beta seed crystals and hydrothermally treating the system.[117]

A "soft template" approach typically involves two molecular templates used simultaneously or in sequence to induce formation of the zeolite as a microporous phase with mesoporous areas between zeolite crystals.[103, 118-121 122, 123] Choi and coworkers used a bifunctional surfactant, composed of a 22 carbon atom alkyl chain and two quaternary ammonium groups separated by a C6 alkyl linkage. The surfactant formed micelles, in which the quaternary ammonium atoms were located in planes, where the crystallization of ZSM-5 nanosheets occurred.[103] Zhu and coworkers employed a double template

system, where the TPAOH template was governing crystallization of the MFI zeolite phase and polyvinyl butyral was used as a mesopore directing agent.[118] Xin et al. used a combination of TPABr and [3-(trimethoxysilyl)propyl] octadecyl-dimethylammonium chloride to synthesize iron-exchanged ZSM-5 powders containing mesoporous aggregates of microporous ZSM-5 particles smaller than 50 nm and tested the catalytic activity of the zeolite in selective hydroxylation of benzene to phenol.[119] Li and coworkers used a TPAOH / L-lysine co-template system and a two-step synthesis to prepare microspheres composed of stacked nanocrystals approximately 35 nm in size.[120] A micro-mesoporous composite with zeolite crystals around 20 nm in size was synthesized by using a mixture of TPAOH and alkyltriethoxysilane.[124] Chmelka and coworkers used a three step double template system, where ZSM-5 was precrystallized with TPAOH template followed by addition of mesopore forming phenylaminopropyltrimethoxysilane and heated at 90 ^{o}C for 6 hours. The resulting reaction mixture was then hydrothermally treated at 170 ^{o}C for 7 days, and zeolite crystals 5-10 nm in size were produced.[125]

Bagshaw and coworkers synthesized a zeolite beta / mesoporous silica composite which contained a structured mesopore and microporous zeolite areas.[121] Composite materials using MCM-41 / zeolite-beta composites were synthesized by Xu et al. via dissolution of zeolite Beta particles and subsequent hydrothermal treatment with hexadecyltrimethylammoniumbromide as a mesopore directing agent.[122]

Aguado and coworkers prepared a hierarchical zeolite-beta material by hydrothermally treating zeolite beta nanocrystals, whose surface was functionalized with organosilanes. The organic moieties provided mesopore spacing between the zeolite crystals. The textural properties of the composite material depended on the type and concentration of organosilane groups on the zeolite seed crystals.[123]

Fang and coworkers reported that the synthesis of mesoporous ZSM-12 zeolite is possible without the use of mesopore directing agent.[126] 20-30 nm zeolite nanocrystals

forming aggregates under 1 μm in size were synthesized from a supersaturated reaction mixture. The authors concluded that formation of mesoporous aggregates using a single template system is achievable by a careful choice of the zeolite nucleation conditions, and that the zeolite nanocrystals form mesopores through self-assembly. Liu et al demonstrated the synthesis of zeolite beta aggregates without a secondary template at different Si/Al ratios, with lowest primary particle size of 80 nm.[127] Camblor and coworkers studied the effect of Si/Al ratio on the crystal size of zeolite beta and found that crystals under 15 nm in size could be synthesized at low Si/Al ratios.[29] The mesopores originate from the interparticle distance, which are non-aggregated in the case of as-synthesized material and may be partially sintered after calcination. Different approaches to preparation of mesoporous zeolites have been summarized by Tao and coworkers.[128]

Here, we report a one-step synthesis of nanocrystalline ZSM-5 and β zeolites from a single template reaction mixture. The size of individual ZSM-5 crystals can be varied from approximately 40 nm to as low as 6 nm. The nanocrystals form mesoporous aggregates approximately 200 nm in size and the degree of mesoporosity was found to be particle size dependent. The crystal size and mesoporosity of the ZSM-5 samples is controlled by varying temperature, hydrothermal treatment duration and the pH of the reaction mixture. The smallest crystals were synthesized at a relatively low temperature of 140 ^{o}C and short hydrothermal treatment times with very good yields.

While many approaches to the synthesis of zeolite beta nanoparticles and hierarchical structures have been reported in the literature, the strategy used in the study reported here is distinct in that the zeolite beta synthesis conditions are systematically varied for a given Si/Al with a single template in order to control the particle size and mesoporosity. Specifically, nanocrystalline zeolite beta with hierarchical porosity was synthesized from a single template system in a one-step hydrothermal treatment.

In the case of zeolite beta synthesis an additional factor that was found to influence formation of mesoporous product was concentration of the reactants in the synthesis gel. The use of concentrated synthesis gels resulted in mesoporous aggregates of approximately 140 nm in size consisting of nanocrystals with sizes ranging from approximately 16 to 40 nm. The use of diluted reaction mixtures resulted in isolated zeolite nanoparticles with sizes of 23 and 156 nm. Both ZSM-5 and β samples were characterized by a combination of spectroscopic, adsorption and electron microscopy techniques.

3.3. Experimental

3.3.1. Zeolite synthesis.

ZSM-5 and Naβ samples were synthesized from clear gel solutions via hydrothermal treatment. A reaction mixture of the following composition was used:

ZSM-5	TEOS	$NaAlO_2$	TPAOH	TPABr	H_2O
Molar ratio	25	1	5	4	1000

Naβ	TEOS	$NaAlO_2$	TEAOH	TEABr	H_2O
Molar ratio	25	1	10	10	1000

where TEOS = tetraethylorthosilicate (Aldrich), TPAOH / TPABr = tetrapropylammonium hydroxide / bromide, TEAOH / TEABr = tetraethylammonium hydroxide / bromide.

For ZSM-5 zeolite synthesis, TPAOH, 1/3 of water and sodium aluminate were mixed together and stirred until sodium aluminate was completely dissolved. Then, the rest of the water and TPABr were added to the solution and stirred briefly to dissolve the solid TPABr. In the case of Naβ synthesis, TEAOH, water and sodium aluminate (EM Science) were mixed together and stirred until sodium aluminate was completely dissolved followed by addition of TEABr, which dissolved quickly under stirring. Next, TEOS was added to the reaction mixture which was stirred for 14-16 hours at room temperature.

Some ZSM-5 reaction mixtures were rotary evaporated at 65 ^{o}C until a specific amount of reaction mixture volume was removed. The evaporated volume was then compensated by adding appropriate amounts of deionized water. pH of the reaction mixture was measured before and after the rotary evaporation. The reaction mixture was then placed in a stainless steel autoclave equipped with a stirbar and PTFE liner. The synthesis was carried out at constant stirring at 250 rpm. The synthesis temperature and time were varied from 140 to 165 ^{o}C and from 12 to 72 hours, respectively.

The Naβ reaction mixtures were rotary evaporated at 65 ^{o}C until a 75% of the initial volume was removed. The reaction mixture was then diluted with appropriate amounts of deionized water to 50 % or 100% of the initial volume. pH of the reaction mixture was measured before and after the rotary evaporation of each batch of zeolite to ensure its consistency. The reaction mixture was then placed in a stainless steel autoclave equipped with a stir bar and PTFE liner. The synthesis was carried out at constant stirring at 250 rpm.

After synthesis, zeolite crystals were separated from the supernatant by centrifugation at 14000 rpm (20817 x g) for 15 minutes. Ethanol or water was added to

the solid and the resulting suspension was sonicated for 1 hour until the entire solid was redispersed, followed by centrifugation at 14000 rpm (20817 x g) for 15 minutes. The washing was done twice with water and once with ethanol. After the final washing, the solid was redispersed in ethanol after sonication and the slurry was dried in an oven at 70 ^{o}C overnight. To remove the template from the pores, the samples were heated at 1.6 ^{o}/min to 600 ^{o}C and calcined for 6 hours in air.

3.3.2. Characterization.

Powder X-ray diffraction patterns (Siemens D5000 X-ray diffractometer with Cu Kα and nickel filter) were collected from 2θ =5 to 55 with a 0.04 step size and 1 s/step. Relative crystallinity (RC) of ZSM-5 was calculated by integrating the peaks between 2θ = 22.5 and 25 after a baseline correction and compared with a commercially available ZSM-5 zeolite (Zeolyst). For Naβ the peaks between 2θ = 20 and 24 were integrated after a baseline correction and compared with a commercially available zeolite beta (Zeolyst).

Surface areas of the parent and calcined nanocrystalline ZSM-5 and β zeolites were measured using the BET method on a Nova 4200 Nitrogen Adsorption Instrument (Quantachrome). Typically, 100 mg of zeolite powder was dried overnight at 120 ^{o}C in vacuum. A 7-point BET isotherm was then recorded and the specific surface area was calculated for the samples before and after calcination in order to obtain the external (S_{ext}) and total specific surface areas (S_{tot}) respectively. The external surface area (S_{ext}) value of ZSM-5 was also used to evaluate the size of crystals according to a previously derived formula, $x=3216/S_{ext}$ where x is the ZSM-5 crystal size in nm and S_{ext} is the measured external specific surface area in m^2/g assuming cubic crystals.[27] In the case of Naβ samples, the derived formula for determination of crystal size $x=3252/S_{ext}$ where x is the ZSM-5 crystal size in nm and S_{ext} is the measured external specific surface area in m^2/g assuming cubic crystals.

A 50 point adsorption / desorption isotherm was measured and used for calculation of micropore and total pore volume as well as the average diameter of mesopores. The total pore volume (V_{tot}) was calculated by measuring the amount of adsorbed nitrogen at the highest adsorption point. The t-plot method was used to calculate the micropore volume (V_{micro}). The mesopore volume (V_{meso}) was calculated from the difference between the V_{tot} and V_{micro}. The size distribution of mesopores in ZSM-5 zeolite samples was calculated using a Barret, Joyner and Halenda (BJH) model.[86] Mesopore size distributions in zeolite-beta were calculated using NLDFT equilibrium model.

Elemental composition of the solids was determined by inductively coupled plasma optical emission spectroscopy (Varian 720-OES). The solids were prepared for analysis in the following manner: 10 mg of zeolite powder was placed in a plastic tube. 1.6 mL of 70:30 HCl : HF solution was added to the tube and the suspension was sonicated for 15 minutes until all of the solid was completely dissolved. Then, 0.6 mL of concentrated nitric acid and 6 mL of 5% boric acid solutions were added, and the total volume was adjusted to 10 mL with DI water. Three replicate solutions were prepared for each sample.

A 300 MHz (6.9 T) wide bore magnet spectrometer (Varian) with a TecMag Discovery Console was used to record ^{27}Al and ^{29}Si magic angle spinning nuclear magnetic resonance (MAS NMR). Aluminum-27 spectra were recorded at the Larmor frequency of 78.209 MHz. 70 mg of powder was loaded in a 4 mm zirconia rotor and spun in a Chemagnetics pencil probe at 12 kHz. The spectra were acquired with 12000 scans, 3 μs pulse width and 3s pulse delays. ^{29}Si MAS NMR spectra were recorded at a Larmor frequency of 59.621 MHz. Approximately 250 mg of sample was loaded in a 7 mm zirconia rotor and spun in a Chemagnetics pencil probe at 7 kHz. A total of 1000 scans were acquired 4 μs pulse width and 60s pulse delays.

For TEM imaging (JEOL JEM-1230 Transmission Electron Microscope), a drop of dilute sample suspension in methanol was placed on a carbon coated copper grid (Ted Pella) and dried at room temperature prior to the measurement.

3.4 Results and Discussion – Mesoporous ZSM-5 synthesis.

3.4.1 Powder X-ray diffraction XRD and product yield.

Nanocrystalline ZSM-5 zeolites were synthesized with and without an evaporation step (E and N series, respectively), with temperatures ranging from 135-165°C, and with hydrothermal synthesis times varying from 12-72 hours. The synthesis and characterization of the nanocrystalline ZSM-5 samples is summarized in Table 1. The samples are numbered in the order of increasing external surface area. Representative powder X-ray diffraction (pXRD) patterns are shown in Figure 1 for a ZSM-5 standard sample (Figure 18A), for ZSM-5 samples synthesized without the evaporation step (Figure 18B,C) and for ZSM-5 samples synthesized from partially evaporated gels (Figure 18D, E, F). Only characteristic reflections of MFI type zeolite were observed in the X-ray powder patterns. The relative crystallinity (RC) of the samples (Table 1) synthesized without the evaporation step remains close to that of the reference standard. The percent yield of the zeolite samples mainly depends on the duration of hydrothermal treatment. Higher product yields correlate with longer synthesis times. The yield was in general over 80% except for the ZSM-5 samples N6 and N7, for which the yields were 59 and 53 % respectively. These samples were also synthesized using the shortest hydrothermal treatment times and had the highest S_{ext} values within the non-evaporated series.

The silicon to aluminum ratio (Si/Al) in the zeolite samples determined by ICP-OES was consistently ~30 and did not change significantly at different synthesis temperature and time conditions. Further decrease of particle size and increase of external

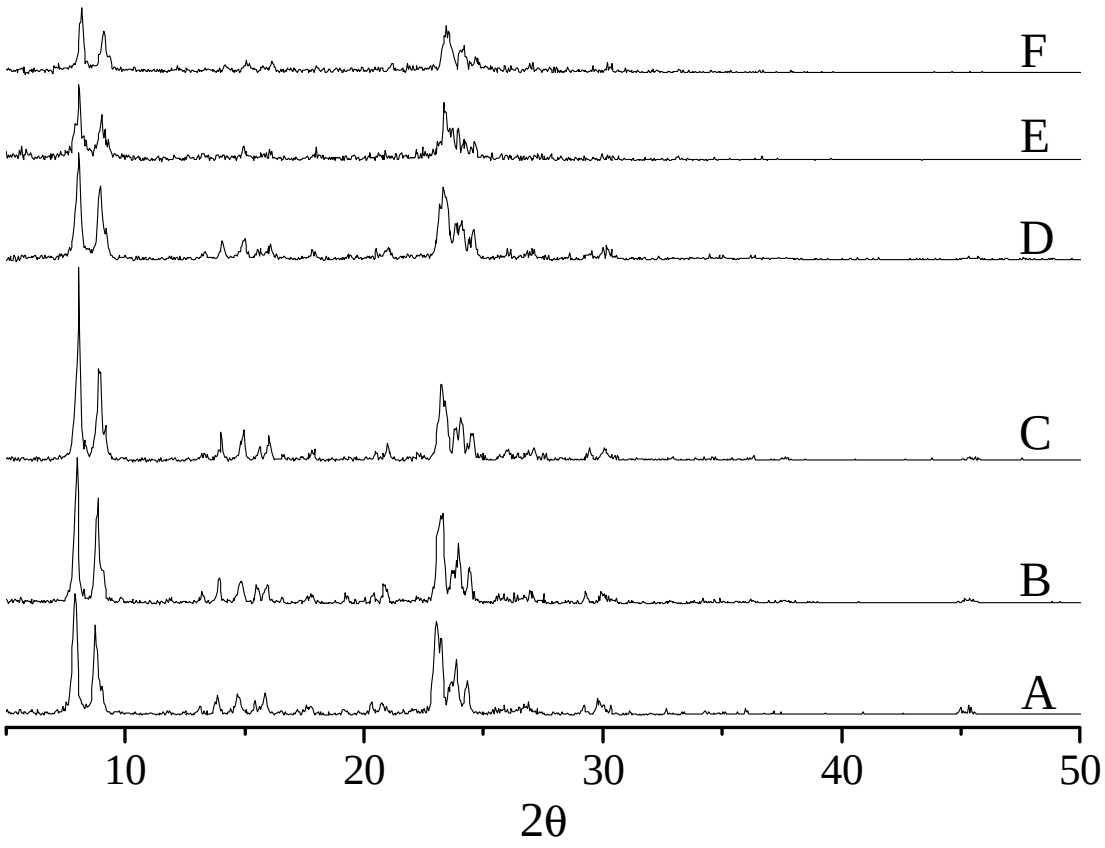

Figure 18. Powder XRD patterns of the ZSM-5 standard (A) and nanocrystalline ZSM-5 samples N1 (22 m^2/g) (B), N5 (47 m^2/g) (C), E4 (122 m^2/g) (D), E6 (153 m^2/g) (E), and E7 (175 m^2/g) (F).

Table 1 Summary of synthesis and characterization of nanocrystalline ZSM-5

Name	T, ^{o}C	Time, h	% evap	pH	S_{ext}, m^2/g	S_{int}, m^2/g	S_{tot}, m^2/g	RC, %	$V_{micro,}$ cc/g	$V_{meso,}$ cc/g	$V_{tot,}$ cc/g	Si/Al	Yield, %	BET size, nm*	TEM crystal size, nm
N1	155	72	0	11.52	22	298	320	96	0.127	0.085	0.212	31 (0.8)	83	146	42
N2	165	48	0	11.52	31	300	331	102	0.134	0.136	0.270	31 (0.3)	84	104	-
N3	140	72	0	11.52	36	309	345	103	0.148	0.116	0.264	28 (0.1)	94	89	-
N4	140	48	0	11.52	42	311	353	98	0.145	0.136	0.281	29 (0.2)	86	77	-
N5	140	24	0	11.52	47	306	353	99	0.148	0.138	0.286	29 (0.7)	86	68	19
N6	140	12	0	11.52	56	300	356	89	0.142	0.139	0.281	27 (1.1)	59	57	-
N7	135	12	0	11.52	60	299	359	93	0.149	0.151	0.300	27 (0.4)	53	54	-

Table 1. Continued.

E1	140	72	50	11.05	35	313	348	101	0.135	0.162	0.297	30 (0.5)	73	92	-
E2	140	48	50	11.05	51	311	362	99	0.151	0.135	0.286	28 (1.3)	95	63	-
E3	140	24	25	11.16	85	304	389	76	0.134	0.244	0.378	29 (0.8)	75	38	-
E4	140	24	50	11.05	122	298	420	74	0.104	0.43	0.534	30 (0.1)	74	26	6.4
E5	140	24	60	10.98	141	299	440	70	0.109	0.418	0.527	23 (2.2)	86	23	-
E6	140	24	70	10.93	153	287	440	61	0.102	0.359	0.461	27 (0.5)	72	21	5.4
E7	140	12	50	11.05	175	264	439	63	0.115	0.351	0.466	27 (0.7)	42	18	-

*BET size is the particle size estimated from the S_{ext} value assuming cubical particle shape.

surface area were not possible under the reaction conditions investigated here. The use of shorter reaction times and lower synthesis temperatures resulted in production of ZSM-5 crystals with low relative crystallinity and poor yields.

The samples synthesized from reaction mixtures subjected to varying degrees of evaporation (samples E1-7) have a wider range of relative crystallinity (Table 1). The RC value for these ZSM-5 samples has a stronger correlation with synthesis time and particle size. The samples synthesized after 48 and 72 hours of hydrothermal treatment have RC value around 100%. Samples E3-E6, synthesized for 24 hours exhibited decreased RC as the particle size became smaller. Sample E7, which had the shortest synthesis duration and smallest particle size, also had the smallest RC value. The percent yield of the samples synthesized with the evaporation step follow a trend similar to that of non-evaporated series. The yield remained generally high, with the exception of the largest surface area sample (175 m^2/g), which had a yield of only 42%. The Si/Al remained around 32 for samples with lower external surface area and decreased to around 26 in case of the smallest particle size samples. High zeolite product yield even after partial evaporation of the reaction mixture indicates that the silicon and aluminum precursors are not removed from the solution during the evaporation process.

3.4.2 Surface area and pore volume characteristics.

The external surface area and particle size of the ZSM-5 zeolites synthesized from the reaction mixture without the evaporation step was varied by carrying out the synthesis at different temperatures (140 to 165 ^oC) and reaction times (12 to 72 hours). Generally, hydrothermal treatment at lower temperatures for shorter periods of time leads to production of smaller particles with larger external surface areas. However, the external surface area of the samples synthesized without an evaporation step (N1-N7) did not change much under different synthesis conditions and ranged from 22 to 60 m^2/g for this series of samples. In contrast, the external surface area of the samples synthesized from

reaction mixtures with varying degrees of evaporation (E1 to E7) ranged from 35 m^2/g for the sample hydrothermally treated for 72 hours to 175 m^2/g in the case of the sample synthesized for 12 hours (Table 1) indicating that evaporation can be used as a variable to control the ZSM-5 external surface area and thus, particle size.

The total surface area (S_{tot}) of the zeolite samples varied from 320 to 440 m^2/g. The value of S_{tot} strongly correlates with the value of S_{ext}. The zeolite sample with the smallest S_{ext} of 22 m^2/g also had the smallest S_{tot} of 320 m^2/g. The ZSM-5 sample with highest S_{ext} of 175 m^2/g had S_{tot} = 439 m^2/g. Conversely, the internal surface area (S_{int}) varied little from one zeolite sample to another and remained constant at ~300 m^2/g. Only the ZSM-5 samples with the highest external surface areas of 153 and 175 m^2/g exhibited a decrease of S_{int} to 287 and 264 m^2/g respectively. While S_{int} does not depend on the particle size, it correlates with the relative crystallinity of samples determined by powder XRD. The ZSM-5 samples with the lowest crystallinity also had the smallest S_{int}.

The micropore volume (V_{micro}) of the ZSM-5 samples varied slightly from 0.102 to 0.151 cc/g (Table 1). No significant dependence of micropore volume on the particle size or relative crystallinity of the samples was detected. However, the degree of mesoporosity of the samples varies strongly depending on the external surface area and particle size as shown in Figure 19. As the S_{ext} increases from 22 m^2/g to 122 m^2/g, the mesopore volume increases from 0.085 cc/g to 0.43 cc/g. Further increase of S_{ext} to 153 (E6) and 175 m^2/g (E7) led to smaller V_{meso} values. The decrease of V_{meso} also correlates with smaller RC values obtained for the ZSM-5 nanocrystals of the smallest size. The decrease of mesopore volume in samples E6 and E7 may be the result of extremely small crystals forming denser aggregates or due to the presence of larger amount of amorphous aluminosilicate compared to the other ZSM-5 samples.

Pore size distributions were obtained by applying the BJH model to nitrogen adsorption data as shown in Figure 20. The ZSM-5 sample with the largest crystal size (N1, Figure 20A) has limited mesoporosity, which increases as the zeolite crystal size is

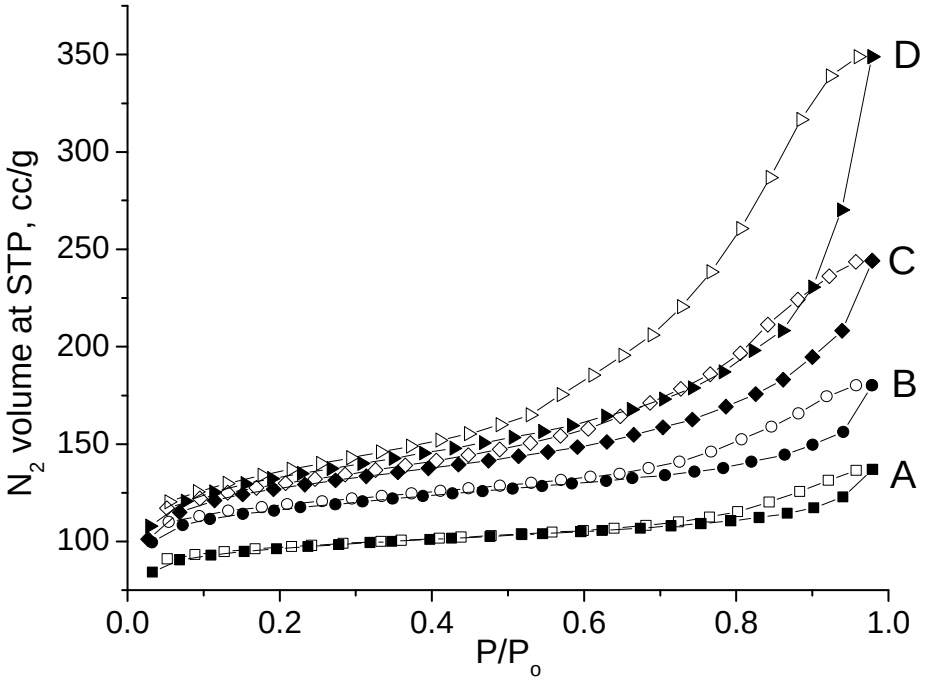

Figure 19. Nitrogen adsorption / desorption isotherms of nanocrystalline ZSM-5 zeolite samples N1 (22 m^2/g) (A), N5 (47 m^2/g) (B), E3 (85 m^2/g) (C) and E4 (122 m^2/g) (D).

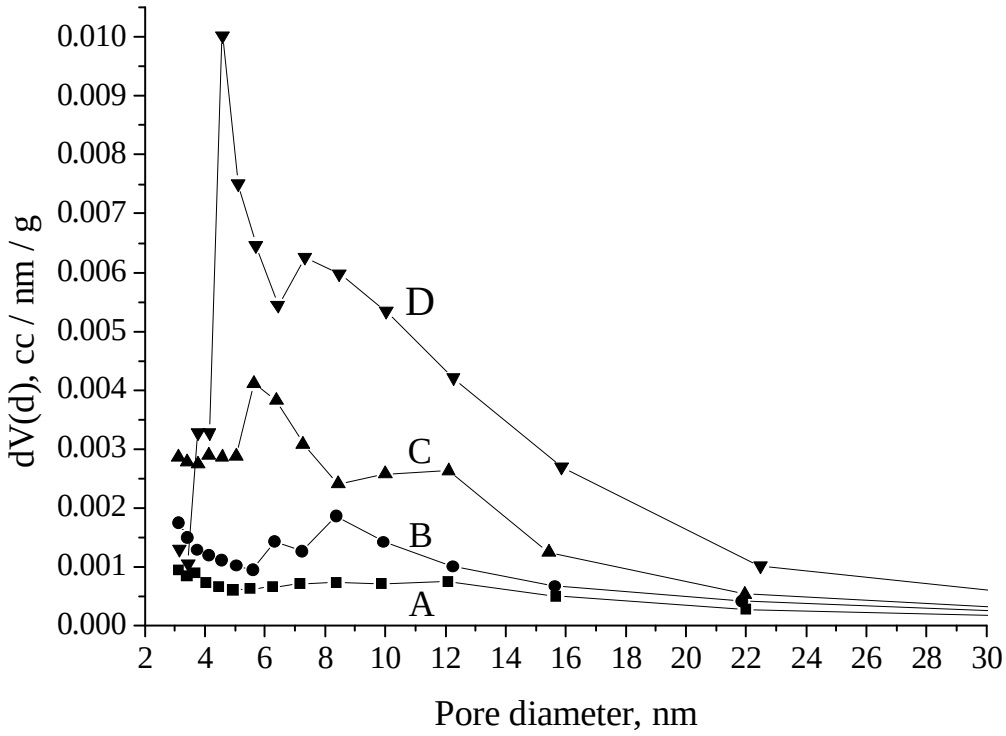

Figure 20. Pore size distribution of the ZSM-5 samples N1 (22 m^2/g) (A), N5 (47 m^2/g) (B), E3 (85 m^2/g) (C) and E4 (122 m^2/g) (D).

decreased (Figure 20B-D). The majority of mesopores have diameters ranging from 4 and 12 nm. The mesopore size distribution in the ZSM-5 samples is wider than in case of conventional mesoporous materials, such as MCM-41. Large zeolite crystals appear to lack mesoporosity. The decrease of particle size results in higher mesopore volume and the shift of the average pore diameter toward smaller sizes. Wider size distribution of mesopores can be attributed to the fact that they are formed by stacked nanocrystals rather than mesopore structure directing agent, such as phenylaminopropyltrimethoxy-silane (PHAPTMS) used by Serrano and coworkers.[102] The use of PHAPTMS allowed the authors to synthesize mesoporous zeolite aggregates with narrowly distributed pores 2 to 4 nm in diameter.

3.4.3. ^{27}Al and ^{29}Si MAS NMR.

Aluminum-27 MAS solid state NMR spectra were collected for select samples in order to determine the effect of particle size on the environment around the aluminum atoms in the framework. The spectra feature a strong chemical shift at 54 ppm, which corresponds to tetrahedrally coordinated aluminum present in the ZSM-5 zeolite (Figure 21).[129] Additionally, a weak peak was observed at 0 ppm indicating the presence of a small amount of extra framework octahedrally coordinated aluminum in the samples. The concentration of extra framework aluminum in the ZSM-5 samples was calculated by integrating the peak at 0 ppm and dividing by the combined integrated intensity of peaks at 54 and 0 ppm and did not exceed 3 at %. A decrease of the ZSM-5 particle size resulted in broadening of the tetrahedral Al peak at 54 ppm. FWHM value increased from approximately 10 ppm for samples N1 and N5 with S_{ext} value of 22 and 47 m^2/g to 16 ppm in the case of samples E4 and E6 with S_{ext} of 122 and 153 m^2/g respectively. The increasing linewidth with decreasing crystal size has been observed previously for nanocrystalline ZSM-5 prepared by seed silanization and was attributed to increasing heterogeneity in the Al local environments.[125, 130] Linewidths of ~12-15 ppm in

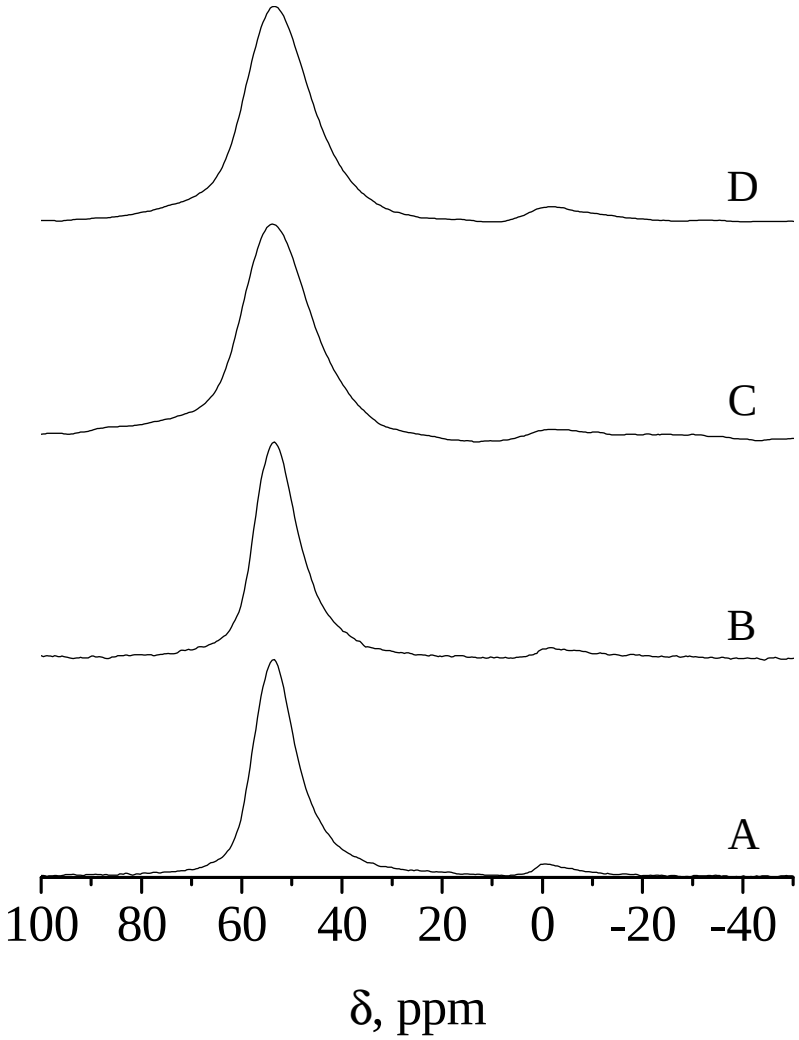

Figure 21. ^{27}Al MAS NMR spectra of calcined ZSM-5 samples N1 (22 m^2/g) (A), N5 (47 m^2/g) (B), E4 (122 m^2/g) (C) and E6 (153 m^2/g) (D)

aluminosilicates have been previously attributed to amorphous silica-alumina materials.[131] So the increasing Al linewidth observed for our samples with the smallest particle sizes (sample E-6) reflects both increasing local heterogeneity and the presence of amorphous silica-alumina materials which is also supported by decreased RC.

Silicon-29 MAS NMR spectra (Figure 22) were recorded for the same samples that were used for ^{27}Al MAS NMR measurements. The spectra contain a strong peak at -111 ppm corresponding to quaternary silicon atoms (Q4 0Al) as well as a shoulder at -100 ppm due to the presence of tertiary silicon atoms (Q3 0Al) in silanol groups located on the surface of the nanocrystalline ZSM-5 and quaternary silicon atoms (Q4 1Al) with one aluminum.[132] The intensity of the peak at -100 ppm was smaller for ZSM-5 samples with lower external surface areas (Figure 22 A, B) and increased for samples with larger external surface areas (Figure 22, C, D) reflecting increasing silanol groups as the external surface area increases. The Q^3 chemical shift also became broader as the external surface area of the ZSM-5 samples was increased.

3.4.4. Transmission Electron Microscopy.

TEM images were collected for ZSM-5 zeolite samples with external surface areas of 22, 47, 122 and 153 m^2/g (Figure 23). Using the TEM images to calculate size distributions (Figure 24), the average particle size and standard deviation (shown in parenthesis) of these samples were 42 (12), 19 (3.9), 6.4 (1.2) and 5.4 (0.96) nm, respectively. The larger zeolite crystals have irregular shapes with some crystals starting to develop a typical MFI rod-shaped morphology (Figure 23 A2). Lattice fringes can also be seen in some particles indicating a well-developed crystal framework (Figure 23A2). The size distribution of large zeolite crystals is fairly broad and ranges from 19 to 72 nm (Figure 24A). The individual crystals form aggregates several hundred nanometers in size (Figure 23 A1). As the size of the individual ZSM-5 crystals decreases, their shape

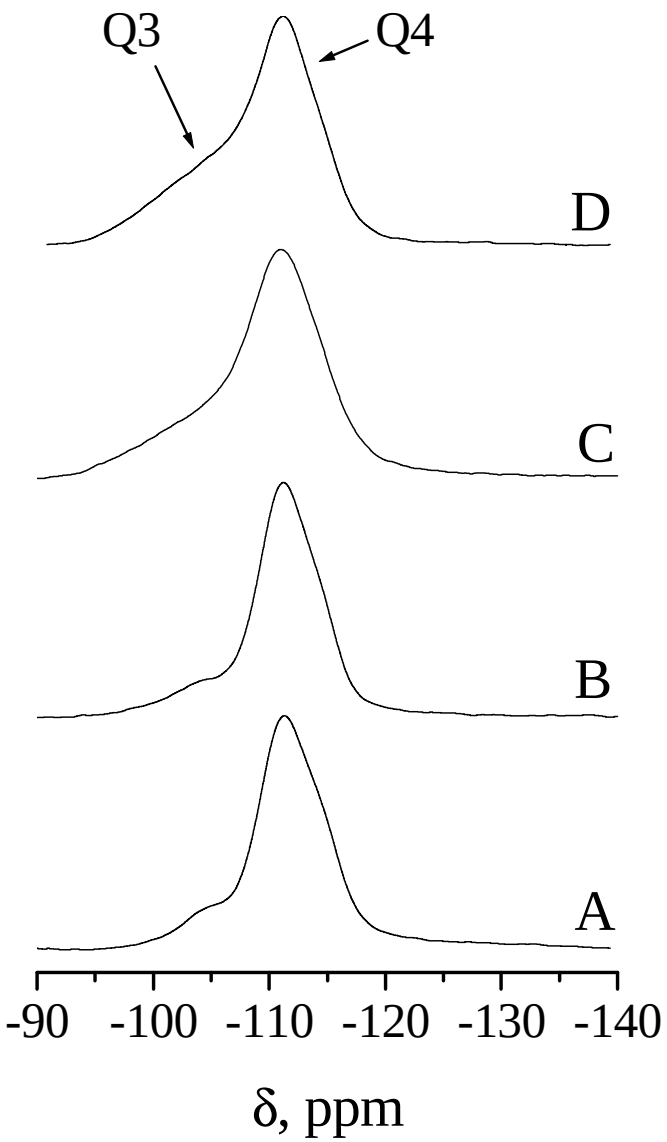

Figure 22. ^{29}Si MAS NMR spectra of calcined ZSM-5 samples N1 (22 m^2/g) (A), N5 (47 m^2/g) (B), E4 (122 m^2/g) (C) and E6 (153 m^2/g) (D)

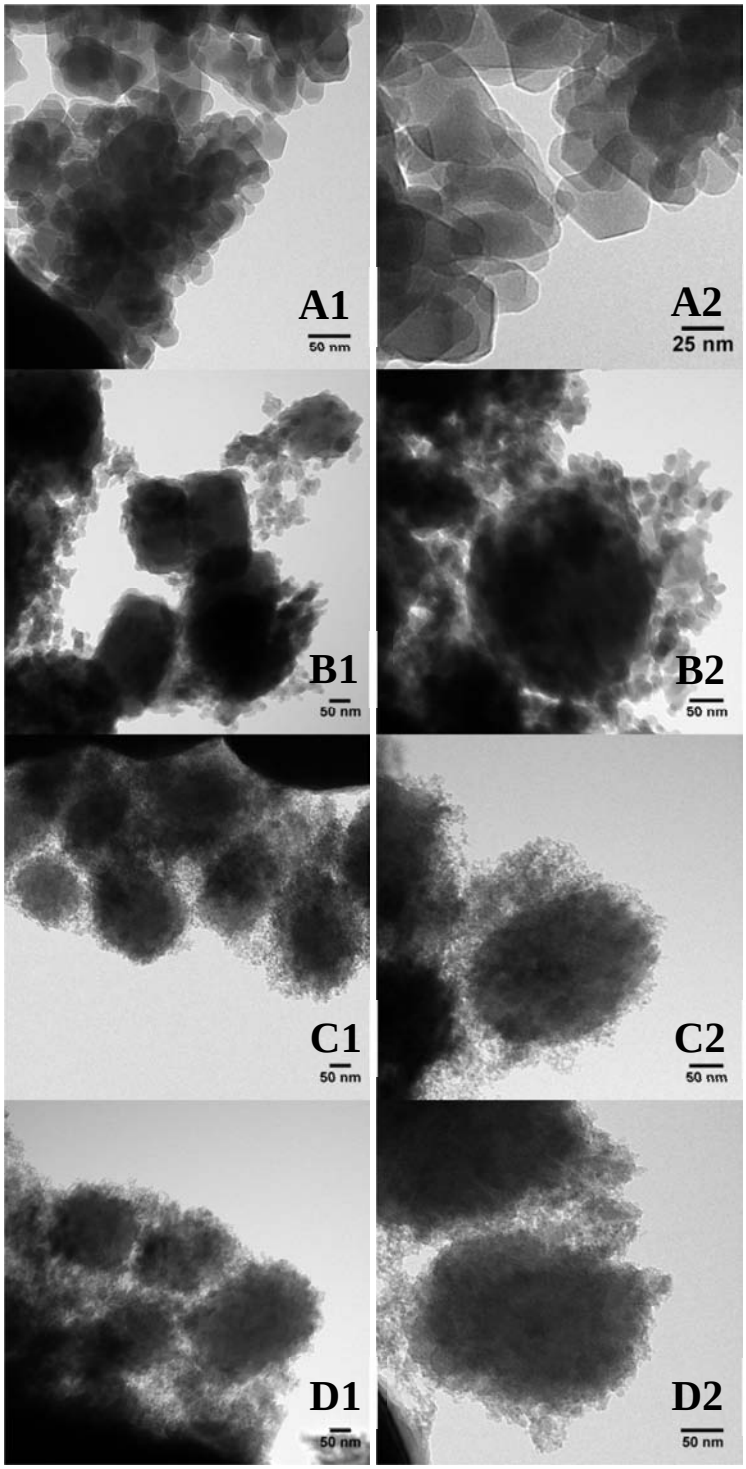

Figure 23. Transmission electron microscopy images of calcined ZSM-5 samples N1 (22 m^2/g) (A), N5 (47 m^2/g) (B), E4 (122 m^2/g) (C) and E6 (153 m^2/g) (D).

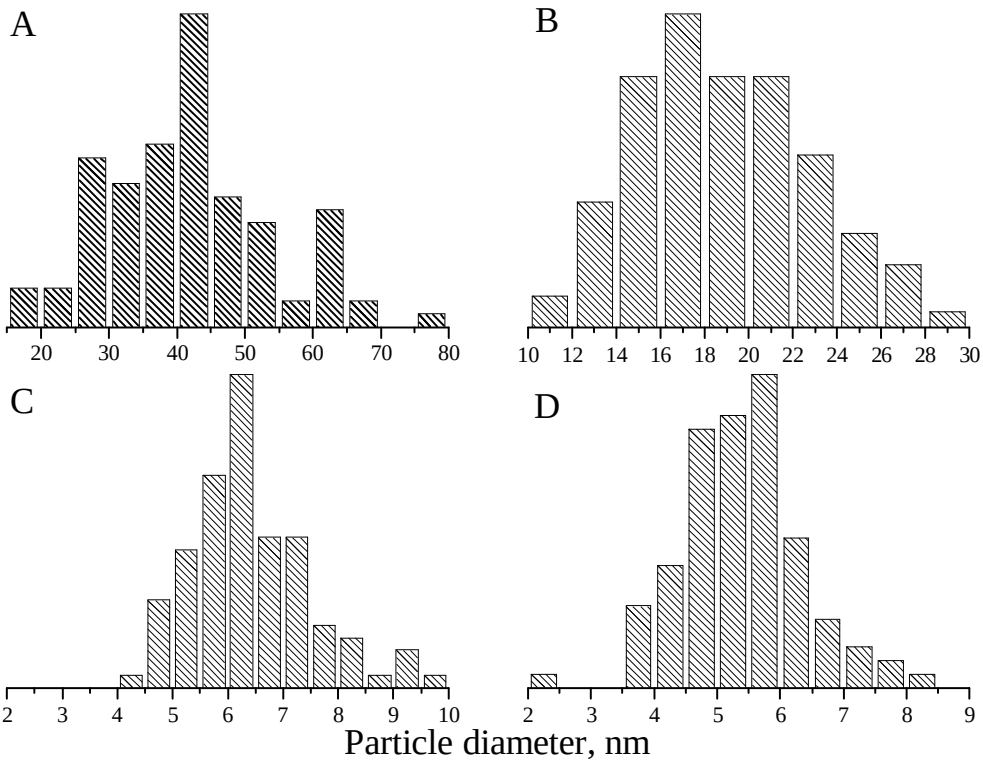

Figure 24. Particle size distribution in ZSM-5 samples N1 (22 m^2/g) (A), N5 (47 m^2/g) (B), E4 (122 m^2/g) (C) and E6 (153 m^2/g) (D).

becomes more spherical and the size distributions more narrow (Figure 23, B2, C2, D2 and Figure 24). The size distribution of crystal sizes for ZSM-5 samples with 42, 19, 6.4 and 5.4 nm average size are shown in Figure 23A-D. Smaller crystals form aggregates, with more spherical and uniform shapes than larger crystals (Figure 23 B1, C1, D1). The aggregate size was found to correlate with the size of individual nanocrystals. The size of ZSM-5 nanocrystal aggregates was 226 nm, 164 nm and 156 nm for single crystal sizes of 19, 6.4 and 5.4 nm, respectively.

The mesoporous aggregates of ZSM-5 nanocrystals under 10 nm in size have a striking similarity with the ZSM-5 zeolite aggregates obtained by Serrano et al.[102] Larger size zeolites synthesized by the authors also lack mesoporosity and their aggregates have irregular shape. The size and shape of the smallest crystals, and the aggregates formed in their study, are similar in to those observed in the study reported here. However, in the case of the ZSM-5 samples synthesized in this work, the particle size and the formation of mesoporous aggregates was controlled by the reaction conditions, such as the synthesis time and the pH, as opposed to the use of an additional structure directing agent in Serrano's study. The fact that no lattice fringes were observed in the smallest zeolite crystals studied in our work is attributed to the insufficient TEM resolutions, and the powder XRD patterns confirm the presence of a crystalline phase.

3.4.5. The effect of pH.

Because the crystallization rate of the zeolites depends on the pH of the reaction mixture, varying the pH can be used to control the size and external surface of ZSM-5 nanocrystals. The decrease of pH observed after rotary evaporation is possibly due to removal of a small amount of template during the evaporation process. Due to the relatively low temperature and short time required for the rotary evaporation of the reaction mixture, no significant interaction between the precursors is expected. The slower crystallization rate of the reaction mixture with pH = 11.52 limits the particle size

range that can be obtained under given conditions. The external surface area of the samples could only be varied between 22 and 60 m^2/g. This slow rate of crystallization does not allow synthesis of smaller crystals while keeping the relative crystallinity and the product yield acceptable. Partial evaporation of the reaction mixture was chosen as a means to vary the pH and crystallization rate, thus controlling the size of synthesized ZSM-5 nanocrystals.

First, two series of samples were synthesized while systematically varying the pH by evaporation from 11.52 (non evaporated, N3-N6) to 11.05 (50% evaporated, E1-2, E4, E7). The samples were hydrothermally treated at 140 ^oC for time period from 12 to 72 hours. A comparison of ZSM-5 samples synthesized at different pH values but with the same synthesis temperature and time is shown in Figure 25. The two ZSM-5 samples synthesized with 12 hours of hydrothermal treatment from reaction mixtures with pH = 11.52 and 11.05 show the largest difference between their S_{ext} values. At longer synthesis time, the difference between the external surface areas of the two series of samples decreases. After 72 hours of hydrothermal treatment, the surface and pore volume parameters of both samples, as well as their relative crystallinity are similar. The higher rate of crystallization in the case of the reaction mixture with pH = 11.05 leads to formation of smaller sized crystals at shorter synthesis times.

To further investigate the role of partial reaction mixture evaporation and the pH on the crystal growth, a series of samples (E3-E6) was synthesized with the same hydrothermal treatment time, while the degree of evaporation was changed. The rate of crystallization steadily increases as the pH of the reaction mixture decreased from 11.52 to 10.93 (Figure 26). The pH value has a major effect on the particle size, external surface area and pore volume of the ZSM-5 crystals. The ZSM-5 samples synthesized at lower pH have smaller sizes. Relative crystallinity and percent yield of the samples is somewhat lower compared to the non-evaporated reaction mixture. One explanation of

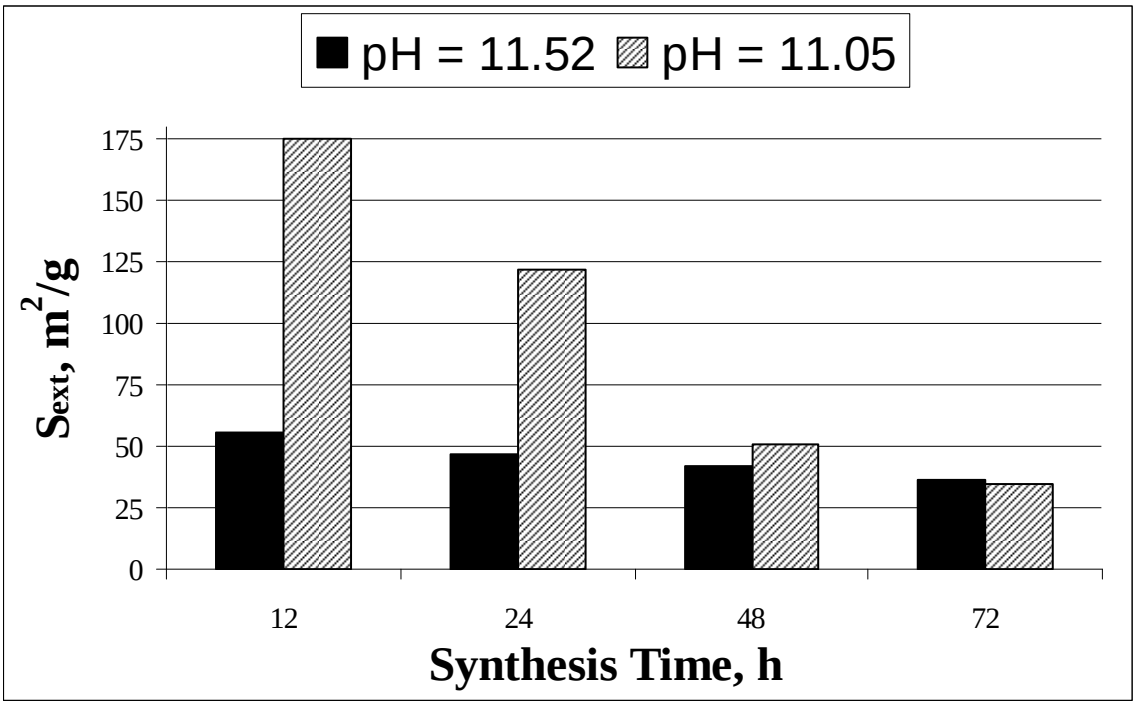

Figure 25. Comparison of S_{ext} values of ZSM-5 samples synthesized from reaction mixture with pH = 11.52 (Samples N6, N5, N4 and N3 in the order of decreasing S_{ext}) and pH = 11.05 (Samples E7, E4, E2 and E1 in the order of decreasing S_{ext}).

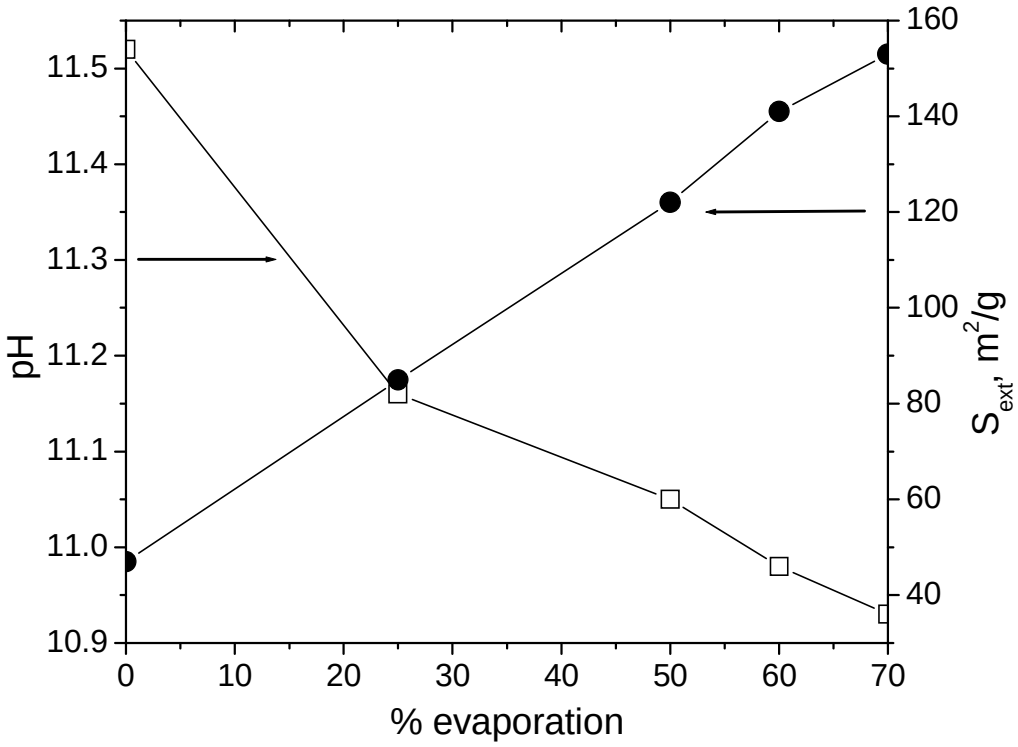

Figure 26. The effect of evaporation on reaction mixture pH and external surface area of the ZSM-5 nanocrystals. The samples were synthesized at 140 ^{o}C for 24 hours. Samples C4, E3, E4, E5 and E6 are shown in the graph in the order of increasing S_{ext}.

the lower RC is the increase of the amorphous particles in the sample. Another possible explanation for lower RC values of the ZSM-5 samples with the smallest crystal size is the presence of a large amount of slightly distorted surface atomic planes in the zeolite crystals due to surface relaxation. In this case, the crystallinity of ZSM-5 samples measured by XRD may be slightly underestimated.

S_{ext} was previously used to estimate the crystal size of Silicalite-1, ZSM-5 and NaY zeolites,[22, 27] because S_{ext} was found to correlate very well with the crystal size. The crystal size calculated from S_{ext} was compared to the size measured from TEM images and found to follow the same trend. However, the average particle size calculated using S_{ext} values underestimates the ZSM-5 crystal size when compared with TEM crystal size measurements (Table 1). The difference between the particle sizes determined by the two methods is most likely due to aggregation of the ZSM-5 nanocrystals that makes a fraction of their surface areas inaccessible for nitrogen adsorption.

29-silicon MAS NMR data correlates with other methods and provides additional evidence for presence of small zeolite particles within the mesoporous aggregates. The intensity of Q3 peak in the spectra increases in samples with higher surface area. Since Q3 silicon atoms are only located on the external surface of the crystals, the increase of the respective chemical shift intensity indicates the presence of smaller crystals within the aggregates. The width of the Q3 peak also increases in the small particles, suggesting that the environment around the surface silicon atoms is not uniform.

A proposed scheme for the formation of mesoporous aggregates is shown in Figure 27. The surface of the zeolite crystals is negatively charged at the pH of the reaction mixture. The negatively charged surface can interact with the excess tetrapropylammonium cations present in the synthesis mixture. TPA^+ cations can electrostatically bind to the surface of the particles and participate in formation of mesopores between the nanocrystals provided the latter have a sufficiently small and uniform size. In the case of bigger ZSM-5 crystals, the effect of the TPA^+ cations layer

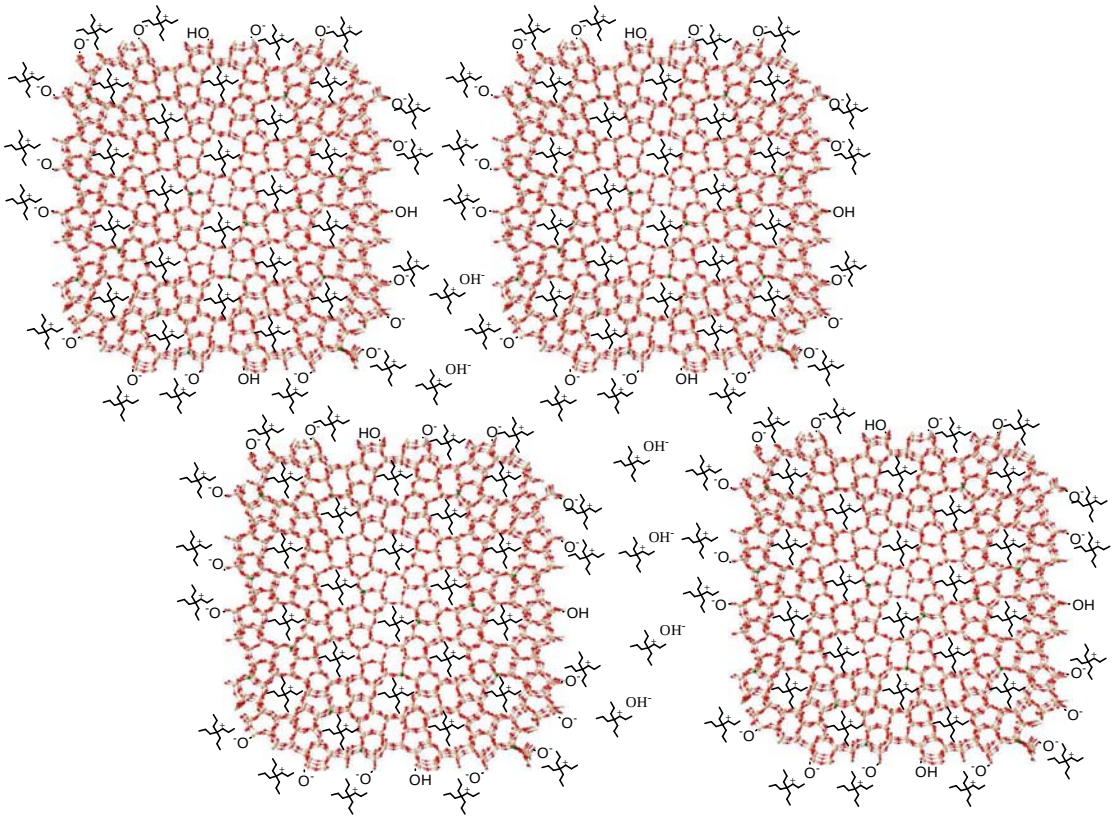

Figure 27. Schematic representation of ZSM-5 nanocrystals forming mesoporous aggregates.

around the particles does not lead to formation of mesopores because large crystals of irregular shape will stack and form macropores within the crystal aggregates.

3.5. Results and Discussion – Mesoporous Naβ synthesis.

3.5.1. Synthesis Conditions

The synthesis gels were rotary evaporated in order to remove the ethanol produced during hydrolysis of TEOS as well as some water, and to increase the concentration of the reacting species in the gel. The concentration of the synthesis gel was then adjusted to the value that was found optimal for micro/mesopore composites synthesis and to the initial volume in order to provide insight into the effect of synthesis gel concentration on the zeolite crystallization process. Synthesis gels with higher concentration produced an amorphous gel after hydrothermal treatment while greater dilution resulted in a slower rate of crystallization as well as the absence of nanocrystals' aggregation into mesoporous composites. The initial pH of the synthesis gel was 12.31. Partial rotary evaporation and subsequent adjustment of synthesis gel volume to 50% of the initial volume resulted in a decrease of pH to 12.18. The samples synthesized from the synthesis gel with pH = 12.18 are labeled as E series. Adjustment of the volume to 100% of the initial volume after rotary evaporation further decreased the pH to 11.91, and the reaction mixtures with this pH were used to synthesize the N series of samples. The decrease of pH after partial rotary evaporation and volume adjustment may be due to the solvent effect, as the ethanol is removed from the reaction mixture. It may also be attributed to a loss of a small amount of the template cations during the evaporation process.

The synthesis yield of calcined zeolite material (Table 2) was approximately 60-65% of the total theoretical yield, and around 50% for the samples with smallest particle size in both series. These values are somewhat lower than the yields that were observed

Table 2. Characterization summary of Naβ zeolite samples.

name	T ^{o}C	Time, hrs	V/V$_i$, %	pH	Yield, %	S$_{ext}$, m^2/g	S$_{total}$, m^2/g	S$_{micro}$ m^2/g	V$_{total}$, cc/g	V$_{micro}$, cc/g	V$_{meso}$, cc/g	Si/Al	RC, %	BET size, nm*
N1	150	72	100	11.9	74	21	487	466	0.559	0.306	0.253	19	94	155
N2	135	96	100	11.9	50	140	590	450	0.672	0.196	0.476	18	102	23
E1	130	30	50	12.18	58	79	649	570	0.647	0.233	0.414	19	99	41
E2	150	20	50	12.19	68	83	611	528	0.634	0.233	0.401	16	104	39
E2	145	20	50	12.18	65	91	602	511	0.589	0.231	0.358	18	94	36
E4	135	20	50	12.18	61	99	672	573	0.731	0.220	0.511	19	99	33
E5	125	30	50	12.18	62	105	645	540	0.631	0.231	0.400	19	92	31
E6	120	34	50	12.18	47	133	647	514	0.651	0.217	0.434	18	92	24

*BET size is the particle size estimated from the S$_{ext}$ value assuming cubical particle shape.

.during synthesis of mesoporous ZSM-5 zeolite,[133] but comparable to yields obtained for similar zeolite beta materials.[123]

3.5.1. Structural characterization

Powder XRD patterns of the zeolite beta samples are shown in Figure 28 and contain two major reflections at 7.8 and 22.5 2θ, which are characteristic of Beta (BEA) type zeolite. No indication of impurities was observed in the XRD patterns of the samples. Relative crystallinity (RC) of the samples before calcination was significantly higher than that of the external reference. The reflection of the 22.5 2θ peak used for RC decreases after calcination and consequently the RC values of calcined samples decreased and became very close to that of the external reference.

The silicon to aluminum ratio (Si/Al) in the synthesized mesoporous zeolite beta samples was determined by ICP-OES. The Si/Al is similar for samples synthesized in different reaction conditions and ranged between 16 and 18. The concentration of the synthesis gel did not affect the Si/Al ratio in the samples. The Si/Al ratio in the solids is lower than in the synthesis gel, which was Si/Al = 25. This observation is consistent with the study by Mintova and coworkers, who synthesized zeolite beta nanocrystals with silicon to aluminum ratio ranging from 25 to 250 in the precursor gel, while the corresponding ratios in the final solids varied between 14 to 42.[93]

^{27}Al MAS NMR spectra of the zeolite beta samples were recorded under ambient conditions in order to monitor the coordination state of aluminum. In the ^{27}Al MAS NMR spectra of as synthesized zeolite beta samples (Figure 29), one peak is observed at approximately 51 ppm and is attributed to tetrahedrally coordinated aluminum atoms. Calcination of zeolite beta samples resulted in appearance of a second peak at approximately 0 ppm in the ^{27}Al MAS NMR spectra, which is assigned to aluminum in octahedral coordination (Figure 30). The presence of a peak with a chemical shift of ~0 ppm was observed for all calcined samples and was slightly more pronounced in the case

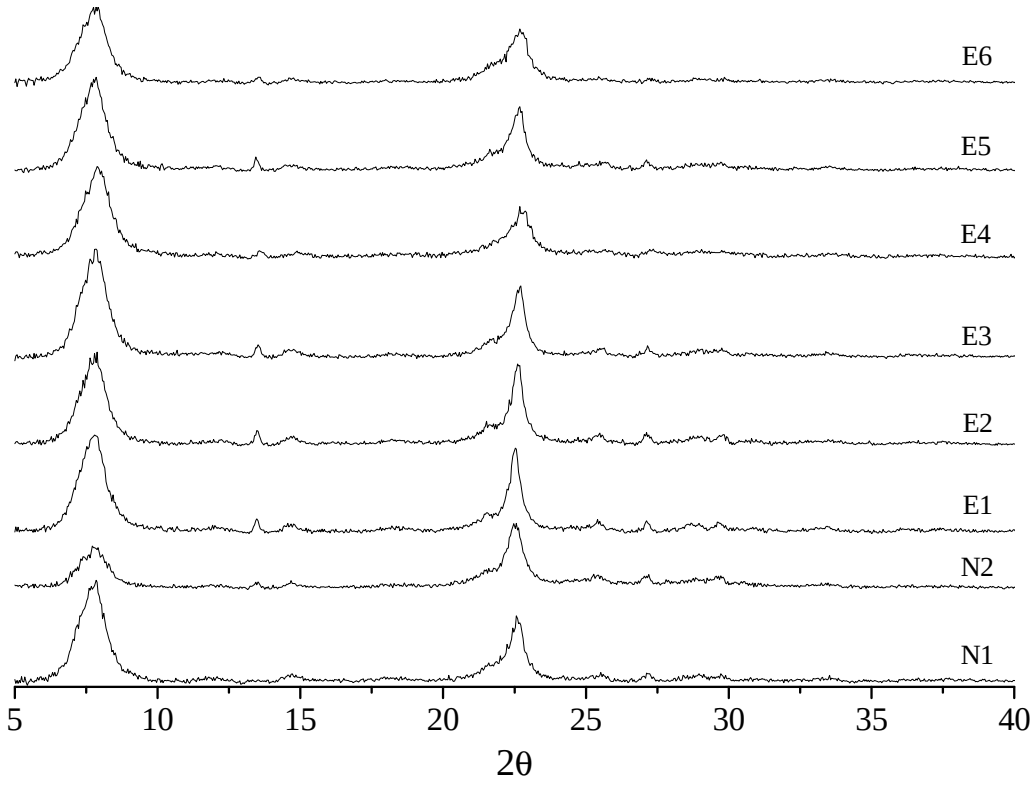

Figure 28. Powder XRD patterns of calcined Naβ zeolite samples.

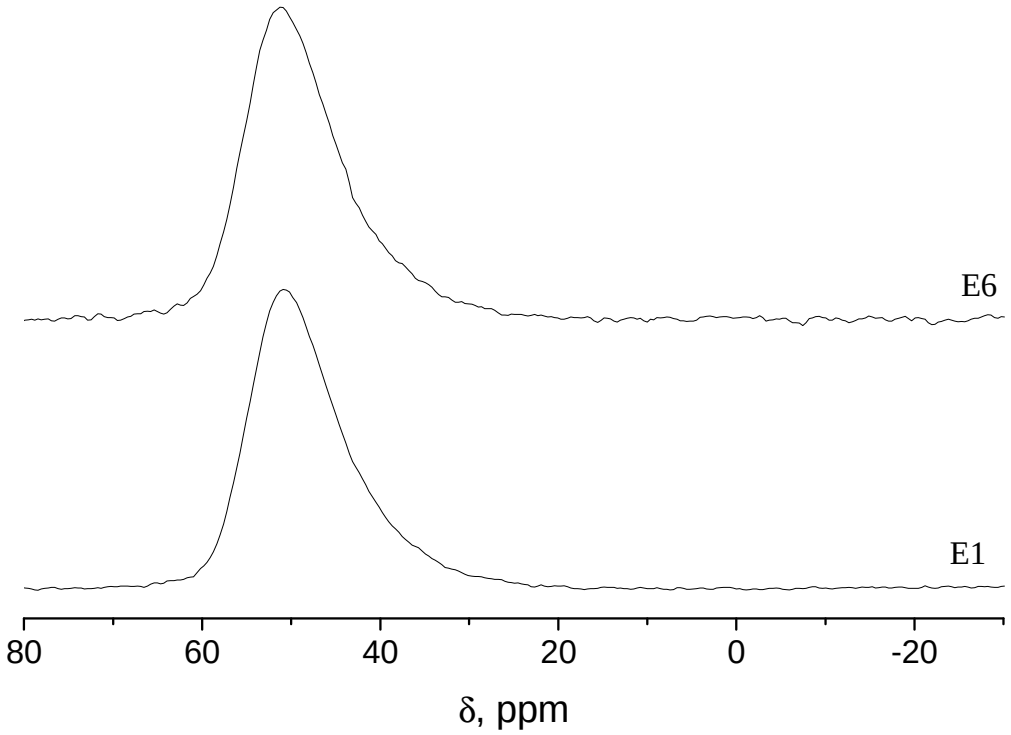

Figure 29. ^{27}Al MAS NMR spectra of as-synthesized Naβ zeolite samples.

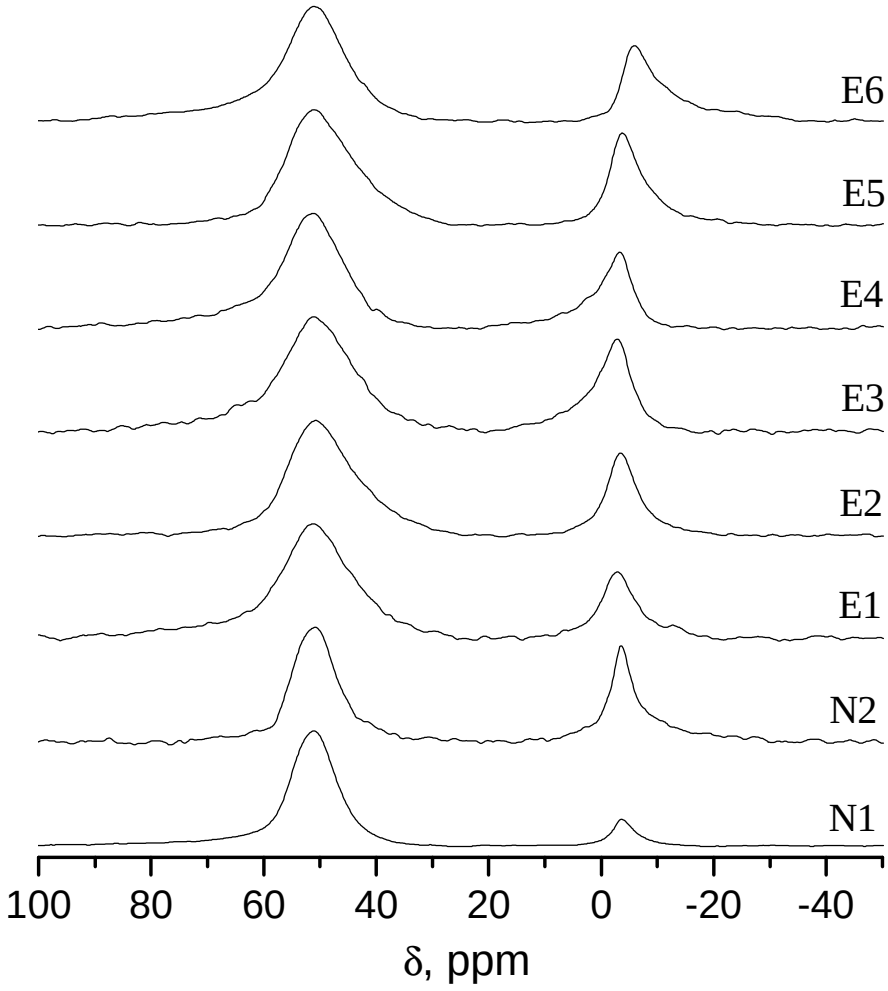

Figure 30. ^{27}Al MAS NMR spectra of calcined Naβ samples.

of smaller zeolite crystals (N2, E1-E6) than in the case of the sample with largest crystal size (Sample N1). Previous studies have shown that the coordination state of aluminum in calcined zeolite beta is reversible, and octahedral aluminum can be restored back into its tetrahedral coordination by treatment with ammonium nitrate.[134] Further studies of this phenomenon indicated that octahedrally coordinated aluminum remains a part of the zeolite framework and the two extra coordination bonds are formed with a water molecule and a hydronium ion.[134, 135] Furthermore, the presence of Lewis acid sites in the zeolite can be beneficial for certain reactions, such as stereoselective reduction of ketones.[136]

^{29}Si MAS NMR spectra of the zeolite beta samples are shown in Figure 31. The spectra display a strong peak at -110 ppm and a shoulder at -100 ppm, which correspond to the presence of Q^4 and Q^3 coordinated silicon atoms in the zeolite framework, respectively.[121] In the spectrum recorded for Sample N1 with the smallest external surface area and largest crystal size, the Q^3 peak is weaker but better resolved from the Q^4 peak.

Decreasing the particle size broadens the Q^3 shoulder, while its integrated intensity increases, which is related to the increase in the number of surface silanol groups. Broadening of the Q^3 chemical shift is due to a decreased homogeneity of the surface silicon atoms environment in comparison with larger crystals. It should be noted that the trend in the change of Q^3 chemical shift intensity is similar to that observed for nanocrystalline ZSM-5 zeolite samples [133].

3.5.3. Surface area and porosity

Nitrogen sorption isotherms were collected in order to determine the external, and mesopore surface areas and pore volumes, as well as the mesopore size distribution in the zeolite aggregates. The nitrogen sorption isotherms (Figure 32) are a type IV isotherm which exhibits a hysteresis loop, indicating the presence of mesopores in the samples.

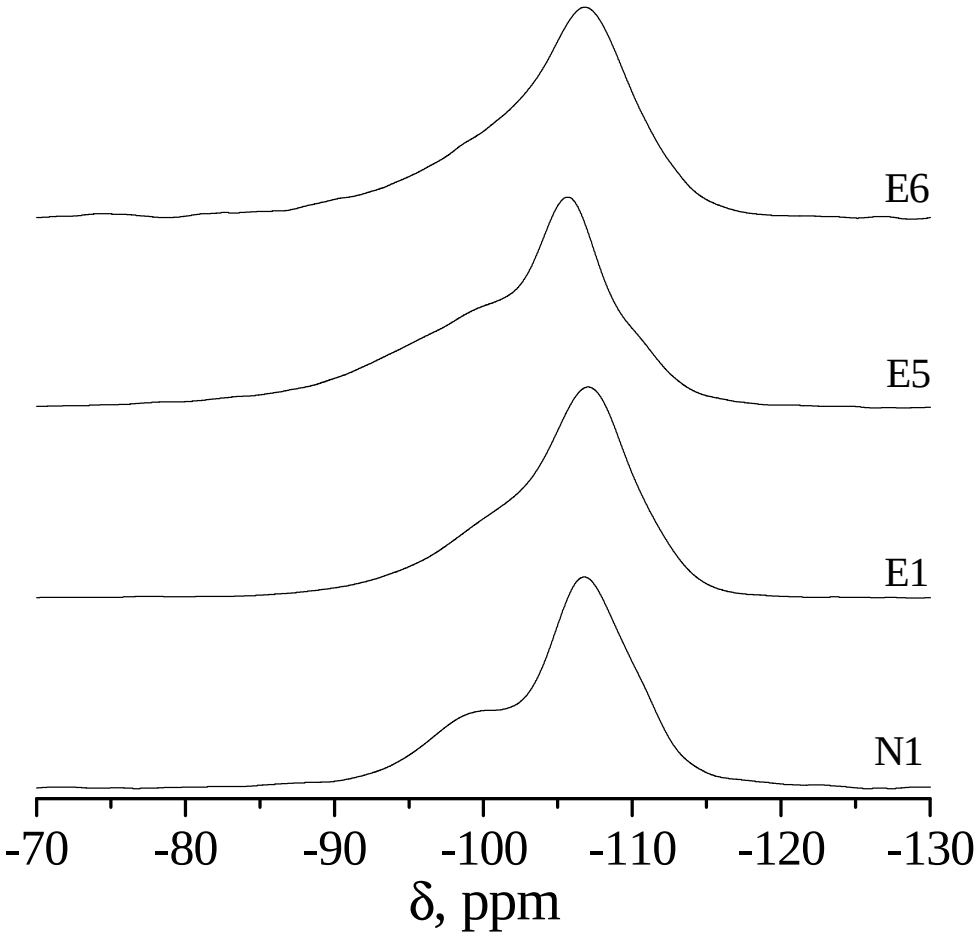

Figure 31. 29Si MAS NMR of calcined Naβ zeolite samples.

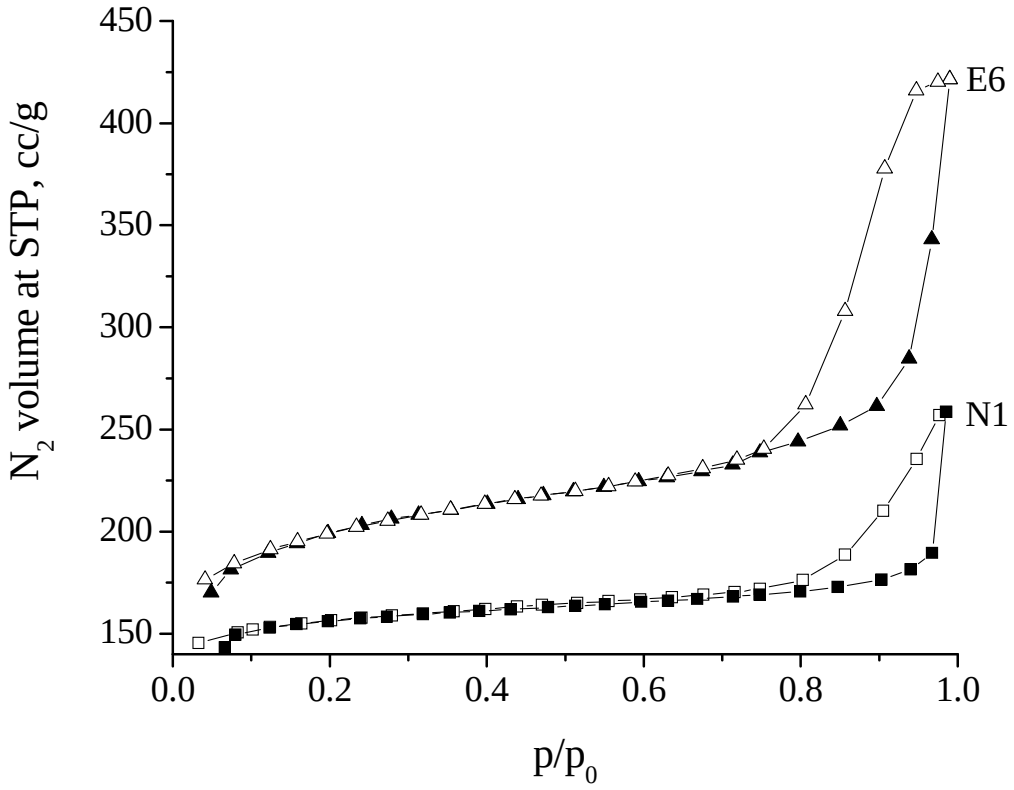

Figure 32. Nitrogen sorption isotherms of calcined Naβ zeolite samples. Filled symbols represent the adsorption branch of the isotherm, open symbols represent the desorption branch.

The total specific surface area (S_{tot}) values of the nanocrystalline zeolite beta samples vary from 490 to 670 m^2/g. In general, samples with smaller crystal sizes have higher total surface areas than the samples with larger crystals. Sample N1 with an estimated crystal size of 200 nm has the smallest S_{tot} value (487 m^2/g) of all of the samples in both series. Samples E1 through E6 synthesized from concentrated reaction mixtures have similar S_{tot} values ranging from 602-672 m^2/g.

The external surface area of the zeolite beta samples strongly depends on the reaction conditions. Lower temperatures and shorter synthesis durations lead to larger values of S_{ext}. This dependence is associated with the relationship between the crystal size and the external surface area. The average size of the zeolite crystals within the aggregates can be estimated from the value of the external surface area.[137] A similar formula was derived for zeolite beta and is given below:

$$S_{ext} = \frac{3252}{x} \qquad (13)$$

where x = average crystal size in nm.

Using this equation, the external surface area (S_{ext}) from the E series in Table 2 was used to calculate the average crystal sizes which ranged from 25 to 41 nm. This range was found to be close to the individual crystal size estimated from TEM images to range from 16 to 40 nm (Table 2).

The micropore volume of the zeolite samples showed a behavior similar to micropore surface area and did not vary significantly for the samples synthesized from concentrated reaction mixtures. The small difference between the micropore volume values of the zeolites is due to its dependence on the degree of crystallinity. Since the synthesized zeolite beta samples have similar relative crystallinity, it is reasonable to expect similar micropore volume parameters. Conversely, micropore volumes of the two samples synthesized from a dilute reaction gel are significantly different from the

mesoporous samples as well as from each other. The V_{micro} of N1 was 0.306 cc/g and was the highest of all of the samples due to the large crystal size. V_{micro} of N2 was 0.196 cc/g, which was slightly lower than the V_{micro} values of the E1-E6 samples which ranged from 0.217-0.233 cc/g.

The mesopore volumes of the zeolite samples changed significantly depending on the reaction conditions. Sample N1 with largest crystals had the smallest mesopore volume, which increased in the case of zeolite samples with smaller crystals. Interestingly, zeolite beta sample N2 showed a high mesopore volume, which was attributed to the presence voids between the crystals that do not have any strong bonds between each other and can be dispersed as individual particles as shown by TEM.

The pore size distribution in the zeolite aggregates was compared for samples N1 and E6 (Figure 33), which have the largest disparity between their pore volume and surface area properties. Sample N1 shows a broad distribution of mesopores that occupy a small volume, and the majority of mesopores are over 10 nm in size. Sample E6 has a significantly higher mesopore volume and the pore size distribution plot contains two peaks, around 3 nm and 15 nm. The smaller pores are attributed to intercrystalline distance within the aggregates whereas the bigger pores are likely to originate from the inter-aggregate distances.

Transmission electron microscopy images of zeolite beta samples were collected in order to determine the effect of synthesis conditions on the size and morphology of the nanocrystals and their aggregates (Figure 34). The zeolite samples (E1 and E6) with external surface areas of 79 m^2/g, and 133 m^2/g as well as the samples N1 and N2, synthesized from diluted reaction mixture were analyzed. The aggregates of larger crystals (sample E1) are of cubical shape with smooth edges and have an average size of approximately 140 nm. The edges of the aggregates consist of layered nanocrystals, which have their lattice fringes aligned uniformly within the aggregate. The parallel lattice fringes have been observed previously for nanocrystalline zeolite beta.[138]

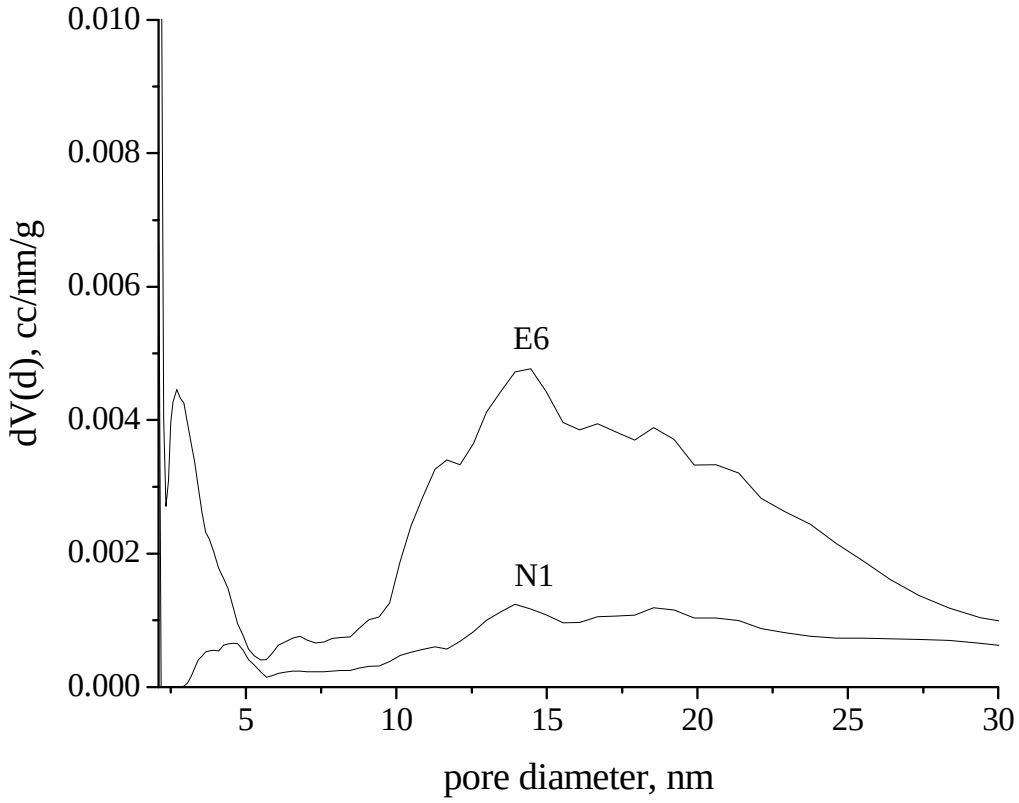

Figure 33. Pore size distribution in calcined Naβ zeolite samples.

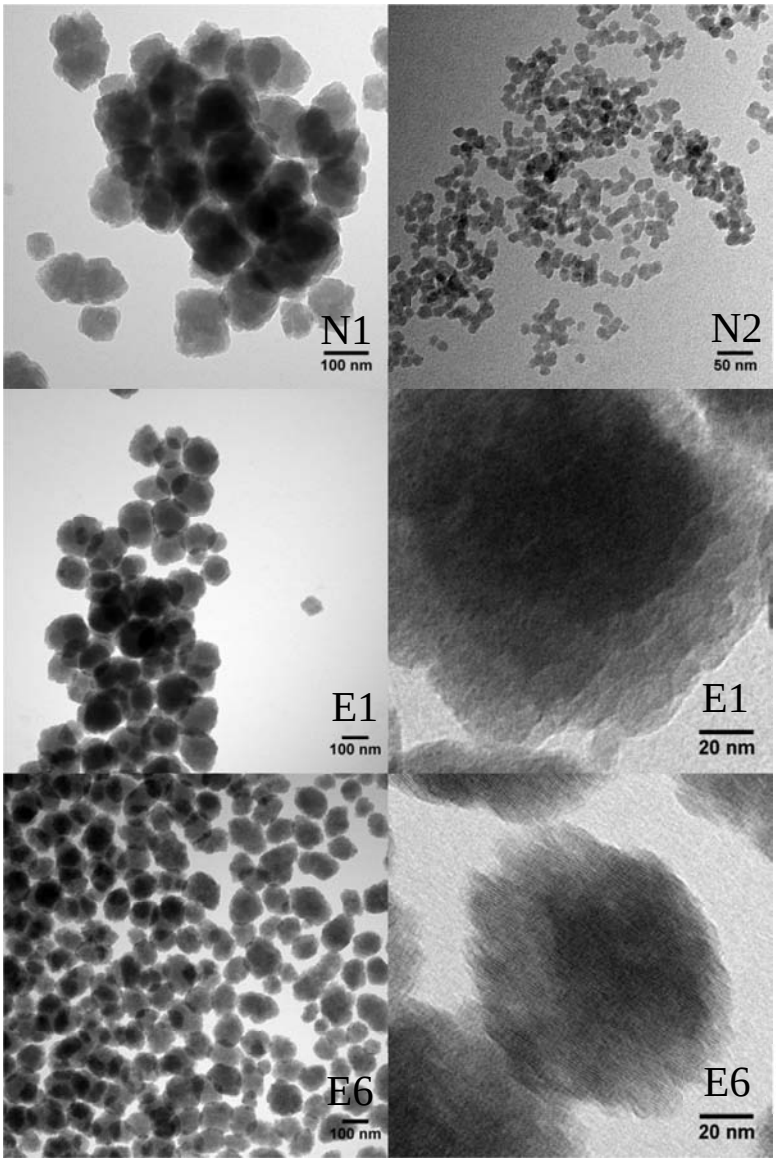

Figure 34. TEM images of calcined Naβ samples N1, N2, E2 and E6

The aggregates of smaller crystals (sample E6) have a less regular shape and their edges are rougher than in the case of the sample with larger crystals. The average size of the aggregates slightly decreases to approximately 120 nm. Lattice fringes can clearly be seen in the case of smaller crystals, and they are aligned within the aggregates as well. An individual crystal size for the Samples E1 (79 m^2/g) and E6 (133 m^2/g) was estimated from TEM as 40 and 16 nm respectively. Kuechl and coworkers observed ~100 nm aggregates when using modified synthesis conditions for preparing zeolite beta with Si/Al~20 based on Camblor's study.[29, 138] Similar, but larger zeolite beta aggregates (~500 nm) are observed by Aguado and coworkers when organofunctionalized zeolite seeds were used in the zeolite beta synthesis.[123]

TEM images of two zeolite beta samples synthesized from a dilute reaction mixture with pH = 11.90 were collected to compare the effect of the synthesis gel concentration on the degree of aggregation of nanocrystals. Sample N2 with S_{ext} = 140 m^2/g consists of crystals with a narrow particle size distribution of about 20 nm (Figure 34 N2). The crystals are well dispersed and do not form aggregates. Sample N1 with S_{ext} = 21 m^2/g formed larger particles with the average size of 200 nm. While the former sample has a large external surface area and latter sample has a convenient particle size, they lack the desired properties, such as formation of aggregates (sample N2) or sufficient external surface area (sample N1). By varying the concentration of the reaction mixture it is possible to obtain zeolite beta nanocrystals with comparable external surface areas but very different crystal morphologies (samples N2 and E6).

3.5.4. Controlling zeolite-Beta crystal size and morphology

The zeolite crystal size and the corresponding value of the external surface area have a strong dependence on the reaction temperature and time as well as the concentration of the reacting species and the pH conditions. Larger zeolite crystals were obtained at higher synthesis temperatures and longer hydrothermal treatment times. The

synthesis temperature can be decreased to as low as 120 ^{o}C while keeping the reaction time reasonably short.

One reaction parameter that had a profound effect on the morphology of the zeolite particles was the concentration of reactants in the synthesis gel. Hydrothermal treatment of reaction mixtures with pH = 11.91 resulted in formation of non-aggregated nanocrystals under 20 nm in size or large zeolite particles with small external surface areas and low mesopore volumes. Synthesis from concentrated reaction mixtures produced zeolite nanocrystals with large external surface areas that form mesoporous aggregates over 100 nm in size. Longer hydrothermal treatment of concentrated reaction mixtures was accompanied by the growth of zeolite crystals and a decrease in their external surface areas.

Further insight can be obtained from the work of Lobo et al. in which the mechanism of zeolite beta nucleation and growth was investigated.[137] In their study, it was shown that aluminum-containing secondary particles (defined as having dimensions of 6-50 nm) in the synthesis mixture exhibit instability and aggregate into larger tertiary particles (defined as having dimensions of >200 nm) when heated. The aggregation is likely to proceed due to weak repulsive forces between the aluminum-containing particles. In our study, it is possible that similar aggregation of aluminum-containing particles is occurring in the concentrated reaction mixtures to produce mesoporous zeolite beta aggregates and that this is the source of the mesoporosity. In the less concentrated solutions, the aluminum containing particles show less tendency to aggregate and therefore do not form the mesoporous aggregates. Further studies of the synthesis of beta, particularly high silica beta, could provide support for this hypothesis.

3.6 Conclusions.

Hierarchical zeolite materials are an emerging and important class of catalysts for a variety of reactions. In this study, we presented a facile method of synthesizing ZSM-5

and β zeolite nanocrystals that form mesoporous aggregates. The method employs one type of structure directing agent, TPA^+ or TEA^+ cations for ZSM-5 and β synthesis respectively. The effects of hydrothermal treatment temperature, synthesis duration and pH of the reaction mixture on the crystal size and the degree of mesoporosity were studied. We have shown that ZSM-5 crystals between 5.5 and 40 nm with narrow particle size distributions can be formed by appropriately tuning the synthesis parameters. The ZSM-5 sample (E4) with average crystal size of 6.4 nm and external surface area of 122 m^2/g was found to have the highest degree of mesoporosity, while its relative crystallinity and yield remained high. The method described here provides an efficient, facile route to the preparation of high quality nanocrystalline ZSM-5 materials with a single template system.

The synthesis of zeolite beta (Si/Al ~18) with different morphologies – isolated nanocrystals and mesoporous aggregates of nanocrystals has been demonstrated. The mesopore volume and the external surface area of the samples vary depending on the reaction conditions and nanocrystals size. Control of the synthesis gel concentration is a useful tool for tuning the zeolite properties for specific applications. The use of concentrated synthesis gels results in mesoporous aggregates of nanocrystals and diluted reaction mixtures are used to synthesize non-aggregated zeolite nanoparticles.

The ability to control the zeolite morphology and thus the porosity has important implications for molecular transport in zeolites and potentially for catalysis. With this synthetic method, hierarchical ZSM-5 and β materials will be more easily accessible for catalytic applications.

Comparison of hierarchical ZSM-5 and β zeolite synthesis reveals some similarities and differences in both reaction conditions leading to formation of mesoporous aggregates and their morphology. For both zeolites, the temperature and synthesis time act similarly, resulting in formation of smaller crystals, which have higher mesoporosity. On the other hand, the change of OH^- / SiO_2 ratio at constant H_2O / SiO_2

ratio had a profound influence on the crystallization of ZSM-5 allowing formation of very small crystals within mesoporous aggregates, whereas for zeolite β the change of H_2O / SiO_2 was required in order to achieve mesoporosity. Another difference in reaction parameters between ZSM-5 and β is the amount of SDA required for obtaining small crystals, which needs to be higher in the case of β zeolite.

Transmission electron microscopy shows that morphology of mesoporous aggregates is also different for ZSM-5 and β. The difference between the size of individual crystals and the size of aggregates is significantly higher in the case of ZSM-5 zeolite (~6 nm crystals versus 300 nm aggregates) than for zeolite β (~15-20 nm nanocrystals in 120 nm aggregates). The zeolite β crystals appear to be more densely packed within the aggregates than ZSM-5 crystals. At the same time, the more open framework of zeolite beta results in higher pore volumes and surface areas. One goal for future work on mesoporous zeolite β synthesis is increasing the size of aggregates while keeping the dimensions of the primary crystals at the current level.

The mesoporous ZSM-5 synthesis results were published in Microporous and Mesoporous Materials, year of 2010, volume 137, pages 92-100, and authored by Petushkov, Yoon, and Larsen. The mesoporous zeolite β synthesis results were published in Microporous and Mesoporous Materials (*in press*), and authored by Petushkov, Merilis and Larsen.

CHAPTER 4

PREPARATION OF TRANSITION METAL EXCHANGED NANOCRYSTALLINE ZEOLITES FOR LEAN DENOX CATALYSIS

4.1 Abstract

Nanocrystalline zeolites, β, ZSM-5 and Y, were exchanged with manganese, vanadium, iron, copper, tin and cerium to prepare singly and doubly exchanged zeolites. The zeolites were characterized by powder x-ray diffraction, inductively coupled plasma/optical emission spectroscopy, scanning and transmission electron microscopy, and nitrogen sorption isotherms. Zeolite particle and aggregate sizes ranging from approximately 30 to 500 nm were used in this study with specific surface areas ranging from ~350-580 m^2/g. The metal-loaded zeolites were evaluated for lean de NOx catalysis with and without added platinum.

4.2 Introduction

Zeolites have been widely studied as potential catalyst materials for controlling automotive gas emissions.[43, 58-60] Typically, the zeolite host is loaded with an active catalytic species such as a transition or precious metal. These metal-exchanged zeolites have been evaluated for deNOx catalytic processes ranging from direct decomposition of NOx to the selective catalytic reduction (SCR) of NOx with hydrocarbons, ammonia and/or urea. Diesel engines pose particular challenges because oxygen is always in excess making oxidation of hydrocarbons and carbon monoxide relatively straightforward but rendering the reduction of NOx under lean conditions difficult.[139] Essentially the problem is that oxygen binds strongly to metal sites in deNOx catalysts, thus poisoning the metal surface toward NO adsorption followed by reduction to nitrogen. A reductant is required to remove the surface bound oxygen and free up the surface for NO adsorption and reaction.

Recently, nanocrystalline zeolites (zeolites with crystal sizes of 100 nm or less) and hierarchical zeolite structures with both micropore and mesopore structures have emerged as potentially important catalytic materials. The advantages of nanocrystalline zeolites or zeolite hierarchical structures for catalysis are the improved mass transfer properties, which in turn may lead to decreased catalyst coking, and more facile reactant and product diffusion.[18, 101-103, 105] Many reports of the synthesis of nanocrystalline zeolites ZSM-5, Y and Beta have appeared in the literature and there are several observations of improved catalytic activity for nanocrystalline zeolites relative to conventional micron-sized zeolites. For example, the selective catalytic reduction of NO with urea on nanocrystalline NaY was reported to produce fewer undesirable side products such as biuret and this was attributed to the smaller crystal size.[140] Recent reports have indicated that microporous/mesoporous zeolites have improved catalytic properties.[103-105] Nanocrystalline zeolites, ZSM-5, β and Y were synthesized with systematically varied sizes, were loaded with different active components, such as manganese, vanadium, iron, copper, tin, cerium and platinum and were extensively characterized. Then, the zeolite samples were tested for NOx reduction under lean burn conditions.

4.3. Experimental Section

4.3.2 Synthesis of NaZSM-5

ZSM-5 nanocrystals were synthesized from the reaction mixture with the following composition: 25 TEOS: 1 $NaAlO_2$: 1000 H_2O: 9 TPAOH, where TEOS = tetraethylorthosilicate and TPAOH = tetra-n-propylammonium hydroxide.

First, the template (TPAOH) sodium aluminate and water were stirred in a RB-flask until all of the sodium aluminate was dissolved. Next, TEOS was added and the mixture was stirred overnight. The reaction mixture was rotary evaporated at 70 ^oC until about 20-25% of the initial volume remained. DI water was added to the flask to

compensate for the lost volume and the reaction mixture was stirred for several hours at room temperature.

The reaction mixture was then placed in a stainless steel autoclave equipped with PTFE liner (Parr Instruments) for hydrothermal treatment. ZSM-5 samples with different crystal sizes were synthesized at 150-165 ^{o}C for 48 to 96 hours under stirred conditions. Zeolite crystals were separated from supernatant via centrifugation at 14000 rpm (20817 x g) for 20 minutes. The solid material was triple washed with DI water and dried in an oven at 100 ^{o}C overnight. The ZSM-5 samples were calcined in air at 600 ^{o}C for 6 hours in order to remove template molecules from the pores.

4.3.2 Synthesis of Na-β

Zeolite Beta nanocrystals were synthesized from the reaction mixture with the following compositions: 25 TEOS: 1 $NaAlO_2$: 1300 H_2O: 20 TEAOH, where TEOS = tetraethylorthosilicate, and TEAOH = tetraethylammonim hydroxide.

First, the template (TEAOH) sodium aluminate and water were stirred in a RB-flask until all of the sodium aluminate was dissolved. Next, TEOS was added and the mixture was stirred overnight. The reaction mixture was rotary evaporated at 70 ^{o}C until about 20-25% of the initial volume remained. DI water was added to the flask to compensate for the lost volume and the reaction mixture was stirred for several hours at room temperature.

The reaction mixture was then placed in a stainless steel autoclave equipped with PTFE liner (Parr Instruments) for hydrothermal treatment. Zeolite-β samples with different crystal sizes were obtained after hydrothermal treatment at 130-140 ^{o}C for 48 to 96 hours under stirred or static conditions. Zeolite crystals were separated from supernatant via centrifugation at 14000 rpm (20817 x g) for 20 minutes. The solid material was triple washed with DI water and dried in an oven at 100 ^{o}C overnight.

Zeolite-β samples were calcined in air at 600 ^{o}C for 6 hours in order to remove template molecules from the pores.

4.3.3 Synthesis of NaY

NaY nanocrystals were synthesized from a clear gel solution of the following composition: 3.4 TEOS : 2 AIP : 4.9 TMAOH : 370 H_2O : 0.064 NaOH, where TEOS = tetraethylorthosilicate, AIP = aluminum isopropoxide and TMAOH = tetramethylammonium hydroxide. First, one half of TMAOH solution was mixed with AIP, water and sodium hydroxide and vigorously stirred for several hours at room temperature. The other half of TMAOH was mixed with TEOS and stirred in a separate flask under the same conditions. After AIP was completely dissolved, the two solutions were mixed together and stirred overnight. The zeolite NaY sample used in this study was synthesized from a recycled reaction mixture.[22] The recycled synthesis mixture was placed in a RB-flask and hydrothermally treated in an oil bath at 98 ^{o}C for 3 days. After completion of the synthesis, the NaY nanocrystals were separated from supernatant via centrifugation at 14000 rpm (20817 x g) for 20 minutes. The nanocrystals were subsequently washed and centrifuged twice with water and once with ethanol, and dried in an oven in air at 105 ^{o}C overnight. The zeolite was then calcined in oxygen at 550 ^{o}C for 12 hours in order to remove the organic template from the pores.

4.3.4 Ion Exchange of Nanocrystalline Zeolites

Ion exchange conditions are shown in Table 3. Typically, 500 mg of zeolite powder was placed in a RB flask and 50 mL of metal salt solution was added. The zeolite suspension was stirred during the ion exchange process. Metal containing samples were washed with DI water 4 times and dried in air at 100 ^{o}C overnight. Fe- containing samples were additionally calcined at 400 ^{o}C for 4 hours.

Table 3. Experimental conditions for ion-exchange of the zeolite samples.

Metal salt	Molar concentration	Temp. (°C)	Time (hrs)
$MnCl_2$	0.05M	80	4
$VOSO_4$	0.05M	70	4
$FeCl_2$	0.05M	70	5
$Ce(NO_3)_3$	0.05M	70	24
$Cu(NO_3)_2$	0.05M	70	4
$SnCl_2$	0.05M	70	5

For preparation of zeolites with bimetallic composition, aqueous solutions of respective metal salts with appropriate ratios were first prepared. The ion-exchange was then performed in the same fashion as in the case of single metal containing samples.

4.3.5 Characterization.

Crystallinity of zeolite samples was evaluated using powder X-ray diffraction (Siemens D5000 X-ray diffractometer with Cu Kα and nickel filter) in step mode with step size 0.04. Integrated intensities of selected reflections relative to those of commercially available zeolites were used to calculate % crystallinity of the samples. Reflections between 22.5 and 24.3 2θ were used for ZSM-5, the reflection at 22.5 2θ was used for Zeolite-β, and the reflection at 23.5 2θ was used for zeolite-Y.

50 point nitrogen adsorption / desorption isotherms were obtained (Nova 4200, Quantachrome) in order to characterize the surface areas and pore volumes of the metal-exchanged samples. The samples were outgassed overnight at 120 ^{o}C prior to the measurement. The total pore volume (V_{tot}) was calculated by measuring the amount of adsorbed nitrogen at 0.99 P/P_o. The t-plot method was used to calculate the micropore volume (V_{micro}). The mesopore volume (V_{meso}) was calculated from the difference between the V_{tot} and V_{micro}.

ICP spectroscopy (Varian 720-ES ICP-OES) was used to determine the respective metal concentration, Si/Al and M/Al ratios of the samples. Typically, 5 mg of the sample was digested in 1.6 mL 70:30 HCl : HF mixture. Then 0.56 mL of concentrated nitric acid and 8.4 mL of 5% boric acid were added and the volume was adjusted to 14mL with DI water. Three replicate solutions were prepared for each zeolite sample and the resulting measured concentrations were averaged. 1 ppm solution of yttrium was used as an internal standard during the measurements.

For TEM imaging (JEOL JEM-1230 Transmission Electron Microscope), a drop of dilute sample suspension in methanol was placed on a carbon coated copper grid (Grid

Tech) and dried at room temperature prior to the measurement. The images were recorded at the accelerating voltage of 120 kV.

4.4. Results and Discussion

4.4.1 Zeolite Synthesis, Characterization, and Ion Exchange

Summaries of the zeolite samples synthesized and the textural properties is provided in Table 4 and 5. Representative powder XRD patterns of parent zeolites are shown in Figure 35. The peak positions observed in each of the XRD patterns of the parent zeolites match those of standard β, ZSM-5 and Y samples.

The metal exchanged ZSM-5, β, and NaY zeolites were studied using scanning and transmission electron microscopy in order to provide information about the size of the zeolite crystals and their the aggregates (Figure 36 and Figure 37). SEM images of representative parent zeolites are shown in Figure 36. The size of crystals or crystal aggregates ranged from ~30 to ~500 nm, whereas commercial zeolites typically have crystal sizes of several micrometers. However, the size of the crystals located within the aggregates is difficult to obtain using SEM.

Transmission electron microscopy images reveal more information about the composition of the zeolite crystal aggregates and the size of individual crystals (Figure 37). ZSM-5 samples Z1 and Z2 with smaller S_{ext} values consist of crystals 34 and 41 nm size respectively as well as aggregates of crystals with size ranging between 200 and 300 nm. The ZSM-5 zeolite sample Z3 is composed of nanocrystals aggregates, which size ranges from 200 to 500 nm. The size of nanocrystals in the sample is under 10 nm.

TEM images of zeolite β samples B1 and B2 with smaller external surface area show extensive aggregation of crystals, which size is over 200 nm and in some cases reach 500-600 nm. Increasing the external surface area to 71 m^2/g in the case of Sample B3 resulted in a significant decrease of the particle size to approximately 80 nm. TEM images of Naβ zeolite B4 show particles of about 100 nm that appear to be aggregates of

Table 4. Summary of single component metal ion-exchanged zeolite samples.

Sample	S_{ext}, m^2/g	$S_{tot,}$ m^2/g	Ssize, nm	Si/Al	M/Al	M conc. (wt. %)	RC, %	TEM size, nm
Zeolite-β B1 (parent)	42	398	229	36	-	-	126	204 (34) aggregates
Mn				29	0.76	2.38		
V				34	0.55	1.44		
Fe				44	10.5	22.5		
Zeolite-β B2 (parent)	43	387	235	72	-	-	33	254 (112) 576 (48) aggregates
Mn				71	0.54	0.70		
V				88	0.88	0.85		
Fe				120	32.3	25.0		
ZSM-5 Z1 (parent)	66	369	65	27	-	-	72	34(14) crystals 222(48) aggregates
Mn				28	0.30	0.98		
V				34	0.98	2.47		
Fe				34	7.65	20.9		
Zeolite-β B3 (parent)	71	542	55	18	-	-	41	80 (20) aggregates
Ce				17	0.202	0.53		
Cu				19	1.42	3.54		
Sn				38	10.6	12.8		
ZSM-5 Z2 (parent)	38	352	82	28	-	-	96	41(15) crystals 255(23) aggregates
Ce				33	0.06	0.08		
Cu				28	1.33	2.20		
Sn				26	5.83	10.5		
NaY (parent)	103	470	74	1.76	-	-	-	37 nm crystals
Mn				1.63	0.04	1.24		
V				1.65	0.21	6.52		
Ce				1.60	0.15	12.16		

Table 5 . Multi-component Ion Exchanged Zeolite Samples.

Sample name	Metals	Sext, m^2/g (parent)	S_{total}, m^2/g (parent)	M/M molar ratio	Metal wt. %	TEM average particle size, nm
ZSM-5 B3-Ce/V	Ce/V	145	379	0.14	Ce = 0.62 V = 1.90	10 nm crystals 200-500 nm aggregates
ZSM-5 B3-Ce/Mn	Ce/Mn			0.71	Ce = 1.15 Mn = 0.53	
ZSM-5 B3-Mn/V	Mn/V			1.45	Mn = 0.23 V = 0.15	
Naβ B4-Ce/V	Ce/V	126	581	0.80	Ce = 1.92 V = 0.69	101 (21) nm aggregates
Naβ B4-Ce/Mn	Ce/Mn			0.46	Ce = 1.22 Mn = 1.10	
Naβ B4-Mn/V-1	Mn/V			0.91	Mn = 0.56 V = 0.57	
Naβ B4-Mn/V-2				1.64	Mn = 0.79 V = 0.45	
Naβ B4-Mn/V-3				3.14	Mn = 0.88 V = 0.26	
NaY B1-Mn/V	Mn/V	103	470	1.21	Mn = 2.99 V = 2.32	37 nm crystals
NaY B1-Ce/V	Ce/V			1.00	Ce = 8.96 V = 3.24	

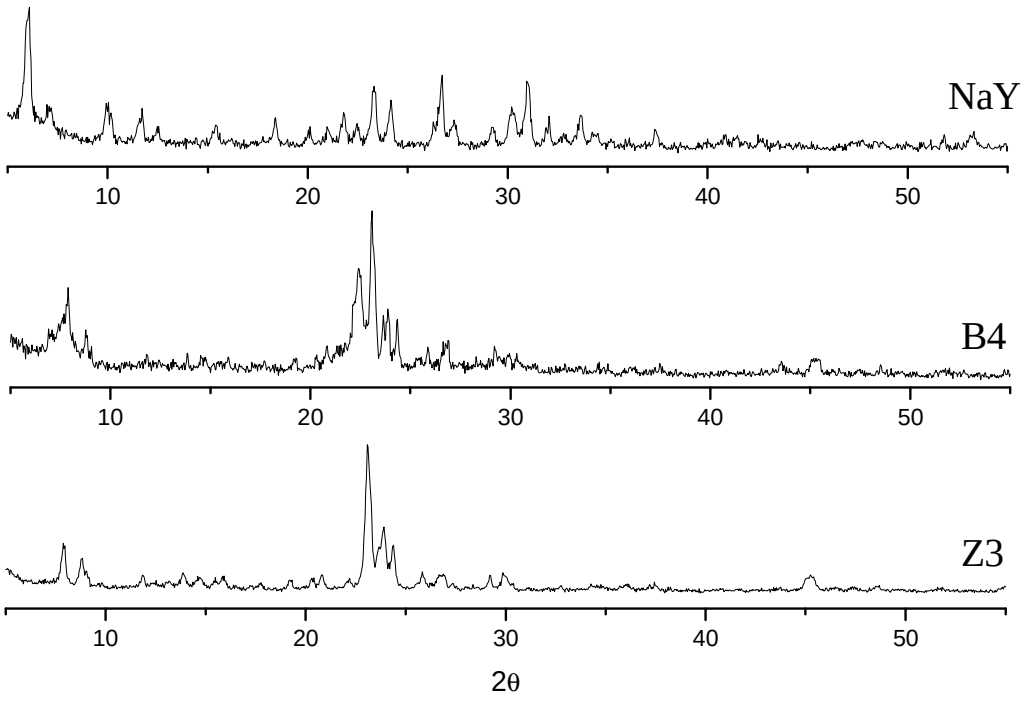

Figure 35. Powder XRD patterns of calcined parent Zeolite-β B4, ZSM-5 Z3, and NaY samples.

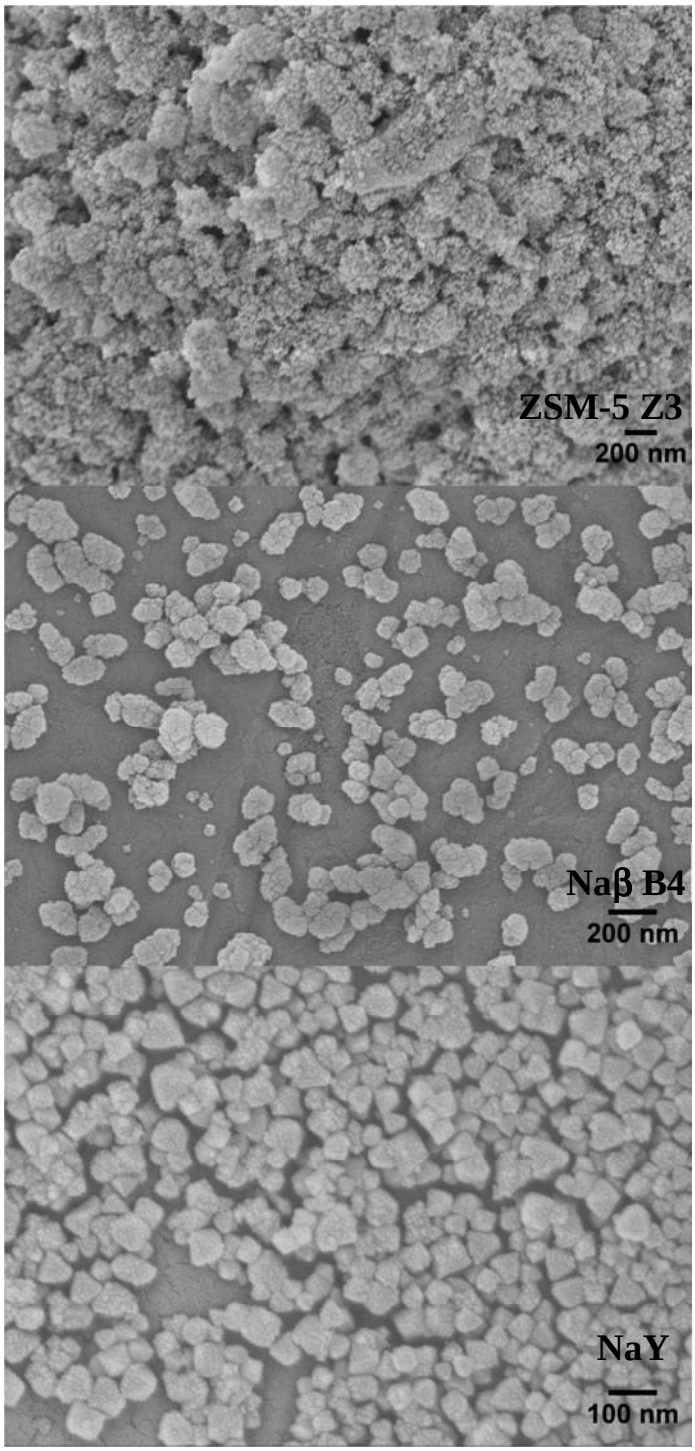

Figure 36. Representative SEM images of parent NaZSM sample Z3; Naβ sample B4, and NaY zeolite samples.

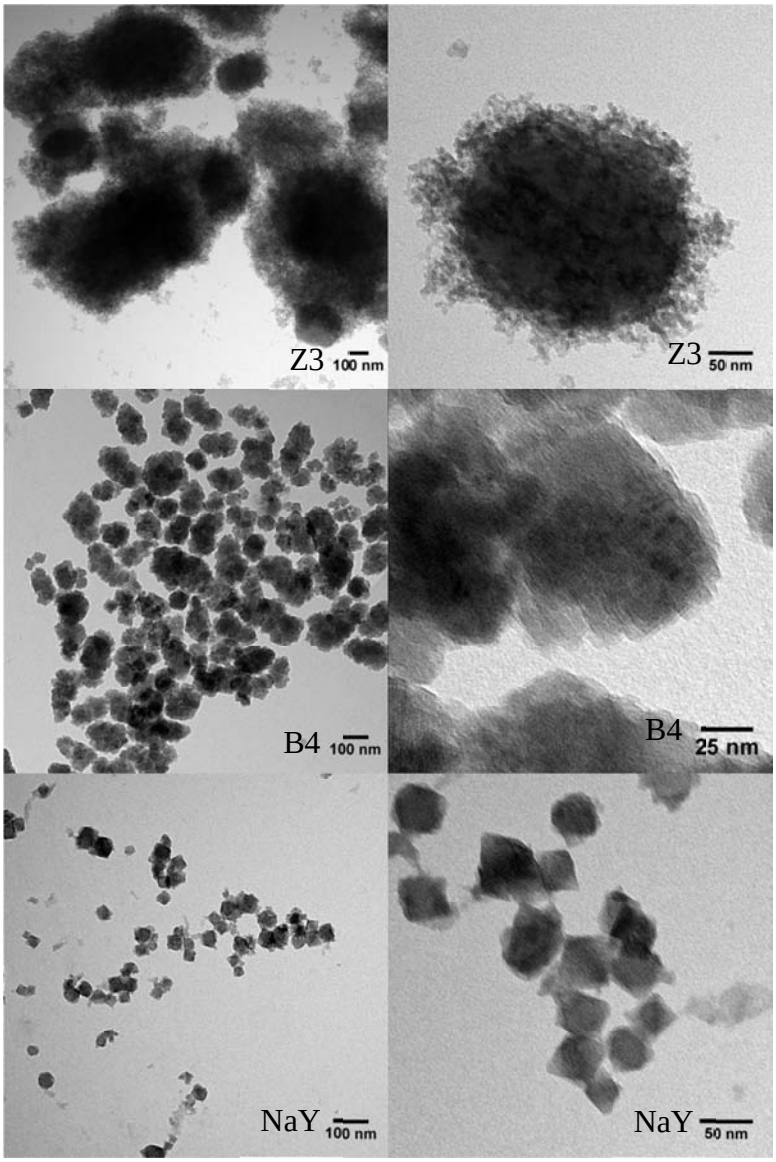

Figure 37. Representative TEM images of ion-exchanged ZSM-5 sample Z3, Naβ sample B4, and NaY samples.

smaller crystals. The crystals are more tightly packed in the aggregates than in the case of ZSM-5 samples and their size appears to be under 20 nm.

Morphology of NaY zeolite used for the ion-exchange significantly differs from that of Naβ and ZSM-5 samples. The TEM images reveal zeolite crystals of ~ 37 nm in size that are well resolved do not appear to be aggregated. The lattice fringes can be clearly seen in the most of the crystals suggesting that that the ion-exchange procedure did not have any effect on the sample framework.

4.4.2 Nitrogen Adsorption Isotherms.

External surface area of commercially available zeolites is small due the micrometer size of their crystals, and is typically below 10 m^2/g. The S_{ext} values of the nanocrystalline zeolite samples are significantly higher than for the commercial zeolites. The ZSM-5 and Naβ zeolite samples ion-exchanged with a single transition metal have S_{ext} values ranging from 40 to 70 m^2/g (Table 5). The ZSM-5 and Naβ zeolites exchanged with two metal ions as well as single and double metal exchanged NaY zeolites used in this study are 145 m^2/g, 126 m^2/g and 103 m^2/g respectively. The S_{ext} represents a significant fraction of the total surface area in the samples, approximately 20-25% in the case of NaY and Naβ zeolites, and 41% in the case of ZSM-5 zeolite. Large external surface area values of the samples mean that a larger fraction of catalytic sites is located on the easily accessible surface in comparison with conventional micron sized crystals. Total specific surface areas (S_{sp}) listed in Table 2 for the zeolite samples are comparable to those of commercial zeolites (396 m^2/g for Zeolyst Na-ZSM-5, 429 m^2/g for Zeolyst Na-β, 640 m^2/g for Zeolyst NaY).

Nitrogen adsorption / desorption isotherms were collected for select ion-exchanged samples and compared with their respective parent zeolites to evaluate effect of metal-exchange on their surface area and pore volume characteristics (Figure 38). Ion-exchanging the zeolites with metals ions resulted in a slight decrease of the total surface

Table 6. Surface area and pore volume analysis of representative zeolite samples.

Sample name	$S_{ext,}$ m^2/g	$S_{total,}$ m^2/g	$S_{micro,}$ m^2/g	$V_{total,}$ cc/g	$V_{micro,}$ cc/g	$V_{meso,}$ cc/g
ZSM-5 Z3 parent	145	371	226	0.625	0.092	0.533
ZSM-5 Z3 Mn/V		349	204	0.636	0.085	0.551
Nab B4 parent	126	521	395	0.622	0.175	0.447
Nab B4 Mn/V-1		502	376	0.670	0.168	0.502
NaY parent	103	462	359	0.437	0.164	0.273
NaY Mn		432	329	0.401	0.161	0.240

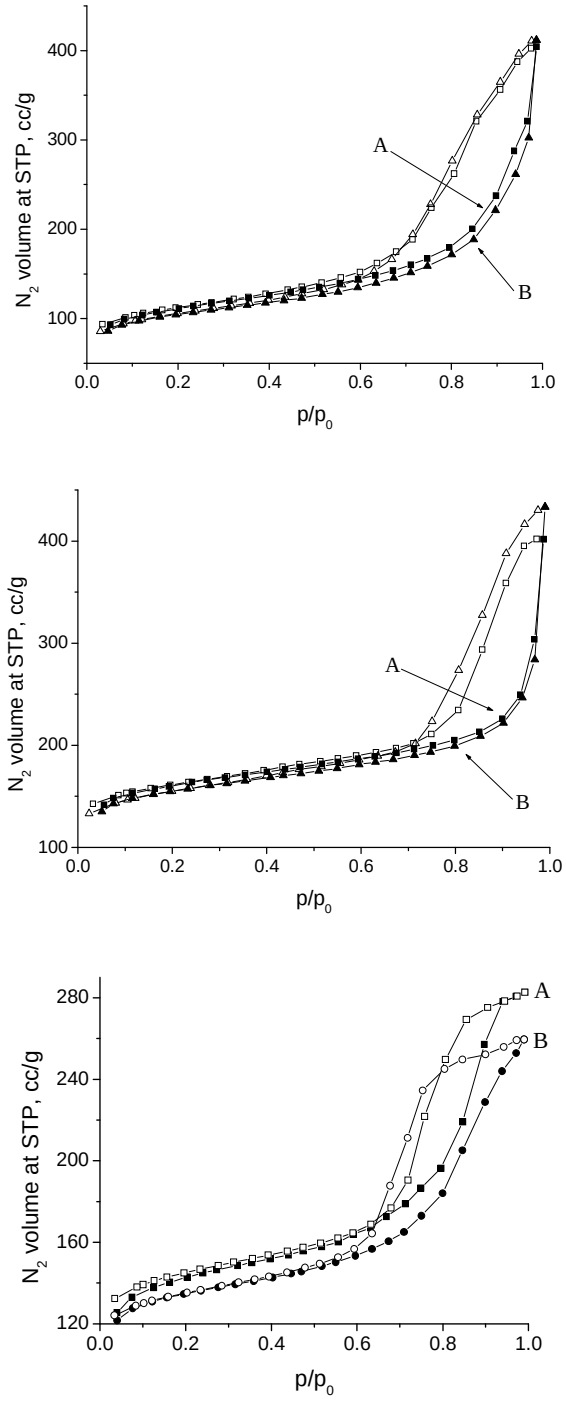

Figure 38. Nitrogen sorption isotherms of ZSM-5 sample Z3, Naβ sample B4, and NaY zeolite. Parent zeolite sorption isotherm is labeled as (A) and the ion-exchanged as (B). Filled and open symbols represent adsorption and desorption data points respectively.

area. The S_{tot} decreased from 379 m^2/g to 349 m^2/g in the case of ZSM-5-Mn/V, from 581 m^2/g to 502 m^2/g in the case of Naβ-Mn/V-1, and from 470 m^2/g to 432 m^2/g for NaY-Mn/V samples, which translates into approximately 10% decrease of the S_{tot} after the ion-exchange (Table 6).

The parent and metal-exchanged ZSM-5 and Naβ samples have large mesopore volumes. High external surface areas and large mesopore volumes of the ZSM-5 and Naβ samples as well as their TEM images indicate that these zeolite samples consist of nanocrystals that form mesoporous aggregates. The aggregates are stable even after prolonged sonication, which was performed prior to collection of TEM images and did not result in the breakage of the aggregates. The mesopore volume of the NaY zeolite, both parent and ion-exchanged, is lower than for the other two zeolite samples. The mesopore volume determined for the sample is most probably due to the presence of intercrystalline voids between the crystals in the powder, as the TEM images suggest that there is no significant aggregation of the crystals. Ion-exchange with metal ions did not have a significant effect on the pore volumes of the zeolite samples. The total pore volume of NaY and zeolite decreased slightly after the ion-exchange, while the total pore volume of Naβ and ZSM-5 slightly increased. In all three of the zeolite samples, the micropore volume decreased slightly after the ion-exchange.

In summary, the nitrogen sorption isotherm analysis has shown that the ion-exchange process does not have any marked effect on the surface area and pore volume of the zeolite samples. Such behavior is expected, as the metal loadings in the zeolite samples are fairly low. Incorporation of metal ions occurs through substitution of existing sodium cations at the ion-exchange sites, and proceeds without significant occlusion of pore network. The small difference between parent and ion-exchanged samples also indicates that the zeolite samples retain their stability during the ion-exchange process.

4.4.3 ICP-OES spectroscopy

The ICP-OES analysis was carried out to quantify the amount of metals in the zeolite and the ratio between metals in case of co-exchanged samples as well as the silicon to aluminum ratio. The results are listed in Table 5 and Table 4. The metal-to-metal ratio in the zeolite can be controlled by changing the ratio between respective metals in the ion-exchange solutions. ZSM-5 and Naβ zeolites have comparable metal loadings, while NaY samples in general have higher metal weight percentage. Higher metal loading in case of NaY samples is due to higher aluminum content and, therefore, larger amount of ion-exchange sites.

Si/Al ratio in ZSM-5 samples remains the same or slightly increases after ion-exchange due to some dealumination. Si/Al ratio in zeolite-β samples shows similar behavior to ZSM-5 in the cases of VO^{2+}, Mn^{2+}, Cu^{2+} and Ce^{3+} ions. However, there is a dramatic increase of Si/Al ratio in case of Fe^{2+} and Sn^{2+} ion-exchanged samples that suggests higher dealumination of these samples relative to the other samples. It appears that the high metal loadings lead to increased dealumination.

Studies of metal concentration in the zeolites have shown different binding activity of metal ions to the anionic sites in the zeolite. Metals used in this work fall into three categories. Cerium (III) has the lowest concentration in both beta and ZSM-5 samples (0.2 and 0.06 wt. % respectively). Manganese (II), vanadyl (VO^{2+}) and copper (II) constitute the group of metals with average ion-exchange activity and their concentration in the zeolite samples ranges from 0.3 to 1.42 wt. %. Finally, iron(II) and tin(II) have the highest concentration in zeolite, reaching up to 25 wt. % in case of iron and 12.8 wt. % in case of tin. High amounts of tin and iron in the zeolite samples is most probably due to formation of respective hydroxides during ion exchanging. These hydroxides are insoluble in water and therefore are not removed during the washings and remain deposited in the zeolite.

In the case of zeolites co-exchanged with two metal cations the difference in metal binding activity resulted in a difference between the metal-to-metal ration in the solutions and the solids. Among three metals used for sample preparation, cerium cation showed a lower uptake in the case of ZSM-5 and Naβ zeolites. Conversely, cerium binding to NaY zeolite was noticeably higher than that of vanadium and manganese. This is in agreement with the study by Keane, who observed a higher selectivity towards cerium exchange in comparison with divalent metal exchange, such as nickel and copper, in zeolite Y. The author concluded that this selectivity may be due to more efficient compensation of framework charge by trivalent cations in zeolite Y.[141] Therefore, a careful choice of metal-to-metal ratio in the ion-exchange solutions was required in order to obtain the desired bi-metal composition in the zeolite samples.

4.5 Conclusions

In conclusion, series of single- and double- metal exchanged ZSM-5, β and Y zeolites were successfully prepared. In the case of manganese and vanadium exchanged ZSM-5 zeolite, the ratio between the two metals was systematically varied. Nitrogen adsorption study has shown the absence of significant changes of surface area and pore volume after the ion-exchange. Transmission and scanning electron microscopy have not revealed any changes of the particle morphology. The concurrent ion-exchange of zeolites with two transition metal ions was found to be a complex process. The ratio between the metals in the zeolite material is different from their ratio in the ion-exchange solution and depends on the affinity of metal cations to the surface exchange sites of specific zeolites. The metal-containing zeolite materials were tested for deNOx activity under relevant conditions at Honda Research Institute.

CHAPTER 5.
EFFECT OF CRYSTAL SIZE AND SURFACE FUNCTIONALIZATION ON THE CYTOTOXICITY OF SILICALITE-1 NANOCRYSTALS

5.1 Abstract.

In this chapter, the synthesis and characterization of nanocrystalline silicalite (the purely siliceous form of the zeolite, ZSM-5) of defined crystal size and surface functionalization is described, and the effect on the type and degree of cytotoxicity induced in two distinct model cell lines is determined. The silicalite materials were characterized by powder X-ray diffraction, dynamic light scattering and ζ-potential, solid state NMR, thermal gravimetric analysis, and nitrogen adsorption using the BET method to determine specific surface area. The silicalite samples were functionalized with amino, thiol, and carboxy groups and had crystal sizes of approximately 30, 150, and 500 nm. The cytotoxicities of the silicalite samples with different crystal sizes and different surface functional groups were investigated using human embryonic kidney 293 (HEK-293) cells and RAW264.7 macrophage cell lines. We used the lactic dehydrogenase release assay to measure damage to the cell membrane, the caspase 3/7 activity assay to measure key molecules involved in apoptosis, and the Annexin V-propidium iodide staining method to provide visual confirmation of the types of cell death induced. We have shown that the impact of size and surface functionalization of silicalite nanoparticles on cell toxicity and mechanism of cell death is cell type dependent. Thirty nanometer silicalite nanoparticles were nontoxic in RAW264.7 cells relative to untreated controls but caused necrosis in HEK293 cells. Carboxy-functionalized 500 nm silicalite nanoparticles resulted in apoptosis and necrosis in RAW264.7 cells and predominantly activated apoptosis in HEK293 cells.

5.2 Introduction.

The rapid growth and development in the synthesis of nanomaterials with carefully controlled properties, such as size and shape, surface area, and composition, has led to a burgeoning of potential applications for nanomaterials, in areas such as electronics, catalysis, optics, and medicine. Carbon-based nanomaterials (carbon nanotubes and buckyballs), semiconductor quantum dots (CdSe), metal nanoparticles and nanorods (gold, nickel, and platinum), and nanosized metal oxides (TiO_2) are important nanomaterials that have been widely studied. For example, metal nanoparticles and nanorods (gold nickel and platinum) are being intensely investigated for applications in cancer detection,[142, 143] imaging,[142] and gene delivery.[144-146] Porous nanomaterials,[18, 101, 147-149] such as zeolites and mesoporous silica, have emerged as nanomaterials with new properties and many potential applications, in areas such as environmental catalysis,[140] drug delivery,[150, 151] and imaging.[152-156]

The growing interest in nanomaterials and their potential applications in these important areas obviate the need to study the toxicity of nanomaterials prior to their widespread use in these far-reaching applications. The smaller size scale of nanoparticles may increase their toxicity or change the mechanism by which they induce toxicity. Toxicological data to date on “incidental” nanoparticles that are produced as a byproduct cannot necessarily be extrapolated to engineered nanoparticles because they do not have the same size, composition, and surface properties.[157] Studies of the toxicity of nanomaterials are further complicated by the fact that nanomaterials have size and shape-dependent properties and are routinely prepared with specific surface coatings.

Zeolites are important commercial materials that are widely used in applications such as catalysis,[158, 159] separations,[160] water softening,[160] and as bloodclotting[161] and imaging agents.[154, 155, 162-164] Zeolites are porous, crystalline materials that have very large surface areas due to the internal surface area of the pores. Mesoporous silica is a related porous material that is amorphous and has larger pores than zeolites. Mesoporous silica

has pores of >2 nm as compared to zeolite micropores of <2 nm. Mesoporous silica can be readily functionalized for applications in catalysis,[165] imaging,[156, 166, 167] and drug delivery.[151, 168] Nanoscale zeolites are zeolites with crystal sizes of less than 100 nm, which have large surface areas due to appreciable internal and external surface areas.[22, 169] The external surface area of nanoscale zeolites is up to an order of magnitude larger than the external surface area for micrometer sized zeolites and provides an additional surface for reaction or functionalization.[169-171] Functionalization of the external surface of nanoscale zeolites has been shown to be critical for applications in biomedicine, such as imaging[172] and drug delivery,[150] and in the development of low dielectric materials for the semiconductor industry.[173] Because of their numerous commercial applications, toxicity studies of zeolites[174] and crystalline silicas,[175-181] such as quartz, have been reported in the literature. While studies of the natural zeolite, clinoptilolite, indicated that it is nontoxic and safe for human and veterinary use,[149, 182] other studies have shown that crystalline silica materials may exhibit toxicity through silicosis, which is caused by inhalation of crystalline silica particles of respirable size. Extensive studies of crystalline silica materials such as quartz dusts have shown that physicochemical properties, such as particle size, shape, surface area, and surface chemistry, all impact toxicity. For example, in a study by Fubini and co-workers, the cytotoxicity of artificial crystalline silicas (differing size, morphology, and surface area) to macrophages was investigated.[174] Macrophages were chosen because alveolar macrophages play a key role in silica related diseases by clearing particles out of the lung or by causing chronic inflammation. Similar toxicity was observed for calcined versus uncalcined crystalline silicas, suggesting that the internal surface does not play a significant role in silica toxicity for these materials. The deposition of aluminum on the zeolite external surface was found to decrease toxicity.[174]

Mesoporous silica, such as MCM-41, which in comparison to zeolites is amorphous, is being intensively investigated for biomedical applications.[156, 183, 184] There

have been several studies recently focused on the interaction of mesoporous silica materials with cells.[185-188] Lin and co-workers investigated the effect of surface functionalization of MCM-41 on cellular uptake.[188] Their study showed that the cellular uptake varied with surface functionality in that the ED_{50} increased with decreasing ζ-potential. In a recent study by Asefa and coworkers, the toxicity of MCM-41 and functionalized MCM-41 showed that unfunctionalized MCM-41 was more toxic on a per particle basis toward human neuroblastoma (SK-N-SH) than aminopropyl- and mercaptopropyl-functionalized MCM-41 and that the most toxic mesoporous silica materials studied were those with the largest BET surface areas.[186] Huang and coworkers determined that positively charged MCM-41 enhanced cellular uptake and that increased surface charge did not increase cytotoxicity.[185] Another recent study suggested that mesoporous silica inhibited cellular respiration.[187]

The focus of the work reported here is the cytoxicity of silicalite with varying size and surface functionalization. In this study, silicalite-1, which has the MFI structure and is the purely siliceous form of the zeolite, ZSM-5, was synthesized with three different crystal sizes (~30, 150, and 500 nm).[22, 189] The silicalite external surface was functionalized by grafting of aminopropyl, mercaptopropyl, and carboxy functional groups onto the external zeolite surface as shown schematically in Figure 39. These functional groups were chosen so that the effect of surface charge on cytotoxicity could be systematically investigated. The silicalite materials were extensively characterized by powder X-ray diffraction (XRD), dynamic light scattering and ζ-potential, solid state NMR, thermal gravimetric analysis (TGA), and nitrogen adsorption using the BET method to determine the specific surface area. The importance of careful characterization of nanomaterials for toxicity studies has been noted in the literature.[157, 190-193] The cytotoxicity of the silicalite samples with different crystal sizes and different surface functional groups was investigated using human embryonic kidney 293 (HEK-293) cells and the RAW264.7 macrophage cell lines. The rationale behind this selection of cell

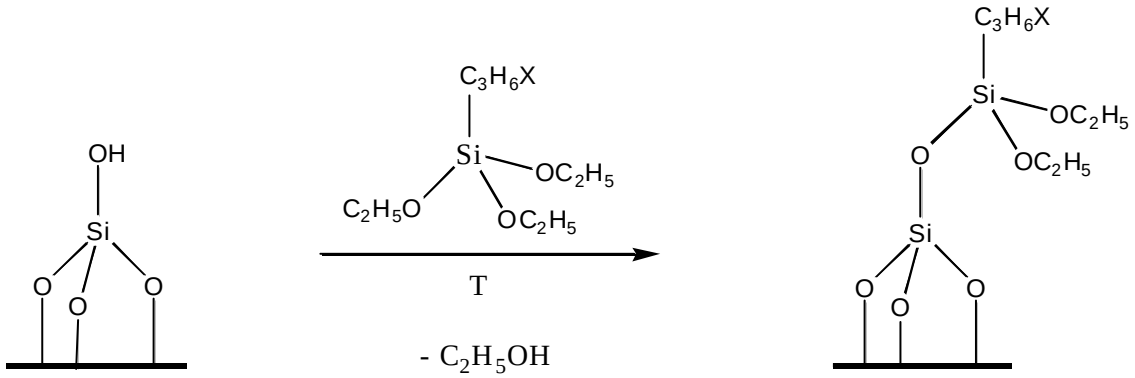

where X = NH_2, SH or CN

Figure 39. Reaction scheme depicting the reaction of the surface silanol groups with the organosilanes (APTES, MPTS, and CPTS) to form amino, thiol and cyano functionalized silicalite-1. The cyano functionalized silicalite-1 was treated with sulfuric acid to form carboxy functionalizaed silicalite-1.

models is that the RAW264.7 cell line is a model macrophage cell line commonly used to represent the physiological scavengers of foreign nanoparticles. HEK293 cells were selected for evaluation in cytotoxicity studies because of their relevance and wide utility in the development of drug and gene delivery vehicles. Cells can die by either of two major mechanisms: necrosis or apoptosis.[194] Necrosis is the death of the cells through external damage, usually mediated via destruction of the plasma membrane or the biochemical supports of its integrity. Necrosis can occur in a matter of seconds. The other major form of cell death, apoptosis, is based on the concept of programmed cell death. Apoptosis is a much slower series of events than necrosis, requiring from a few hours to several days, depending on the initiator. The manifestations of apoptosis, both biochemical and morphological, are unique and are completely different from those of necrosis.[195] In this study, we used the lactic dehydrogenase release (LDH) assay to measure damage to the cell membrane, the caspase 3/7 activity assay to measure key molecules involved in apoptosis, and the Annexin V-propidium iodide (PI) staining method to provide visual confirmation of the types of cell death induced relative to the size and surface functionalization of the silicalite nanoparticles.

5.3 Experimental Procedures

5.3.1 Silicalite-1 Preparation.

Silicalite-1 was synthesized according to a well-established procedure.[189] Three batches of reaction mixture with the molar ratio of components TEOS:TPAOH: NaOH:H_2O as 25:9:0.16:495 were prepared. One batch was heated at 60 ^oC in an oil bath for 9 days, while the other two were heated at 165 ^oC in stainless steel autoclaves equipped with a PTFE liner for 46 and 56 h. The resultant suspensions were centrifuged at 14000 rpm (20817 x g) for 20 min to separate the particles from the supernatant. The particles were then washed once with ethanol and twice with deionized water and dried at 90 ^oC overnight. All samples were calcined in air at 600 °C for 6 h to remove the organic

template. Samples are labeled according to their crystal size estimated from BET. For example, 31 nm silicalite-1 will be referred to as silicalite- 31.

5.3.2 Functionalization of Calcined Silicalite.

Functionalization with amine groups was carried out by refluxing a mixture of 2 g of silicalite and 2 g of 3-aminopropyltriethoxysilane (APTES) in 60 mL of toluene for 4 h followed by centrifugation and washing of the silicalite powder with toluene. Functionalization with thiol groups was carried out by refluxing a mixture of 2 g of silicalite and 4 g of 3-mercaptopropyltriethoxysilane (MPTS) in 60 mL of toluene for 4 h followed by centrifugation and washing of the silicalite powder with toluene.

Functionalization with carboxypropyl groups was done in two steps. First, 2 g of silicalite was refluxed with 4 g of (3-ethoxysilyl)propionitrile (CPTS) in 60 mL of mesithylene overnight. The suspension was then centrifuged, and the crystals were washed with acetone. CPTS-functionalized silicalite was dried at 60 °C overnight. Then, the dry powder was suspended in 40 mL of 50% w/w sulfuric acid and refluxed for 6 h. The suspension was centrifuged, and the particles were washed with deionized water until the pH of the supernatant became neutral. Functionalized samples were dried in an oven at 60 °C overnight. Samples are labeled according to the functionalization and size. For example, 31 nm silicalite-1 that has been functionalized with APTES will be referred to as APTES-silicalite-31.

5.3.3 XRD and Nitrogen Adsorption.

Both calcined and functionalized silicalite nanocrystals were characterized using powder XRD (Siemens D5000 X-ray diffractometer with Cu Kα and nickel filter). The nitrogen adsorption isotherm (Nova 1200, Quantachrome) was measured to calculate specific surface area and particle size (in the case of as-synthesized crystals) for each sample. The specific surface obtained using the BET method on the as-synthesized samples, in which the template is still present in the pores, provides the external surface

area, S_{ext}. As described previously in the literature,[27] the BET external surface area can be used to calculate the silicalite crystal size assuming uniform cubic crystals by using the following equation:

$$x = \frac{3214}{S_{ext}} \qquad (14)$$

where S_{ext} is the external surface area in m^2/g and x is the silicalite-1 crystal size in nm. The total specific surface area is obtained using the BET method on the calcined silicalite samples.

5.3.4 Scanning Electron Microscopy (SEM).

SEM images of the silicalite crystals were acquired using a Hitachi S-4800 scanning electron microscope. To prepare the sample for SEM, a drop of dilute colloidal solution of the sample in methanol was dropped onto the SEM sample stud surface, and the sample stud was then dried for 15 min at room temperature. Shortly before acquiring an SEM image, the sample was coated with gold.

5.3.5 ζ-Potential Measurements.

The samples were prepared in the following way: 4 mg of sample was placed in disposable plastic tubes. Four milliliters of acetate (pH 4-6) and phosphate buffer (pH 6.2-8) solutions with matching ionic strengths was added to the silicalite powder, and the resulting suspensions were sonicated for 1 h (1510 Sonicator, Branson). The suspensions were allowed to settle overnight, and their pH (Corning pH meter 320) was checked prior to the ζ-potential measurements (Zetasizer Nano-ZS, Malvern Instruments).

5.3.6 EPR study of ROS generation.

Generation of reactive oxygen species by the zeolite surface was studied by EPR following the procedure previously described.[196] 5,5-dimethyl-1-pyrroline-N-oxide (DMPO) was used as a spin trapping agent. 50 μl of distilled deionized water, 50 μl of 0.5 M H_2O_2 in pH = 7.4 phosphate buffer and 100 μl of 0.05 M of DMPO in distilled deionized water were added to 4-6 mg of fine zeolite powder. The solution was separated from zeolite via centrifugation (2 minutes at 14000 rpm (20817 x g)) and loaded into a flat cell. CW EPR (continuous wave EPR) spectra were acquired using a Bruker EMX61 EPR spectrometer equipped with a PC for spectrometer control and data acquisition. A flat cell was used for acquisition of the EPR spectra. Typical EPR spectral parameters were: X-band frequency = 9.43 GHz, modulation amplitude = 0.5 G and modulation frequency = 100 kHz. The magnetic field and microwave frequency were measured using a Hall probe and a frequency counter, respectively.

5.3.7 Cell Culture.

Human embryonic kidney 293 cells (HEK293) and macrophage cells (RAW264.7) were obtained from the American Type Culture Collection (Rockville, MD). The cells were maintained in Dulbecco's modified Eagle's medium (DMEM, Gibco) supplemented with 10% fetal bovine serum (Gibco), streptomycin at 100 μg/mL, penicillin at 100 U/mL, and 4 mM L-glutamine at 37 °C in a humidified 5% CO_2-containing atmosphere.

5.3.8 LDH Release Assay.

The LDH activity from the incubation medium of cultured cells was assayed using the CytoTox 96 nonradioactive cytotoxicity assay kit from Promega Corp. (Madison, WI). HEK293 and RAW264.7 cells were seeded in V-bottom 96 cells/well at 1 × 104 and 1.5 × 104, respectively. Cells were treated with silicalite nanoparticles using a series of concentrations for 4 h at 37 °C. Fifty microliters of incubation medium was

transferred into 96 well plates, mixed with 50 μL of reaction substrate mix, and incubated at room temperature for 30 min with light protection. Fifty microliters of stop solution was added into each well, and the optical density was measured at 490 nm using Spectramax plus384 Microplate Spectrophotometer (Molecular Device). Results were then normalized to untreated cells.

5.3.9 Caspase 3/7 Activity Assay.

HEK293 and RAW264.7 cells were seeded in 75 cm^2 flasks in DMEM growth media at 37 °C with 5% CO_2 and allowed to reach 75-80% confluence. One × 104 cells for HEK293 and 1.5 × 104 RAW264.7 cells/well were plated in 100 μL volume per well in 96 well plates for 24 h. To measure caspase 3/7 activity, the Apo-ONEHomogenous Caspase-3/7 assay kit from Promega Corp. was used according to the manufacturer's protocol. Briefly, cells were incubated with silica nanoparticles at a concentration of 1 mg/mL for 4 h. After 4 h, 100 μL of reaction mixture (substrate in lysis buffer) was added and the fluorescence measured at 2 h using 485 (excitation) and 527 nm (emission) wavelengths (Spectra Max M5, Molecular Device). Untreated cells were used as negative controls, and cells treated with 1 μM staurosporine for 2 h were used as positive controls.

5.3.10 Annexin V-PI Staining.

The Annexin V-PI staining method is commonly used to differentiate necrotic and apoptotic cells. For simultaneous detection of apoptotic and necrotic cell death, a costaining technique with fluorochrome-conjugated Annexin V, in tandem with the DNA-binding dye PI (Vybrant Apoptosis Kit #3, Molecular Probes) was used according to the manufacturer's instructions. Briefly, HEK293 and RAW264.7 cells were seeded in Lab-Tek II eight well chamber slides (Nalgene Nun Int., IL) at 2 × 105 cells/chamber using the same conditions as previous sets of experiments. Cells were incubated with different silicalite nanoparticles at 1 mg/mL for 4 h. After 4 h, the cells were washed in cold PBS. Cells were stained with Annexin V conjugate and PI. The images were taken

using a Zeiss 510 NLO confocal laser scanning microscope (Carl Zeiss Microscope Systems, Jena, Germany). Staining with Annexin-V identified apoptotic cells. Cells only stained with PI were identified as necrotic cells.

5.3.11 Statistical Analysis.

The data are presented as means (standard errors). The statistical significance was determined using one-way analysis of variance (ANOVA) and the Tukey post-test, where $P< 0.05$ was considered significant. The data presented are representative of at least three repeats.

5.4 Results

Silicalite was synthesized in three different crystal sizes (approximately 30, 150, and 500 nm), and the samples were subsequently functionalized with amine (APTES), thiol (MPTS), and carboxylate (CPTS) functional groups as shown schematically in Figure 39. The silicalite crystal structure was confirmed by powder XRD. Representative X-ray powder patterns of the calcined and APTES-functionalized silicalite-31 samples (Figure 40) reflect the MFI crystal structure and are very similar before and after functionalization, which indicates that the crystallinity of silicalite nanoparticles is retained during the surface functionalization. One exception was observed for the case of carboxyfunctionalized silicalite with the smallest crystal size of 31 nm. To form carboxy-functionalized silicalite, the silicalite is first treated with CPTS to form the CPTS-silicalite followed by treatment with sulfuric acid to convert the cyano group to a carboxy group. However, for silicalite-31, after the sample was refluxed in sulfuric acid, a brown powder was recovered and the XRD pattern of the brown powder did not contain any

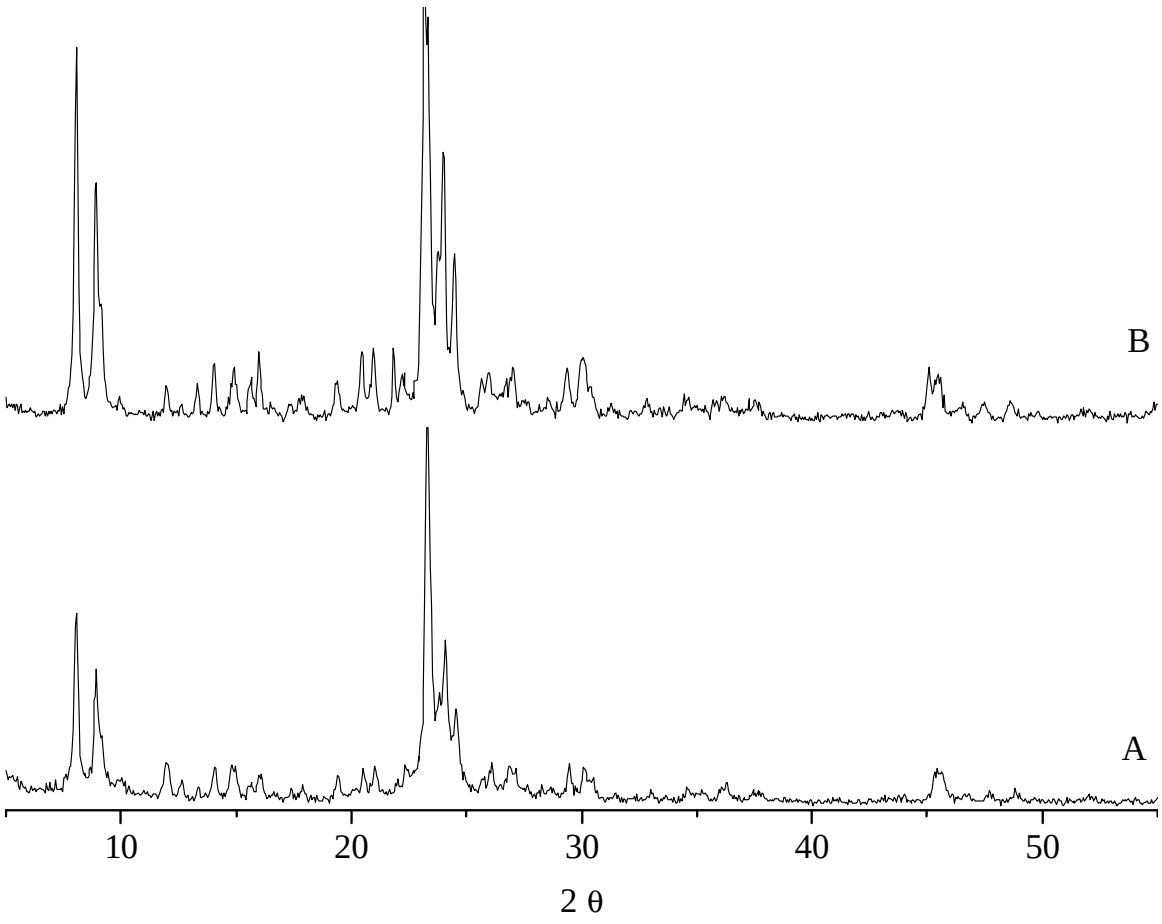

Figure 40. Representative powder XRD patterns of A) calcined silicalite-31 and B) APTES-silicalite-31.

characteristic silicalite reflections, which indicated the loss of crystallinity for this sample. When carboxy functionalization was carried out on 50 nm and larger silicalite particles, no loss of silicalite crystallinity was observed. It was concluded that the small size and high specific surface area, and therefore high surface free energy, potentially lead to instability of the smallest silicalite particles when they were refluxed in sulfuric acid.

Representative SEM images are shown in Figure 41 for (a) calcined silicalite-153 nm, (b) CPTS-silicalite-153, and (c) APTES-silicalite-153. The crystal morphology from the SEM images is approximately cubic and did not noticeably change when the sample was functionalized. The crystal size from SEM agrees with the crystal size obtained from the BET surface area as described below.

The BET specific surface area (S_{sp}) of the silicalite samples was measured to monitor the change of available surface area of calcined and functionalized samples (

Table 7). The value of external S_{sp} was used to calculate the average crystal size formulas described previously [189] and in the Experimental Procedures. The silicalite samples had crystal sizes of approximately 30, 150, and 500 nm. Upon calcination, the organic template is removed from the silicalite pores, and the measured surface area is the sum of external and internal S_{sp}. Functionalization of silicalite nanoparticles results in a decrease in the total specific surface area. In the case of APTES-functionalized silicalite, the total S_{sp} decreased by up to 20% as compared to the calcined sample. A more pronounced decrease was observed for CPTS-silicalite samples (up to 45%). This has been observed previously for functionalized zeolites and is attributed to pore blocking by the organic groups that are grafted onto the surface possibly near the entrance to the zeolite pores.[169] Thermogravimetry was used to measure the functional group loading of the silicalite samples. A representative TGA curve is shown in Figure 42, and the quantitative results are tabulated in

Table 7.

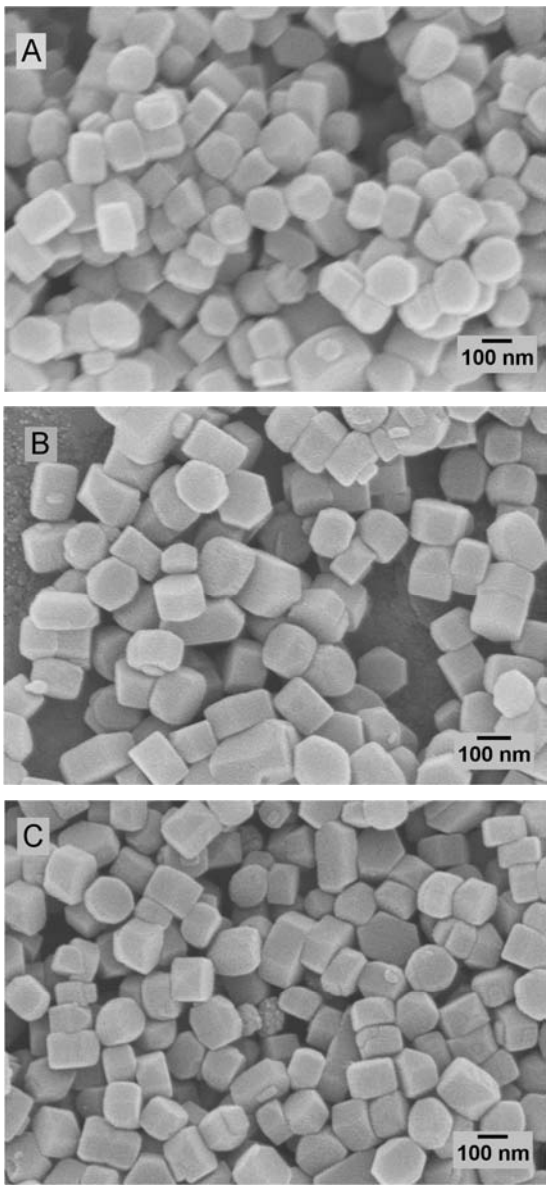

Figure 41. Representative SEM images of A) calcined silicalite-153, B) APTES-silicalite-153 and C) CPTS-silicalite-153. Scale bars are 100 nm.

Table 7. Physicochemical Properties of Functionalized Silicalite-1 Samples

Sample	Average particle diameter[a], nm	S_{sp}[b], m^2/g Calcined (as-synthesized)	Surface Coverage[c], mmol/g	ζ potential, mV @pH=7.4[d]
Silicalite-1-31	31	340 (104)	--	-27.8
APTES-Silicalite-1-31	31	280	0.240	5.1
MPTS-Silicalite-1-31	31	313	0.176	-11.1
Silicalite-1-50	50	336 (64)	--	-22.6
COOH-Silicalite-1-30	50	203	0.096	-39.0
Silicalite-1-153	153	298 (21)	--	-25.2
APTES-Silicalite-1-153	153	240	0.098	-4.06
MPTS-Silicalite-1-153	153	275	0.069	-16.2
COOH-Silicalite-1-153	153	189	0.075	-29.1
Silicalite-1-506	506	326 (6)	--	-31.1
APTES-Silicalite-1-5-6	506	269	0.066	-11.7
MPTES-Silicalite-1-506	506	265	0.056	-19.2
COOH-Silicalite-1-506	506	178	0.077	-43.9

[a] Calculated from external surface area of as-synthesized silicalite samples as determined from nitrogen adsorption and the BET method.

[b] Specific surface area from nitrogen adsorption and the BET method

[c] Measured by TGA

[d] Calcined samples

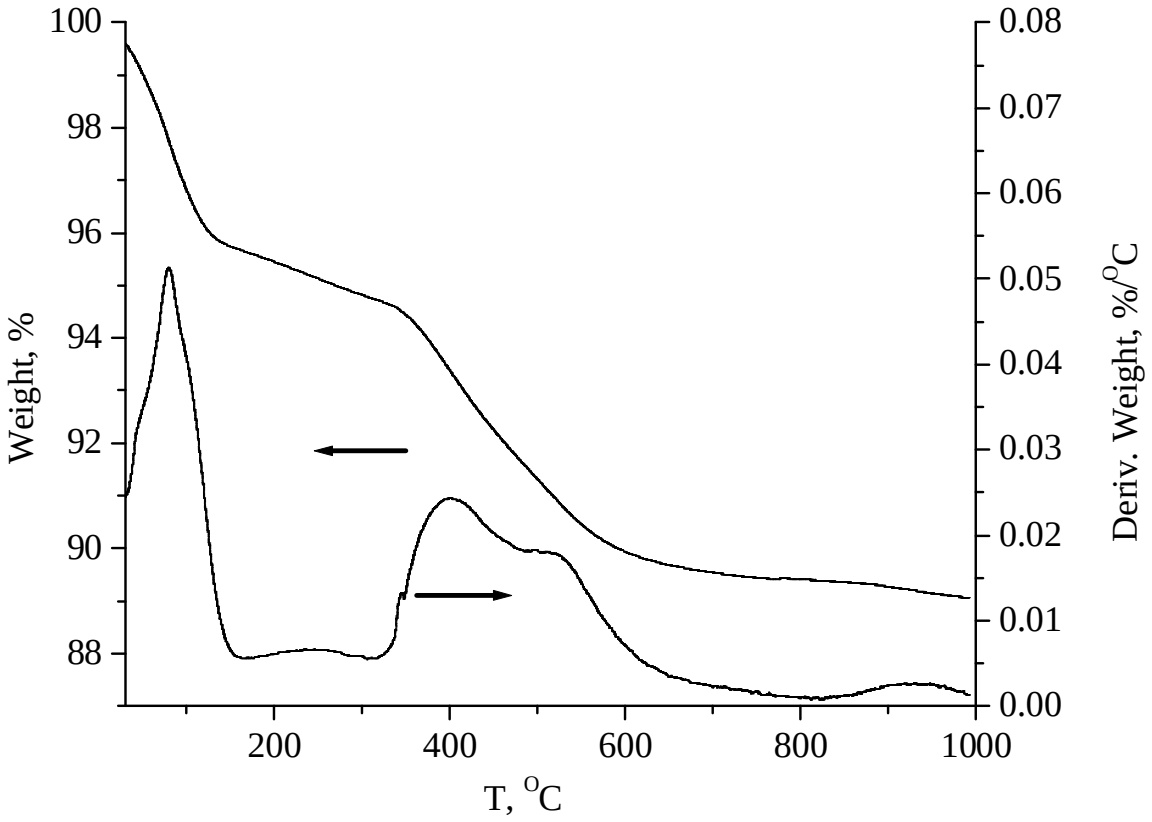

Figure 42. TGA graph of APTES-silicalite-31 functionalized zeolite.

The TGA curves were similar for the different-sized silicalite samples. The amount of APTES functionalization in mmol/g silicalite increases from 0.066 mmol/g for APTES-silicalite-506 to 0.240 mmol/g for APTES-silicalite-31, which shows that the increased external surface area leads to increased capacity for surface functionalization.[174]

The ζ-potential represents the surface charge of the particles in solution and varies with pH and ionic strength. The ζ-potentials for the calcined silicalite at pH 7.4 in phosphate buffer solution are listed in

Table 7. The variation of the ζ-potential as a function of pH is shown in Figure 43 for silicalite with different functional groups. The ζ-potential shows similar trends with pH and functional groups for all of the silicalite sizes studied here. The ζ-potential of unfunctionalized silicalite reflects the protonation of surface hydroxyl groups according to the equilibrium shown in Figure 44A.

The ζ-potential ranged from -28 to -31 mV for the different sized silicalite samples, indicating that the surface silanol groups are deprotonated to SiO^- as indicated in Figure 44A. The ζ-potential is expected to change when the silicalite surface is functionalized with different organic groups. For example, the ζ-potential for APTES-functionalized silicalite is governed by the following equilibrium involving the protonation of the surface amine groups (Figure 44B).

Functionalization of silicalite with APTES leads to a marked positive shift of ζ-potential in comparison with calcined silicalite sample. The ζ-potential for APTES-silicalite-31 is more positive than the ζ-potential for the calcined silicalite. This reflects that the amine groups in the samples are protonated in this range of pH and is in agreement with alkylamine behavior in aqueous solutions. The ζ-potential for CPTS-silicalite-1 is governed by the following equilibrium involving the protonation of the surface carboxy groups (Figure 44C).

Calculations of % ionization for propionic acid (which is expected to have a similar pK_a) show that about 10% of the acid is dissociated at pH 4 and almost completely dissociated at pH 8. Therefore, a smaller change in ζ-potential cannot

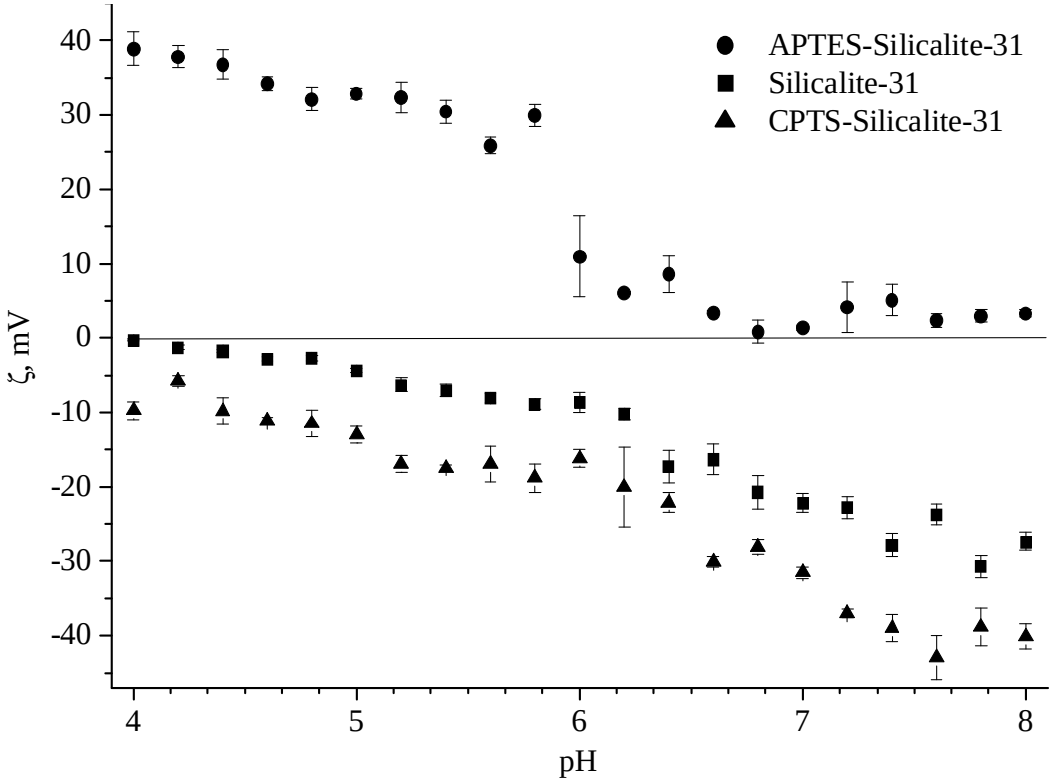

Figure 43. Zeta potential vs. pH titration curves for silicalite-31 calcined (■), APTES functionalized (●), and CPTS-silicalite-50 (▲).

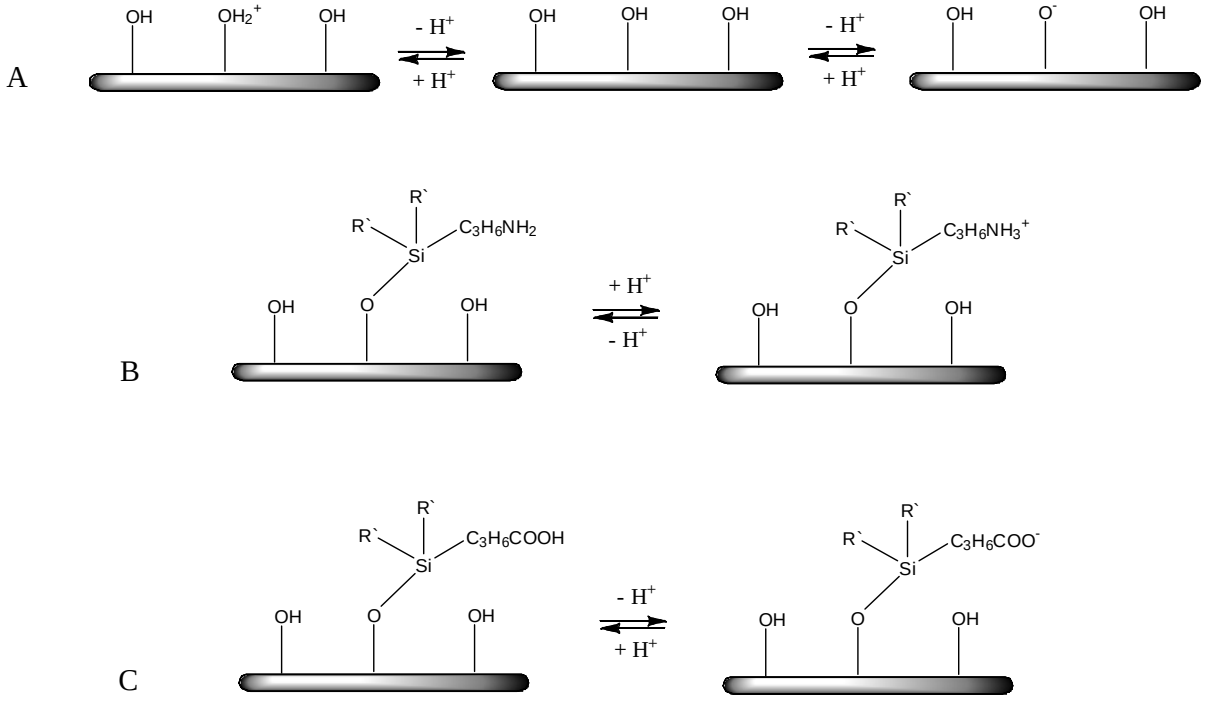

Figure 44. Surface charge equilibrium of unfunctionalized (A), APTES- (B) and CPTS functionalized (C) zeolite surface.

be justified by the small dissociation constant. Another reasonable explanation is that reflux in sulfuric acid results in lower surface coverage with carboxy groups as some of them may be completely oxidized.

Silicalite samples with different sizes (~30, 150, and 500 nm) were thoroughly characterized to ensure that the materials were crystalline and to determine the textural properties such as surface area and particle size. After functionalization with three different functional groups (amino, thiol, and carboxy), the silicalite-1 samples were further characterized by ^{29}Si (Figure 45), ^{13}C CP-MAS NMR (Figure 46), and TGA to assess the functional group loading and molecular structure of the organic moiety and by ζ-potential to determine the stability and surface charge in phosphate buffer solution. The measurement of ζ-potential in phosphate buffer solution underscores the importance of characterization in the medium being used for the cytotoxicity study so that an understanding of the properties of the materials in the appropriate medium is obtained.

Generation of hydroxyl radicals by the zeolite surface was studied by means of EPR. 5,5-dimethyl-1-pyrroline-N-oxide (DMPO) is used as a spin trap in the study. DMPO is EPR inactive but it can react with a number of different radicals, such as hydroxyl radicals, and form EPR active adducts (Figure 47).[196, 197] These adducts are relatively stable and their EPR spectra can be recorded. The intensity of peaks in the spectra correlate with the amount of hydroxyl radicals generated by the zeolite surface and therefore ability of zeolite samples with different particle size and organic functional group type can be compared. Typical 1:2:2:1 splitting characteristic of DMPO-OH adduct originates from splitting by the nitrogen and proton, as shown in the hyperfine splitting diagram (Figure 48).[194] Representative EPR spectra of non-functionalized and functionalized zeolites in Figure 49, and the EPR results are summarized in Table 8.

The ability of non-functionalized zeolites to generate hydroxyl radicals appear to be independent of particle size. Functionalization of zeolites with amino- and mercaptopropyl groups decreases the amount of generated hydroxyl radicals

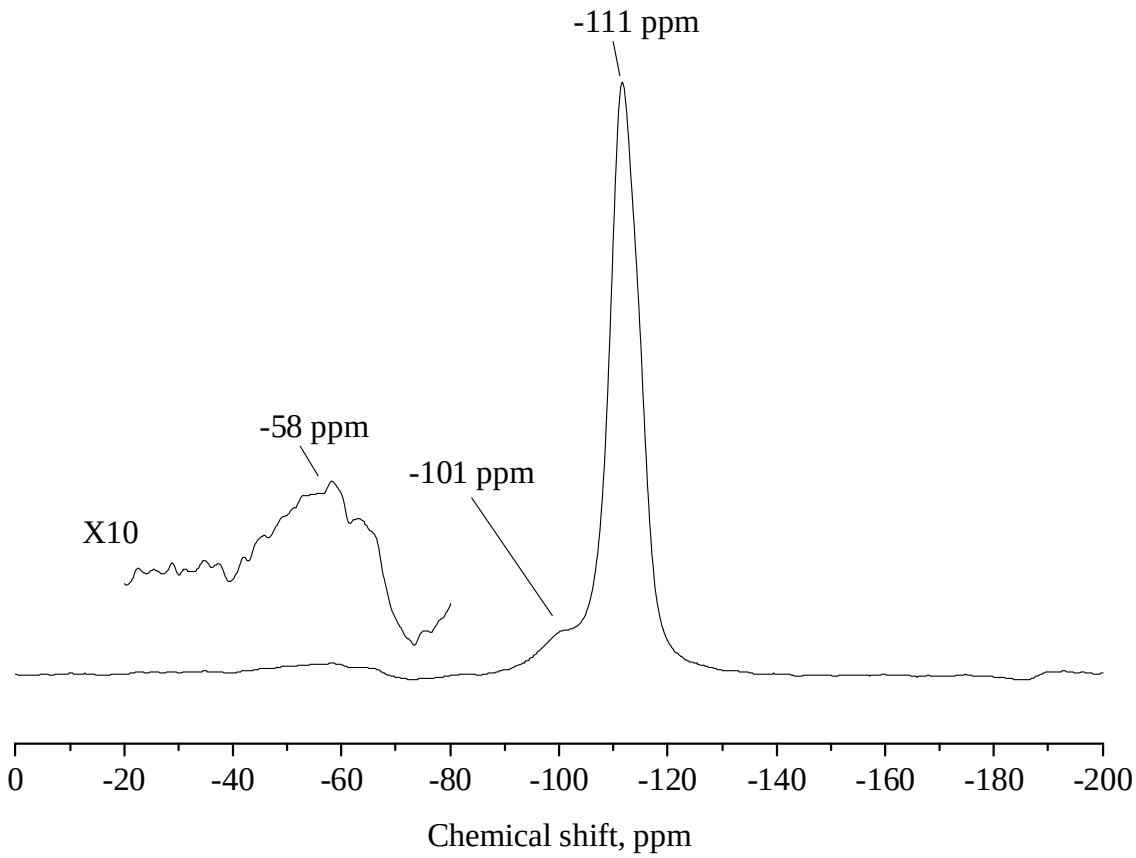

Figure 45. ^{29}Si MAS NMR of APTES-silicalite-31 sample.

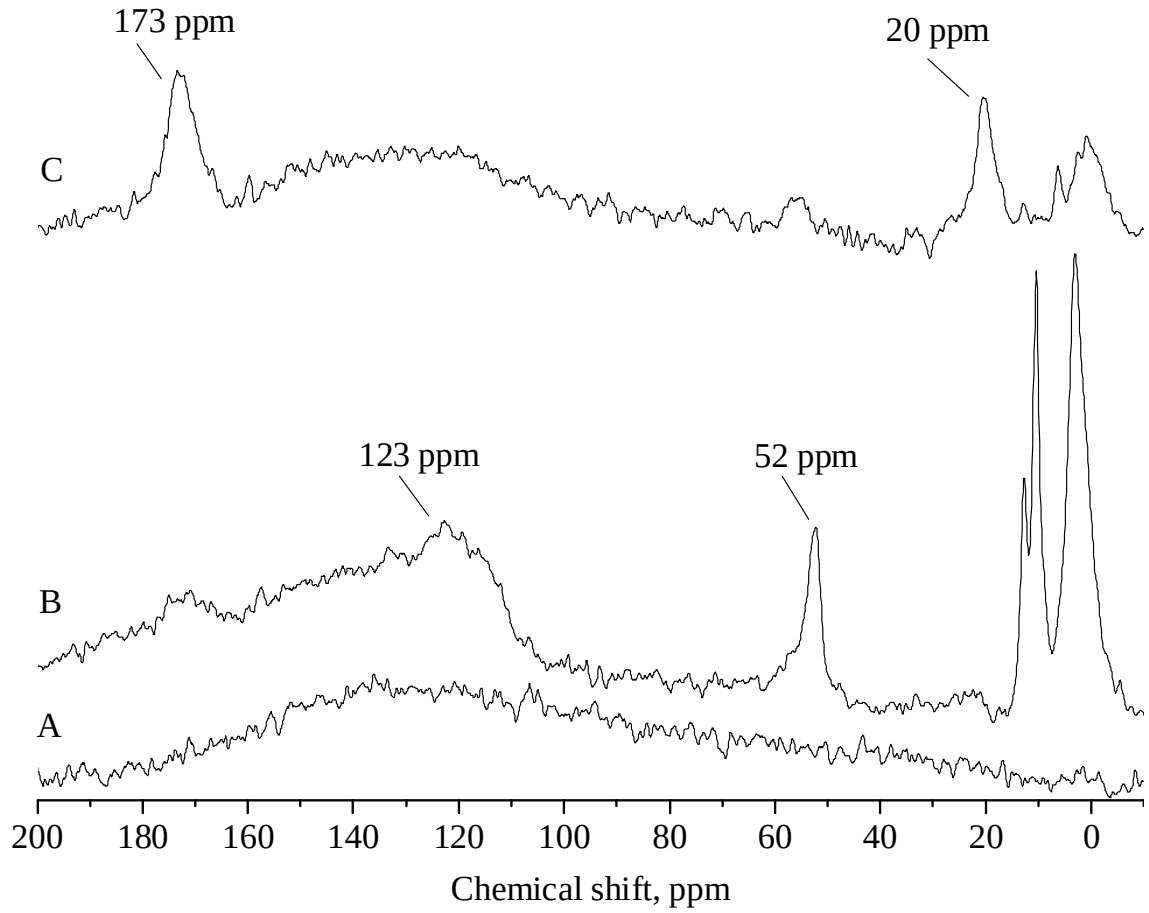

Figure 46. ^{13}C CPMAS NMR of silicalite-1-50 calcined (A), cyanopropyl (B) and carboxypropyl (C) functionalized samples.

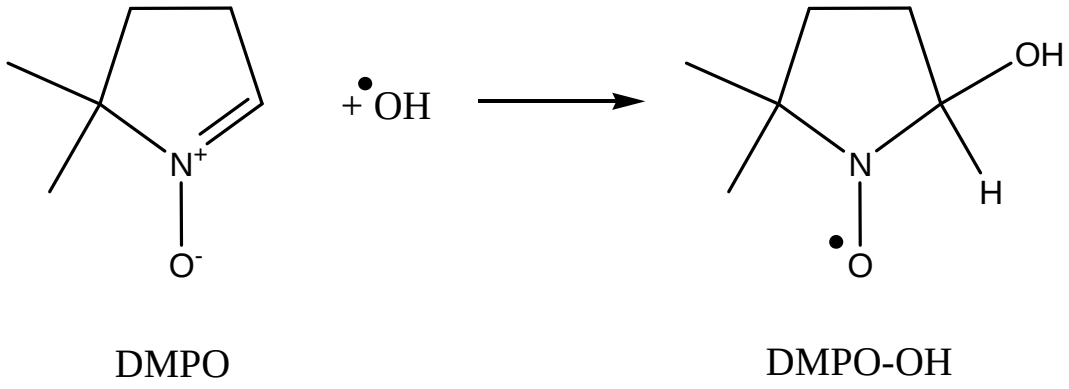

Figure 47. Scheme of reaction between DMPO and hydroxyl radicals.

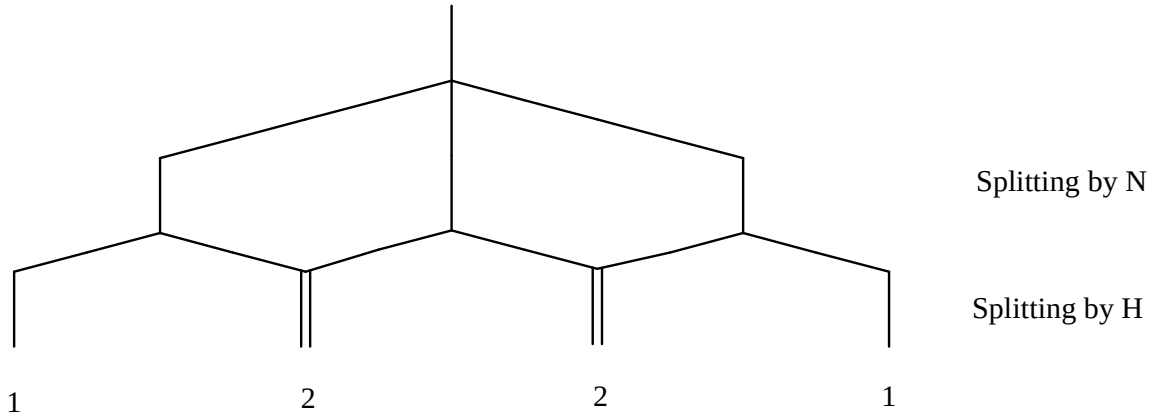

Figure 48. Hyperfine splitting diagram of DMPO-OH adduct.

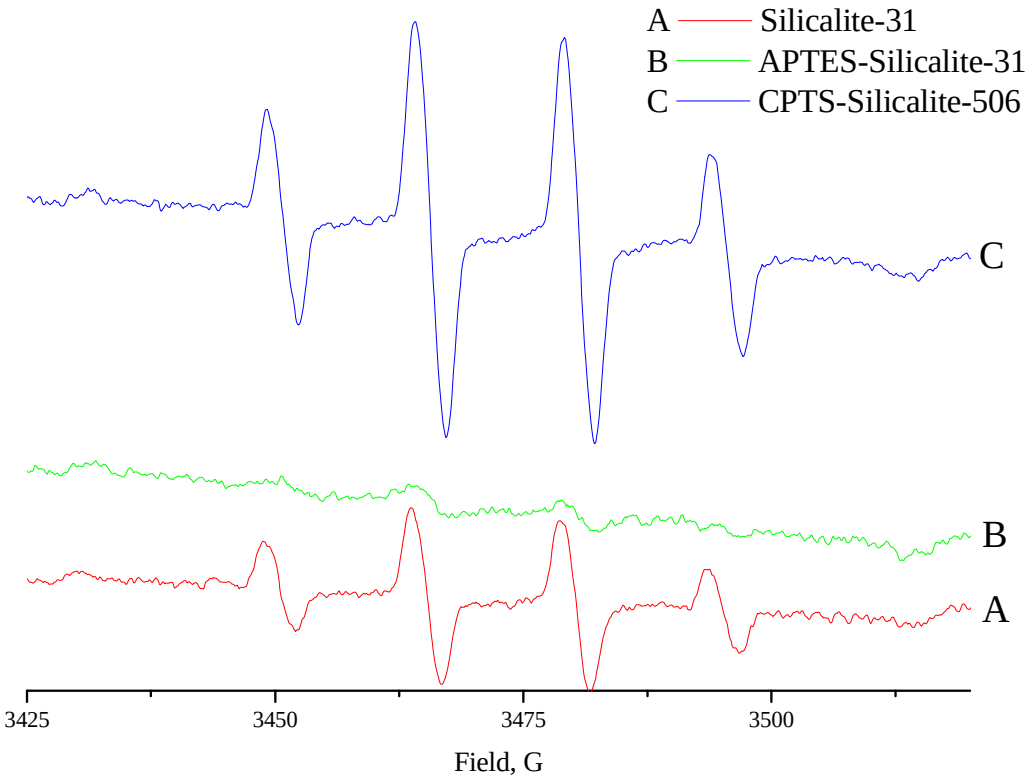

Figure 49. Representative EPR spectra of Silicalite-1 samples (before normalization by sample weight).

Table 8. EPR studies of radical generation by zeolite nanocrystals. The integrated intensities were normalized to that of Silicalite-31

	Particle diameter, nm		
	31*	153	506
Calcined	1.00	0.66	0.94
APTES	low	low	2.58
MPTS	low	1.40	1.08
CPTS	0.88	0.97	3.21

*Silicalite-50-CPTS was used

in small zeolite particles but does not have such effect on 500 nm zeolite crystals. Functionalization with carboxypropyl groups of largest zeolite crystals resulted in a significantly increased generation of hydroxyl radicals, which was the highest among the studied samples. The absence of direct correlation between the ROS generation activity and the cytotoxicity of the sample can be explained multiple mechanisms affecting cytotoxic activity, ROS generation being one of them. The amount of generated hydroxyl radicals is shown relative to one of the samples, so there is no absolute value available. Some studies indicated that the ability of silica surface to generate ROS decreases as the sample is aged.[198, 199] Since the timeframe between synthesis of zeolites and cytotoxic studies or EPR measurements was considerable, the absolute amount of generated ROS in the samples may be too low to have a significant contribution to cytotoxicity.

Toxicity of the Silicalite nanoparticles is determined by measuring leakage of LDH and Caspase 3/7 molecules. The silicalite nanoparticles of different sizes and different functionalization were tested using the LDH release assay (Figure 50) and the caspase 3/7 activity assay (Figure 50) to determine the degree of necrosis and apoptosis induced in HEK293 cells and RAW264.7 cells. These results were confirmed qualitatively using Annexin V-PI staining. Toxicity as measured by leakage of LDH is dependent on dose, size, and type of surface functionalization of silicalite nanoparticles and the cell type being tested. In HEK293 cells, low levels of LDH release were detected at concentrations of 0.25 and 0.5 mg/mL of silicalite nanoparticles (Figure 50a). Increasing the concentration of 30 nm silicalite nanoparticles incubated with the HEK293 cells increased LDH release activity by 2-3-fold ($P < 0.001$). While increasing the concentration of 30 nm silicalite nanoparticles incubated with HEK293 cells significantly increased LDH release activity, the surface functionalization of the silicalite nanoparticles with amine or thiol groups did not significantly change LDH release activity ($P > 0.05$). Functionalizing the surface of the 30 nm silicalite nanoparticles with amine or thiol groups had no significant effect on LDH release activity in RAW264.7

cells ($P > 0.05$). In RAW264.7 cells, increasing the dose of 30 nm silicalite nanoparticles from 0.25 to 1 mg/mL increased LDH release activity by 3-5%; however, relative to untreated controls, this was considered nontoxic (Figure 51). In HEK293 cells, the 150 nm calcined silicalite nanoparticles were nontoxic at all doses tested. In contrast, amine-, carboxy-, and thiol-functionalized silicalite nanoparticles all demonstrated dose-dependent toxicity with a 2-3-fold increase in LDH release activity when the dose was increased from 0.25 to 1 mg/mL ($P < 0.01$). Data from the LDH release activity assay showed that cell membrane damage was induced by nanoparticles functionalized in the following order: amine > carboxy > thiol > calcined. In RAW264.7 cells, all 150 nm silicalite nanoparticles at or below 0.5 mg/mL dosing concentration were nontoxic. At 1 mg/mL dosing, however, calcined, carboxy-, and thiol-functionalized 150 nm silicalite nanoparticles all generated significant increases in LDH release activity that were approximately 4-fold higher than doses of 0.5 mg/mL ($P < 0.001$). The amine functionalized 150 nm silicalite nanoparticles generated nonsignificant dose-dependent increases in LDH release activity in RAW264.7 cells. At a dosing of 1 mg/mL, the amine functionalized silicalite nanoparticles were significantly less toxic than calcined, thiol-functionalized, and carboxy-functionalized silicalite nanoparticles ($P < 0.001$). This was only observed in the RAW264.7 cells ($P < 0.001$) and not the HEK293 cells ($P > 0.05$), indicating that reduced toxicity observed through amine functionalization is cell type-specific. At 500 nm, the silicalite nanoparticles demonstrated dose dependent toxicity in HEK293 cells, but these increases were small. Functionalization of the 500 nm silicalite nanoparticles did not significantly change the LDH release activity in HEK293 cells. In comparison, the functionalized 500 nm silicalite nanoparticles generated significant dose-dependent LDH release activity/toxicity in RAW264.7 cells that increased approximately 5-9-fold when the dose was increased from 0.25 to 1 mg/mL ($P < 0.001$).

Functionalization of the silicalite nanoparticles had a significant impact on LDH release activity with thiol functionalized silicalite nanoparticles generating the highest

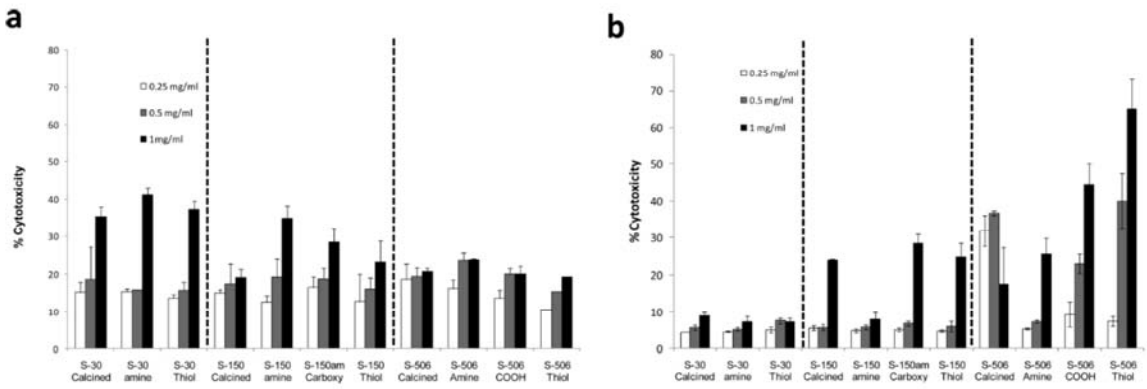

Figure 50. Cytotoxicity of calcined, amine-functionalized, thiol-functionalized, and carboxy-functionalized silicalite nanoparticles after 4 h of incubation in (a) HEK293 cells and (b) RAW264.7 macrophages as measured by the extent of LDH release. The extent of enzyme leakage is expressed as a percentage of the total activity (mean ±SD of three separate experiments).

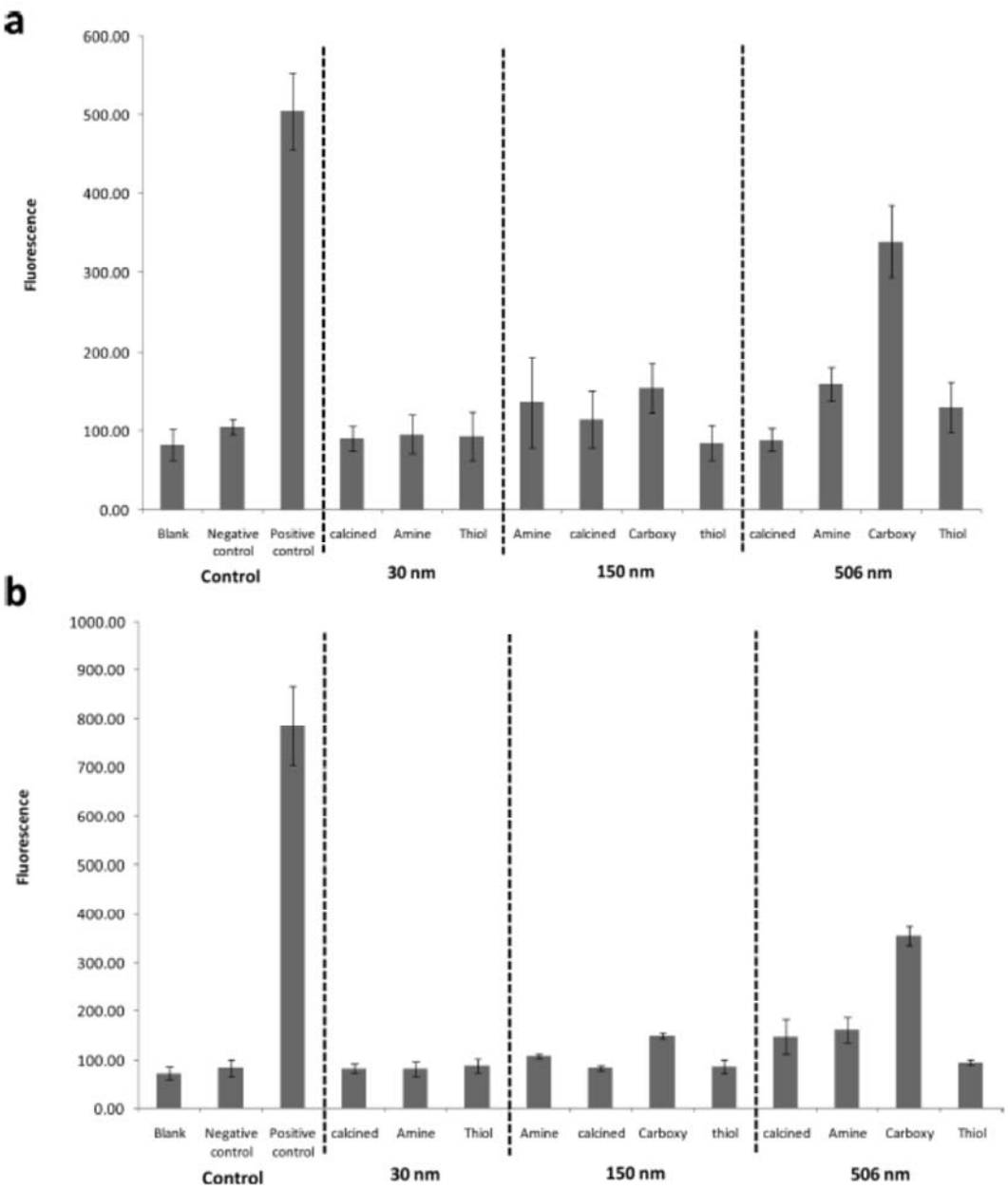

Figure 51. Cytotoxicity of calcined, amine-functionalized, thiol-functionalized, and carboxy-functionalized silicalite nanoparticles after 4 h of incubation in (a) HEK293 cells and (b) RAW264.7 macrophages as measured using the caspase 3/7 activity assay. Fluorescence is measured using 485 (excitation) and 527 nm (emission) wavelengths and presented as the mean ± SD of three separate experiments.

toxicity at 1 mg/mL dosing in RAW264.7 cells. Functionalization of the 500 nm silicalite nanoparticles increased toxicity in the following order thiol > carboxy > amine, and in contrast to HEK293 cells, these differences were significant ($P < 0.001$). In HEK293 cells at 1 mg/mL dosing, the 30 nm silicalite nanoparticles generated the highest toxicity regardless of functionalization, while the 30 nm silicalite nanoparticles had no significant impact on LDH release activity in RAW264.7 cells. In contrast, the 500 nm silicalite nanoparticles at 1 mg/mL generated the highest LDH release activity in RAW264.7 cells, and the degree of toxicity was linked to the nature of the functionalization. These same 500 nm silicalite nanoparticles did not cause significant LDH release activity/toxicity in HEK293 cells regardless of the type of functionalization. Toxicity as measured by caspase activity is most significant in cell lines treated with carboxy-functionalized 500 nm Silicalite nanoparticles. The results of the caspase activity assays are shown in Figure 51a for HEK293 and Figure 51b for RAW264.7. In HEK293 and RAW264.7 cells, 30 nm silicalite nanoparticles did not generate any significant caspase activity regardless of functionalization ($P > 0.05$). At a size of 150 nm, the silicalite nanoparticles that were calcined or functionalized with thiols did not generate significant increases in caspase activity relative to untreated controls in HEK293 or RAW264.7 cells ($P > 0.05$). Functionalization of the 500 nm silicalite nanoparticles did increase caspase activity with increases in the following order, carboxy > amine > calcined > thiol, for both HEK293 cells and RAW264.7 cell lines. The 500 nm silicalite nanoparticles generated the highest levels of caspase activity in HEK293 cells (except calcined 500 nm silicalite nanoparticles) and RAW264.7 cells in comparison to 150 nm silicalite nanoparticles and 30 nm silicalite nanoparticles regardless of functionalization. Functionalization of the 500 nm silicalite nanoparticles had a direct impact on caspase activity with the order of carboxy >> amine > thiol. The carboxy-functionalized500 nm silicalite nanoparticles generated significantly higher caspase activity than all other functionalizations and sizes of silicalite nanoparticles in HEK293 and RAW264.7 cells ($P < 0.001$). The LDH release

assay and the caspase 3/7 assay were also carried out at different time points, and similar differences in the various groups were observed. Annexin V-PI staining confirms results from LDH release assay and Caspase 3/7 activity assays. Figure 52b shows HEK293 cells treated with 30 nm thiol-functionalized silicalite nanoparticles. Consistent with the results from the LDH release assay and the caspase 3/7 activity assay, the HEK293 cells are primarily stained with PI with limited Annexin-V fluorescent signals detected, suggesting that necrosis is the primary mechanism of cell death. Figure 52c shows HEK293 cells treated with carboxy-functionalized 500 nm silicalite nanoparticles. The majority of the HEK293 cells are doublestained with Annexin V and PI with apoptosis found to be the primary mechanism of cell death, and this is consistent with the high caspase activity that was detected with this group. In RAW264.7 cells incubated with 500 nm carboxy-functionalized silicalite nanoparticles, in which both high LDH activity and caspase activity was induced, significant cell death was observed through necrosis and apoptosis (Figure 52d). Similar confocal fluorescent images provided visual confirmation of the type of cell death being induced by each of the various silicalite nanoparticles groups with different sizes and different surface functionalizations tested.

5.5 Discussion

Increasing evidence in the field of nanotoxicity is showing that the size, crystallinity, surface morphology, surface charge, and surface functional groups can have a significant impact on the degree of toxicity induced in vitro and in vivo.[190-193, 200, 201] In this study, we complement existing data on toxicity induced by porous silica-based nanoparticles by showing, for the first time, the effect of size and type of surface functionalization on apoptosis and necrosis-based toxicity.[174, 186, 187, 202] It is increasingly being recognized that a thorough physicochemical characterization of nanoparticles prior to testing for toxicity is essential to successfully correlate the properties of the nanoparticles to the toxicity profiles.[191, 192, 203] In this study, we have carefully

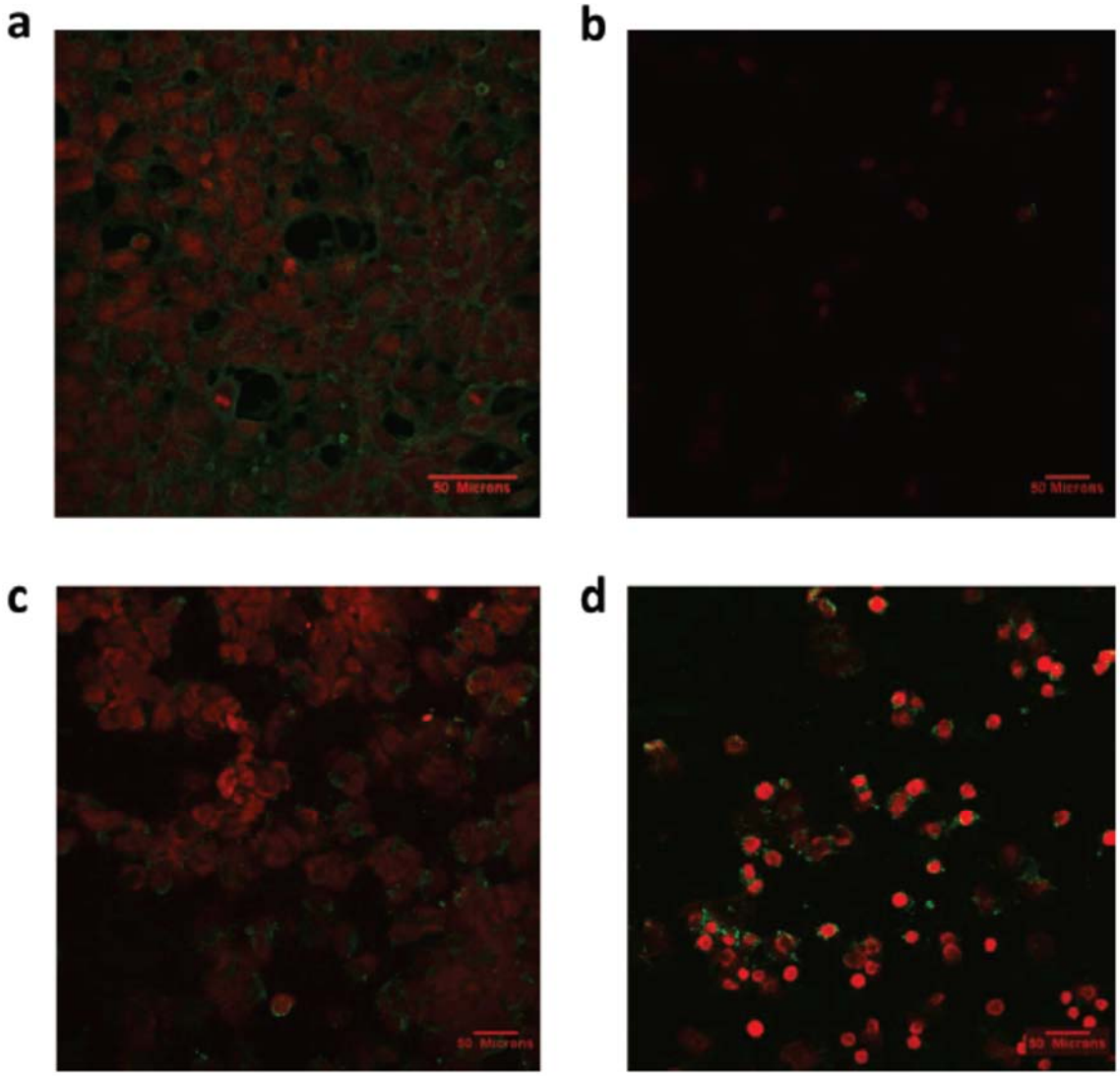

Figure 52. Representative confocal microscopy images of cells treated with Annexin V-PI staining. (a) Positive control of cells treated with 1 μM staurosporine for 2 h, (b) HEK293 cells incubated with 30 nm silicalite nanoparticles functionalized with thiol groups for 4 h, (c) HEK293 cells incubated with 500 nm silicalite nanoparticles functionalized with carboxy groups for 4 h, and (d) RAW264.7 macrophages incubated with 500 nm silicalite nanoparticles functionalized with carboxy groups for 4 h.

characterized the size, shape, surface morphology, surface charge, and surface functionalization of nanoscale silicalite using analytical tools such as NMR, TGA, powder XRD, nitrogen adsorption, and dynamic light scattering. In particular, the measurements of the size and surface charge were conducted in the buffer solutions that were used for the cytotoxicity assays.

To measure toxicity, we first measured LDH levels. The leakage of LDH from cells provides a direct measure of the damage/integrity to the cell membrane. At the highest concentrations tested for LDH activity, we then tested the silicalite nanoparticles with different functionalizations and different sizes for toxicity using the caspase 3/7 activity assay. Some of the key molecules involved in apoptosis are members of a family of cysteine aspartic acid-specific proteases called caspases. Caspases participate in a proteolytic cascade that leads to the programmed death of cells. Initiator caspases such as caspases 8 and 10 have an early role in the cascade, while effector caspases such as caspases 3, 6, and 7 are involved at later stages. As a result, measuring caspase 3/7 activity allows for a strong correlation of the degree of apoptosis occurring in a cell population. The Apo-ONE Homogeneous Caspase-3/7 Assay works by providing cells with a substrate that fluoresces following cleavage by the activated caspases 3 and 7. The Annexin V-PI staining method was then used to provide visual confirmation of the type of cell death induced by the different functionalized silicalite nanoparticles. Annexin-V FITC is a 35.8 kDa protein that has a strong natural affinity for phosphatidylserine, a membrane phospholipid that, soon after apoptosis initiates, translocates from the inner to the outer surface of the cell plasma membrane. Cells with preserved membranes are impermeable to PI. However, PI enters those cells with a damaged membrane, staining the DNA red.

The degree of LDH release induced by silicalite nanoparticles is dependent on dose and particle size, but the impact of the particle size is dependent on the cell type being tested. In HEK293 cells, an increase from 0.5 to 1 mg/mL for 30 and 150 nm

silicalite nanoparticles significantly increased LDH release. An increase of 0.5 to 1 mg/mL for 500 nm nanoparticles did not significantly increase LDH levels in HEK293 cells. Surprisingly, and in contrast to the HEK293 cells, increasing the dose of 30 nm silicalite nanoparticles from 0.5 to 1 mg did not cause a significant increase in toxicity when incubated in RAW264.7 cells. However, increasing the dose of 150 and 500 nm silicalitenanoparticles from 0.5 to 1 mg did cause a significant increase in toxicity when incubated in RAW264.7 cells. Increasing the dose of larger silicalite nanoparticles increased toxicity in RAW264.7 cells, while increasing the dose of smaller silicalite nanoparticles increased toxicity in HEK293 cells.

These results are most likely related to the biological characteristics of each of these cell lines. HEK293 cells, which are a hypotriploid human cell line derived from the kidney and commonly used for drug and gene delivery efficacy testing, will preferentially internalize particles that are less than 300 nm by clathrin-mediated endocytosis.[204] Particles above the 250-300 nm cutoff for endocytosis including the 500 nm silicalite nanoparticles would likely have greater difficulty entering the cell by this route, and the toxicity of these particles even with increasing dose would therefore be expected to be reduced. In contrast, the RAW264.7 cells are a macrophage-like cell line that have a greater capacity to phagocytose much larger particles extending into the micrometer-size range. As such, 500 nm particles would be expected to be internalized more easily in RAW264.7 cells when compared to HEK293 cells, and this would account for the dose-dependent toxicity at higher particle sizes. Interestingly, a recent study by Thrall et al. has shown that changing the size of silica nanoparticles from 10 to 500 nm did not significantly change any of the 1009 gene sets they tested that were present in RAW264.7 cells. This suggests that it is not genotoxicity that is being affected by the size of the silicalite nanoparticles.[205] Results are presented on a per mass basis, which is the most common approach used in nanoparticle drug delivery research and many other toxicity studies.[145, 150, 168, 174, 175, 186, 200, 206–210]

Fubini and co-workers have shown that the surface area and aspect ratio of porosils in the 0.5-15 μm size range correlate with macrophage toxicity.[174] These results showed that the porosil aspect ratio and external surface area correlated with cytotoxicity. An increase in external surface area led to an increase in the observed cytotoxicity of the monocyte-macrophage cell line (J774). Rodlike zeolite crystals also showed an increase in cytoxicity with increasing aspect ratio. Because the RAW264.7 cell line is a macrophage cell line, the experiments reported here with silicalite and the RAW264.7 cell line can be best compared to the studies of Fubini and co-workers. However, the toxicity of silicalite does not correlate with the surface area. For example, 30 nm silicalite particles have the largest external surface area yet show markedly lower toxicity relative to the largest 500 nm silicalite particles. Our studies were conducted with zeolite particles in a much smaller size range (the lower limit in the Fubini study is our upper limit for crystal size), and thus, as discussed above, the endocytosis process may be quite different. In a related study on mesoporous silica, Asefa and co-workers found that the cytotoxicity was related to absorptive surface area, but the nature of the surface functional group could not be ruled out.[186] A distinct difference between the mesoporous silica and the zeolitic materials is that the pore size of the mesoporous silica materials studied is significantly larger, suggesting that the internal surface could have a greater role in cytotoxicity because it is accessible to a wider range of biological molecules. These previous studies both suggest that the role of the zeolite surface area plays an important and complex role in determining the cytotoxicity of the materials.

In HEK293 cells, the dominant parameter effecting increased LDH release was dose and particle size regardless of surface functionalization. However, dose, particle size, and surface functionalization were linked to LDH release activity in RAW264.7 cells. Surface functionalization did not change the degree of toxicity in RAW264.7 cells incubated with 30 nm silicalite nanoparticles but did change toxicity induced by the 153 and 500 nm silicalite nanoparticles. For example, the larger 500 nm silicalite

nanoparticles showed dose-dependent increases in toxicity that increased with surface functionalization in the order of amine < carboxylic acid < thiol. The amine-functionalized silicalite exhibits the lowest toxicity for both the 153 and the 500 nm silicalite particles and the most positive ζ-potential, suggesting some correlation with surface charge. Thiol groups have been reported to inhibit NO production, which is also linked to S-nitrosoglutathione (GSNO) production.[211-213] One potential reason that thiol-functionalized 500 nm silicalite nanoparticles trigger strong LDH release but not apoptosis may be related to interference with levels of S-nitrosoglutathione (GSNO) and nitric oxide (NO) production. When GSNO is depleted, toxicity is induced in macrophages that is predominantly caused by necrosis.[211] This could account for the large LDH release but low caspase 3/7 activity observed in RAW264.7 cells when treated with thiol-functionalized 500 nm silicalite nanoparticles.

Carboxylic acid-functionalized 500 nm silicalite nanoparticles generated significantly higher levels of caspase 3/7 activity when compared to all other groups. Previous studies comparing quantum dots coated with either amine groups or carboxylic acid groups have shown that the quantum dots coated with COOH groups to be significantly more toxic. These particles stimulated significantly higher pro-inflammatory cytokines such as IL-6, IL-8, and IL-10 that have been reported to be correlated with immunotoxicity and apoptosis.[214] In addition, other studies have shown that COOH-coated nanoparticles are efficiently taken up by cells such as macrophages.[215] It is likely that COOH-coated silicalite nanoparticles generate the strongest reactive oxygen species (ROS) production, which has been reported to be correlated to high levels of caspase 3/7 activity and apoptosis.[216] Studies on quartz dusts have shown that surface modification can dramatically influence the toxicity.[180, 202] For example, quartz modified with aluminum lactate or polyvinylpyridine-N-oxide (PVNO) was significantly less toxic, and this was correlated to lower production of hydroxyl radicals when the modified quartz was exposed to hydrogen peroxide. Preliminary studies of the radical-generating ability

of our silicalite samples in the presence of hydrogen peroxide do not show a clear correlation with toxicity. Future studies will focus on measuring the production of hydroxyl radical species, ROS, pro-inflammatory cytokines, NO production, and GSNO production to evaluate the role of oxidative stress, immunotoxicity, and GSNO/NO levels on the degree of apoptosis and necrosis triggered in cells.

5.6 Conclusions

In summary, the cytotoxicity of nanoscale silicalite is complex and depends on the particle size, surface functional group, and cell line used for the toxicity studies. The differences observed in toxicity based on cell type are most likely due to the different mechanisms for nanoparticle uptake by the HEK293 and RAW264.7 cell lines. The effect of surface functionalization on cytotoxicity also depends on the cell line. Smaller silicalite particles show dose-dependent toxicity in HEK293 cells that is not dependent on surface functionalization, and larger particles show dose-dependent toxicity in RAW264.7 cells that is dependent on functionalization. The mechanism for cell death was examined and was also found to depend on the cell line. Thiol-functionalized 500 nm silicalite nanoparticles predominantly cause toxicity by necrosis in RAW264.7 cells, while COOH-functionalized 500 nm silicalite nanoparticles predominantly trigger apoptosis as measured by caspase 3/7 activity in HEK293 and RAW264.7 cells.

The study was done in collaboration with Dr. Aliasger K. Salem, College of Pharmacy, University of Iowa. The results were published in Chemical Research in Toxicology, year of 2009, volume 22, pages 1359-1368, and authored by Petushkov, Intra, Graham, Larsen and Salem.

CHAPTER 6

FRAMEWORK STABILITY OF NANOCRYSTALLINE NaY IN AQUEOUS SOLUTION AT VARYING pH

6.1Abstract

Nanocrystalline zeolites are emerging as important materials for a variety of potential applications in industry and medicine. Reducing the particle size to less than 100 nm, results in advantages for nanocrystalline zeolites relative to micron-sized zeolite crystals, such as very large total and external specific surface areas and reduced diffusion path lengths. Understanding the physical and chemical properties of zeolite nanocrystals is imperative for further development and application of nanocrystalline zeolites. In this study, the framework stability of nanocrystalline NaY zeolite with a crystal size of 66 nm and Si/Al=1.74 was investigated at pH = 7.4, 4, 2 and 1. The solids and solutions were analyzed using several different analytical techniques. The relative crystallinity and crystal size and morphology of the solids were examined by powder X-ray diffraction (XRD) and transmission electron microscopy (TEM), respectively. The aluminum content, Si/Al and coordination were monitored by inductively coupled plasma/optical emission spectroscopy (ICP/OES), x-ray photoelectron spectroscopy (XPS) and aluminum-27 solid state magic angle spinning NMR. As the acidity of the medium increased, the framework stability of nanocrystalline NaY decreased. Treatment of the zeolite samples at pH = 1 resulted in complete degradation of the zeolite framework after 1 h. An increase in Si/Al was also observed suggesting selective removal of aluminum at low pH.

6.2 Introduction

Zeolites are a class of aluminosilicates that have a well-defined crystal structure and pore network. The presence of silanol groups and ion exchange sites on the zeolite surface provides a variety of ways to modify the zeolite and to tune its properties for

specific applications.[217-219] Recently, there has been a growing interest in nanocrystalline zeolites that have large surface areas like their bulk analogs, with the distinction that the external surface area constitutes a significant fraction of the total surface area.[18, 27, 101, 189] Nanocrystalline zeolites have been used in catalysis,[220] fine chemical synthesis of large organic molecules,[124] as molecular separation membranes,[221] and optically active materials.[222] Nanocrystalline zeolites have also been used to produce multifunctional materials for MRI applications[172] and protein digestion systems.[223] Zeolite particle size is especially important in MRI and drug delivery applications due to size restricted access of particles inside the cells.[224] Nanocrystalline zeolites have been found to promote pDNA transfection into the HEK-293 cells.[150] Cellular toxicity of nanocrystalline Silicalite-1 was evaluated for two different cell lines as function of particle size, concentration and the type of surface functionalization.[225]

One of the most important factors when determining zeolite suitability for applications is the stability of its framework under relevant conditions. Information about zeolite dissolution is important from the perspective of using zeolites as aluminum sources for the synthesis of zeolites or mesoporous aluminosilicates. For example, zeolites can be dissolved under basic[226] or acidic conditions[227] and used as an aluminum source for the synthesis of mesoporous aluminosilicates. For other applications of zeolites in catalysis, water treatment and biomedical application such as imaging, the stability of zeolites in aqueous solution is critically important.

Zeolite framework stability at elevated temperature,[228, 229] and in fluid catalytic cracking conditions[230] has been previously studied. In a series of publications,[231-233] the dissolution kinetics of zeolite A (Si/Al = 1.0), zeolite X (Si/Al = 1.0) and mordenite (Si/Al = 4.4) in sodium hydroxide solutions at elevated temperatures were investigated. It was determined that the dissolution of the zeolites in a highly basic environment was dependent on the Si-to-Al ratio of the zeolite. For zeolite A, the Si-to-Al ratios in the samples did not change and for zeolite X, the Si/Al changed very little as the dissolution

proceeded. However, mordenite, which had a higher initial Si/Al than zeolites X and A had a different dissolution profile, such that the Si-to-Al ratio of the mordenite decreased over the dissolution time period. This phenomenon was explained by easier Si-O-Si bond breakage in comparison to Si-O-Al bond breakage in alkaline medium.

Dissolution behavior of several types of zeolites in a highly acidic medium was investigated by Hartman and Fogler.[234, 235] They also found that the Si-to-Al ratio of the starting zeolite material affected the dissolution profile of the zeolites studied. Low Si-to-Al ratio lead to complete stoichiometric dissolution of the zeolite, while higher Si/Al ratio (>1) resulted in selective removal of aluminum from the framework.

In these previous studies, micron-sized zeolite crystals were used. There is no information in the literature regarding stability of zeolites with crystal sizes less than 100 nm in aqueous medium. With growing use of nanocrystalline zeolites in new applications, it is critically important to evaluate the stability of nanocrystalline zeolites relative to bulk zeolites particularly as biomedical applications are developed.

In the present work, we investigated the framework stability of nanocrystalline NaY zeolite (FAU phase) with a crystal size of 66 nm and Si/Al=1.74. The low Si-to-Al ratio in this zeolite provides it with a large number of ion exchange sites. The combination of the large pore size and ion-exchange capacity may be beneficial for NaY use in biomedical applications, such as MRI and drug delivery. Therefore, pH = 7.4 was chosen to provide insight into zeolite framework stability under cellular and blood pH conditions. Dissolution experiments were conducted at pH = 7.4, 4, 2 and 1 and the resulting solids and solutions were analyzed separately with several different analytical techniques. The relative crystallinity and crystal size and morphology of the solids were examined by powder X-ray diffraction (XRD) and transmission electron microscopy (TEM), respectively. The aluminum content and coordination environment were monitored by inductively coupled plasma/optical emission spectroscopy (ICP/OES), X-

ray photoelectron spectroscopy (XPS), energy dispersive spectroscopy (EDS) and aluminum-27 solid-state magic angle spinning NMR, respectively.

6.3 Experimental Section

6.3.1 Zeolite synthesis

NaY nanocrystals were synthesized from a clear gel solution of the following composition: 3.4 TEOS : 2 AIP : 4.9 TMAOH : 370 H2O : 0.064 NaOH, where TEOS = tetraethylorthosilicate, AIP = aluminum isopropoxide and TMAOH = tetramethylammonium hydroxide. First, one half of TMAOH solution was mixed with AIP, water and sodium hydroxide and vigorously stirred for several hours at room temperature. The other half of TMAOH was mixed with TEOS and stirred in a separate flask under the same conditions. After AIP was completely dissolved, the two solutions were mixed together and stirred overnight. The zeolite NaY sample used in this study was synthesized from a recycled reaction mixture. Full details of nanocrystalline NaY synthesis from recycled reaction mixtures can be found elsewhere.[236] The recycled synthesis mixture was placed in a RB-flask and hydrothermally treated in an oil bath at 98 ^{o}C for 7 days. After completion of the synthesis, the NaY nanocrystals were separated from supernatant via centrifugation at 14000 rpm (20817 x g) for 20 minutes. The nanocrystals were subsequently washed and centrifuged twice with water and once with ethanol, and dried in an oven in air at 105 ^{o}C overnight. The zeolite was then calcined in oxygen at 550 ^{o}C for 12 hours in order to remove the organic template from the pores. The NaY was characterized by powder X-ray diffraction to confirm the zeolite identity and by nitrogen adsorption (Nova 1200, Quantachrome) to determine the surface area and particle size. The total specific surface area of 510 m^2/g was obtained using the BET method on the calcined NaY sample.

6.3.2 Dissolution experiments.

Four series of solutions each at different pH were prepared for the study of nanocrystalline NaY stability. The experiment was conducted at 60 ^{o}C in an aqueous solution with pH = 7.4, and at room temperature in aqueous solutions with pH = 4, 2 and 1. Phosphate buffer solutions (0.1 M) were used for preparation of the pH 7.4 and 4 solutions, while hydrochloric acid was used for preparation of pH 2 and 1 solutions. 250 mg of parent zeolite sample was placed in a polypropylene tube, 40 mL of solution was added and the resulting suspension was stirred. A separate suspension was used for each pH and time value. For the dissolution studies performed at 60°C, the tubes were removed from an oil bath after 1, 2, 4, 6 and 24 hours and cooled down in an ice bath. The suspensions were centrifuged for 15 minutes at 14000 rpm (20817 x g) to separate the solids from the supernatants. The supernatants were then additionally centrifuged for 40 minutes at 14000 rpm (20817 x g) in order to remove any traces of solid.

6.3.3 Instrumentation.

Powder X-ray diffraction patterns (Siemens D5000 X-ray diffractometer with Cu Kα and nickel filter) were collected in two different modes. A broad range pattern (5 to 55 2θ with 0.04 step size, 1 s/step) was collected for the parent zeolite to confirm the crystal phase. Narrow range patterns were collected from 2θ = 23-24 with a 0.01 2θ step size, 10 s/step. After a background correction, the peak at 2θ = 23.7 was integrated to calculate the relative crystallinity (RC) of the samples. The narrow range patterns were collected three times for each sample in order to calculate the average value of the relative crystallinity.

Elemental composition of the solids and supernatants was determined by inductively coupled plasma / optical emission spectroscopy (Varian 720-ES). The solids were prepared for analysis in the following manner: 10 mg of zeolite powder was placed in a plastic tube. 1.6 mL of 70:30 HCl : HF solution was added to the tube and the

suspension was sonicated for 15 minutes until all of the solid was completely dissolved. Then, 0.6 mL of concentrated nitric acid and 6 mL of 5% boric acid solutions were added, and the total volume was adjusted to 10 mL with DI water.

A 300 MHz wide bore magnet spectrometer (Varian) with a TecMag Discovery Console was used to record ^{27}Al magic angle spinning nuclear magnetic resonance (MAS NMR). The magnetic field was 6.9 T and the Larmor frequency was 78.172 MHz. 70 mg of powder was loaded in a 4mm zirconia rotor and spun in a Chemagnetics pencil probe at 12 kHz. The spectra were acquired with 512 scans and 3s pulse delays. Additionally, ^{27}Al MAS NMR spectra were recorded for select samples on a Varian-Oxford Inova 63 mm wide bore 900 MHz NMR spectrometer. The main magnetic field was 21.1 T, and the corresponding Larmor frequency was 226.49 MHz. 40mg of sample was placed in a 3.2mm zirconia rotor and spun at 16 kHz. Samples were referenced to $Al(NO_3)_3$ dissolved in aqueous solution.

For TEM imaging (JEOL JEM-1230 Transmission Electron Microscope), a drop of dilute sample suspension in methanol was placed on a holey carbon film (Ted Pella) and dried at room temperature prior to the measurement.

Full XPS (KratosAxis Ultra XPS) instrumental setup can be found elsewhere.[237] Briefly, the surface analysis chamber is equipped with monochromatic radiation at 1486.6 eV from an aluminum K_α source using a 500 mm Rowland circle silicon single crystal monochromator. The X-ray gun was operated using a 15 mA emission current at an accelerating voltage of 15 kV. Low energy electrons were used for charge compensation to neutralize the sample. Survey scans were collected using the following instrument parameters: energy scan range of 1200 to -5 eV; pass energy of 160 eV; step size of 1 eV; dwell time of 200 ms and an X-ray spot size of 700×300 μm. A Shirley-type background was subtracted from each spectrum to account for inelastically scattered electrons that contribute to the broad background. CasaXPS software was used to process the XPS data. Transmission corrected relative sensitivity factor (RSF) values

from the Kratos library were used for elemental quantification. Three spectra were acquired on the same sample in different locations to obtain experimental error. All quantification was performed in terms of atomic percent.

6.4 Results and Discussion

6.4.1 Crystallinity and crystal morphology.

The presence of the FAU phase in the parent zeolite sample was confirmed by powder X-ray diffraction (XRD). A representative XRD powder pattern of the parent nanocrystalline NaY (66 nm) is shown in Figure 53. The powder XRD patterns were also obtained for the solids remaining after the dissolution experiments and the relative crystallinity of each sample was determined by integration of the range from 2θ = 23-24°. The narrow range pattern (2θ = 23-24°) that was used for the relative crystallinity calculations is shown in the inset for representative NaY samples treated at pH=7.4, 4, 2, and 1 for 24 h.

The crystallinity of the zeolite samples was determined relative to the parent NaY sample, whose relative crystallinity (RC) was assumed to be 100%. It was found that a major change in sample crystallinity occurs during the first hour of treatment for all pH conditions (Figure 54). The RC of samples that were treated in pH 7.4, 4 and 2 solutions for 1 hour drops to 70%, 82% and 46% respectively. Further treatment did not have a major effect on RC of these samples. For nanocrystalline NaY zeolite treated at pH 1, the RC decreased to 0% after 1 hour indicating complete loss of the FAU crystal structure.

The series of samples treated at pH 4 showed an interesting evolution in the RC with time. The value of the RC gradually decreased over the 24 hour time period. Still, the first hour of treatment contributed to almost 20% of crystallinity loss, while the next 23 hours contributed to an additional 20% loss of crystallinity (for a total 40% of

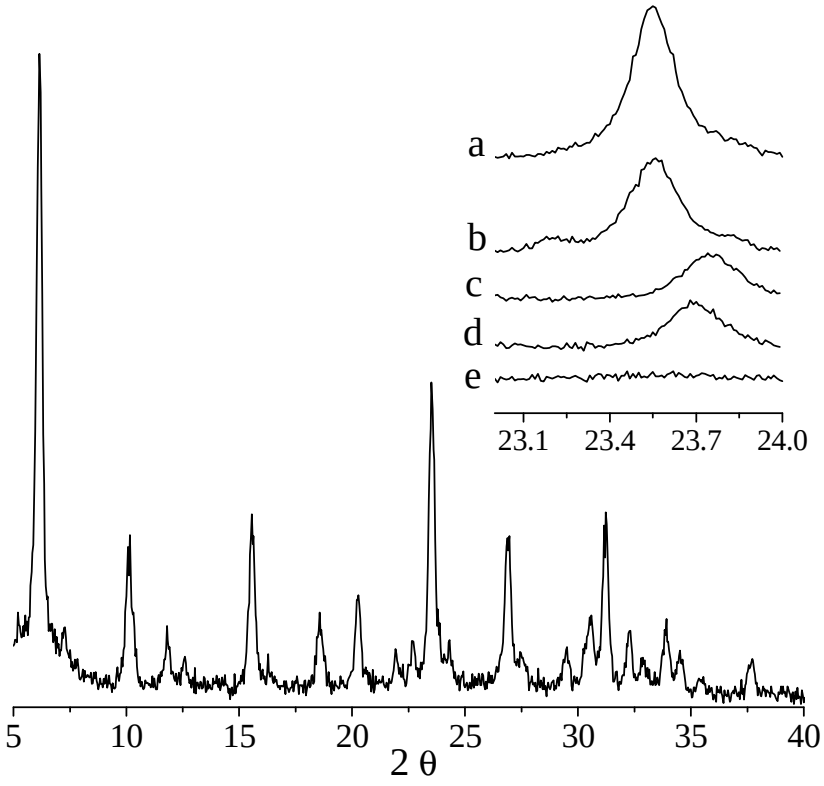

Figure 53. Representative powder x-ray diffraction pattern of parent NaY zeolite. The inset shows the evolution of the reflection at $2\theta = 23.7$ in the a) parent zeolite that was treated for 24 h. at pH values of: b) 7.4, c) 4, d) 2 and e) 1.

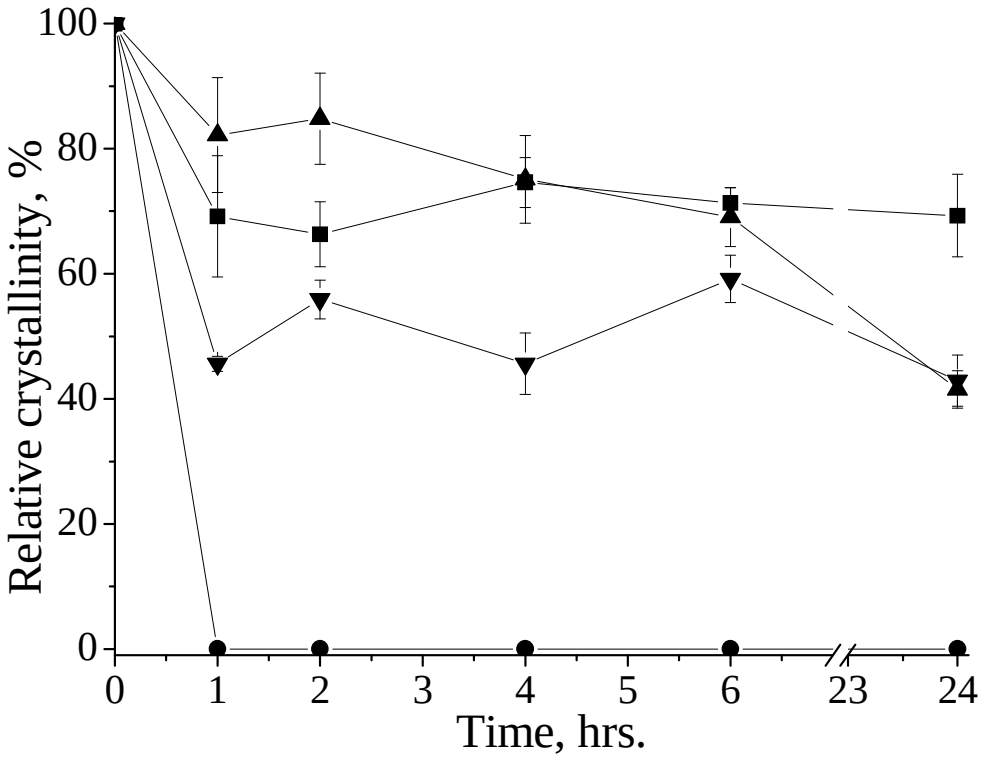

Figure 54. A plot of relative crystallinity of samples vs. treatment time at pH 7.4 (■), 4 (▲), 2 (▼), and 1 (●).

crystallinity loss). This pattern of RC change under mild pH conditions suggests that there might be a small number of reactive sites on the surface of NaY nanocrystals that are quickly dissolved when a sample is placed in an aqueous medium. Stability of the major part of the samples remains highly dependent on the acidity of the reaction medium for a given particle size. For example, the sample treated at pH=7.4 retained ~80% of the initial crystallinity after treatment at 60°C for 24 h while the samples treated at pH=4 and 2 retained about 50% of the crystallinity after 24 h.

The scope of the transmission electron microscopy (TEM) experiment was to visualize the changes occurring in the zeolite framework during the dissolution process. Three samples were selected for TEM imaging. An untreated sample and samples treated pH 7.4 and 1 were chosen as representative, providing the largest contrast between two extreme conditions of dissolution. Particle size and standard deviation of the zeolite nanocrystals were calculated by measuring the size of 100 randomly chosen particles. The histogram of particle sizes is shown in Figure 55. The standard deviation from the average particle size was 13 nm in all cases.

A TEM image of the parent zeolite (Figure 55A) shows cubic particles characteristic of NaY zeolite. The particles have an average size of 66 nm. Particles treated at pH 7.4 for one hour are nearly identical to the parent zeolite (Figure 55B) and no sign of framework dissolution was observed. The average particle size was 64 nm (Figure 56), which was very close to the average size of the parent zeolite. Additional evidence for the stability of the crystal structure at pH 7.4 was provided by the presence of lattice fringes observed for select particles at higher magnification (Figure 55C).

A completely different image is observed in case of nanocrystalline NaY treated at pH 1 for one hour (Figure 55D). The particles' edges are rough, and significant leaching of the framework is clearly seen in the TEM image. There is a pattern of lighter and darker areas in the particles. Lighter spots denote the areas with excessive loss of material, while darker areas represent parts of the zeolite that weren't dissolved. No

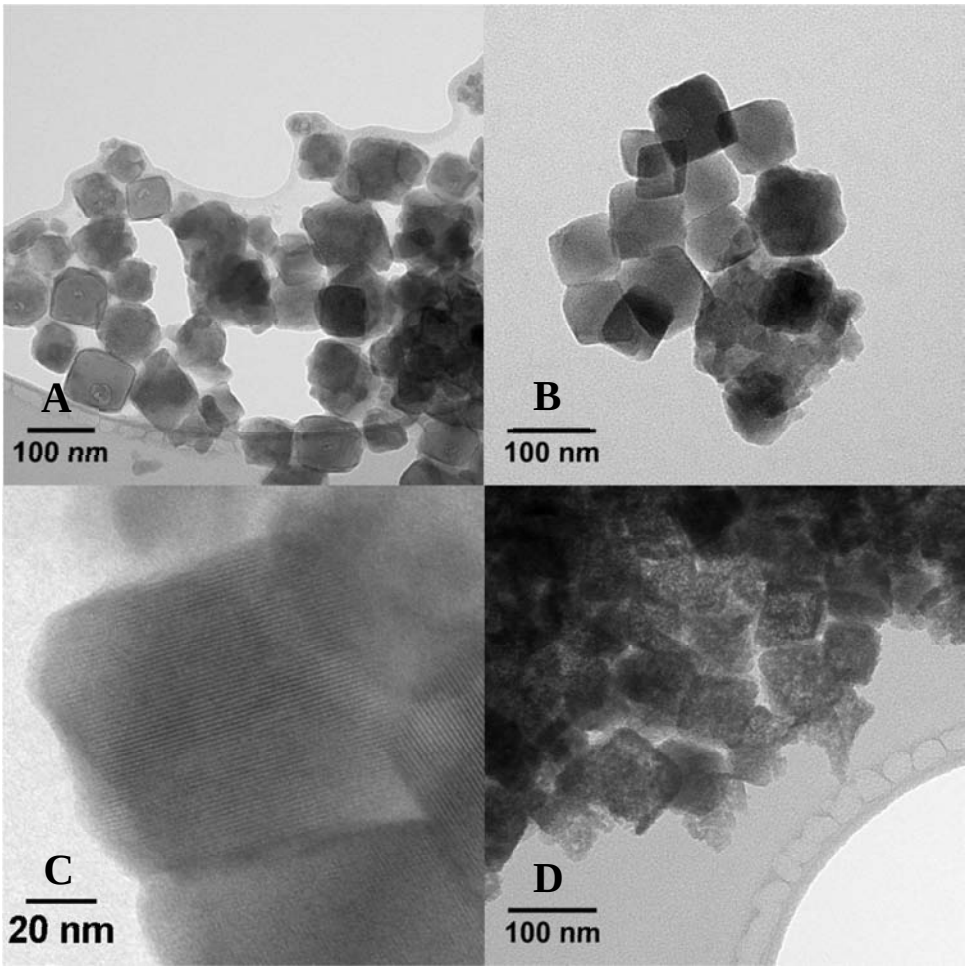

Figure 55. TEM images of parent zeolite (A), zeolite sample treated at pH 7.4 (B, C) and pH 1 (D) for one hour.

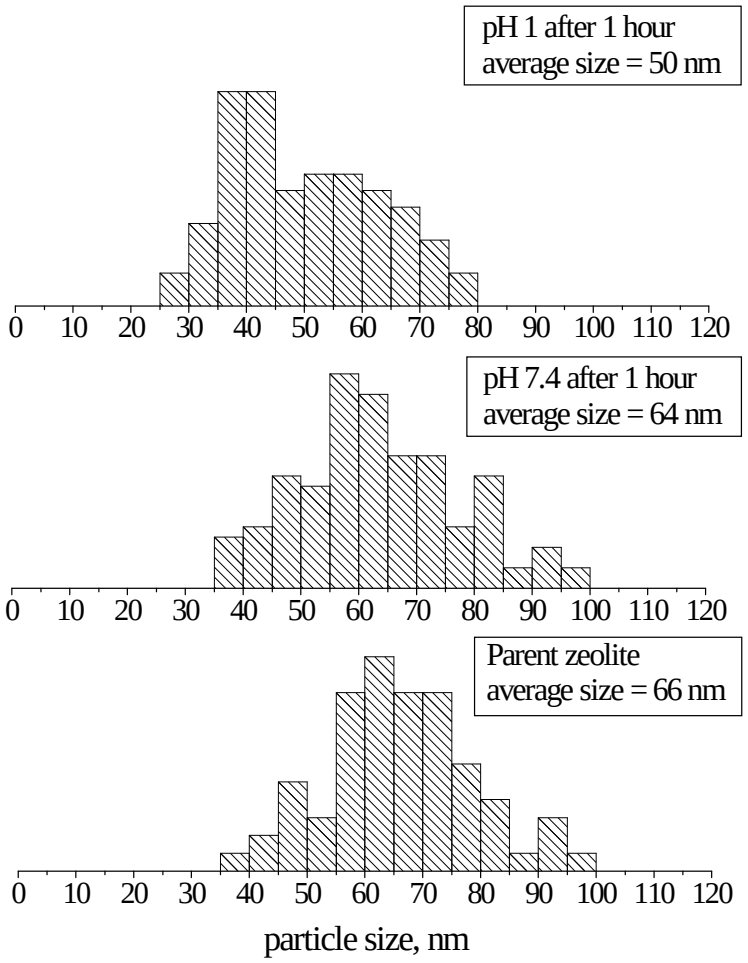

Figure 56. Particle size distribution calculated from TEM images in Figure 3. Particle size and standard deviation of the zeolite nanocrystals were calculated by measuring the size of 100 randomly chosen particles in each image. In each case, the standard deviation was 13 nm.

lattice fringes are observed. Particle size also decreases by 16 nm to an average size of 50 nm, which is another indication of dissolution of the zeolite framework.

6.4.2 Aluminum MAS NMR.

^{27}Al MAS NMR spectra were collected to monitor the coordination state of aluminum in solids before and after treatment. Since ^{27}Al is a quadrupolar nucleus with nuclear spin of 5/2, its solid state NMR spectrum is typically characterized by significant line broadening due to a large quadrupole coupling constant. ^{27}Al MAS spectra were obtained at 6.9 T and then at 21.1 T because the quadrupolar line broadening is inversely dependent on magnetic field strength.

The ^{27}Al MAS NMR spectra (Figure 57A) of the parent NaY obtained on a 300 MHz NMR spectrometer contain two peaks at approximately 60 ppm and -5 ppm that have been assigned to aluminum centers in tetrahedral (T_d) and octahedral (O_h) coordination respectively.[238] It can be assumed that all of the tetrahedrally coordinated aluminum atoms are in the zeolite framework while the octahedrally coordinated aluminum is generally associated with extra-framework aluminum. A small amount of octahedrally coordinated aluminum in the parent zeolite sample is due to the presence of small amounts of extra-framework aluminum species. The amount of extra-framework aluminum in the parent zeolite constitutes approximately 4% of the total number of aluminum atoms.

When aluminum is leached from the zeolite framework, its coordination state changes from tetrahedral to octahedral. The spectrum of the zeolite sample treated at pH 7.4 for 24 hours shows little difference from the parent zeolite (Figure 57B). As the acidity of the reaction medium increases, the intensity of peak with a chemical shift at approximately 60 ppm decreases dramatically. A slight increase in the signal at ~ -5 ppm is also observed. This observation indicates that in the solids remaining after partial

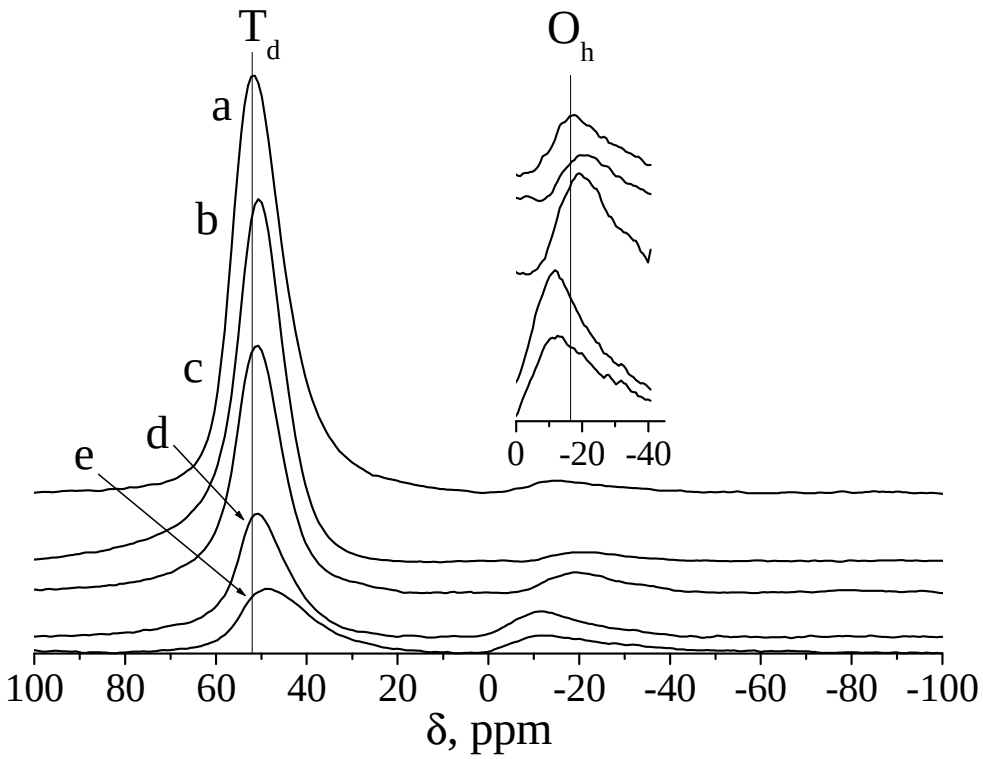

Figure 57. ^{27}Al MAS NMR spectra of parent NaY zeolite (a) and samples treated at pH = 7.4 (b), 4 (c), 2 (d) and 1 (e) for 24 hours.

dissolution, more aluminum is removed from the zeolite framework at lower pH values. There is a significant decrease of the T_d peak intensity in the series of samples, especially at lower pH values. The relatively small increase of O_d peak strength is most likely due to the formation of insoluble aluminum species, in which aluminum has octahedral coordination. A slight upfield shift of O_h peak from -5 ppm to -10 ppm is most likely due to reaction between aluminum cations and hydrophosphate anions resulting in formation of aluminum hydrophosphate. ^{31}P MAS NMR supports the presence of an aluminum hydrophosphate in the solids.

The ratio between integrated intensities of tetrahedrally to octahedrally coordinated aluminum $I(T_d)/I(O_h)$ was chosen as a reliable parameter that reflects the change of aluminum content in the framework, as this value is independent of the sample mass used (Figure 58). Similar to the trends observed in powder XRD patterns, the highest change of $I(T_d)/I(O_h)$ occurred during the first hour of the experiment and subsequently changed very little after. Figure 6 shows that at pH 7.4 there is a small decrease of the ratio from 25.6 to 24.3. This observation indicates that the majority of aluminum atoms remain in the zeolitic framework and, therefore, that the zeolite is stable at pH 7.4. The decrease of pH to 4 is accompanied by a more marked spectral change. $I(T_d)/I(O_h)$ ratio decreases to 10.8. Further increase of the reaction medium acidity results in higher loss of framework aluminum. The $I(T_d)/I(O_h)$ values further decreased to 4.4 and 2.6 at pH 2 and 1 respectively.

^{27}Al MAS NMR spectra of parent 66 nm zeolite and samples treated pH = 7.4, 4, 2 and 1 for 24 hours were also recorded on a 900 MHz Oxford-Varian instrument (Figure 59). The spectra recorded on a high field instrument show features similar so those observed at lower field but with improved resolution. The major tetrahedral aluminum peak at 62 ppm is observed for the parent zeolite sample and treatment of the zeolite sample at pH = 7.4 does not result in any significant changes to this peak. Smaller peaks are also observed at 3.2 and -2.0 ppm and are assigned to octahedrally coordinated

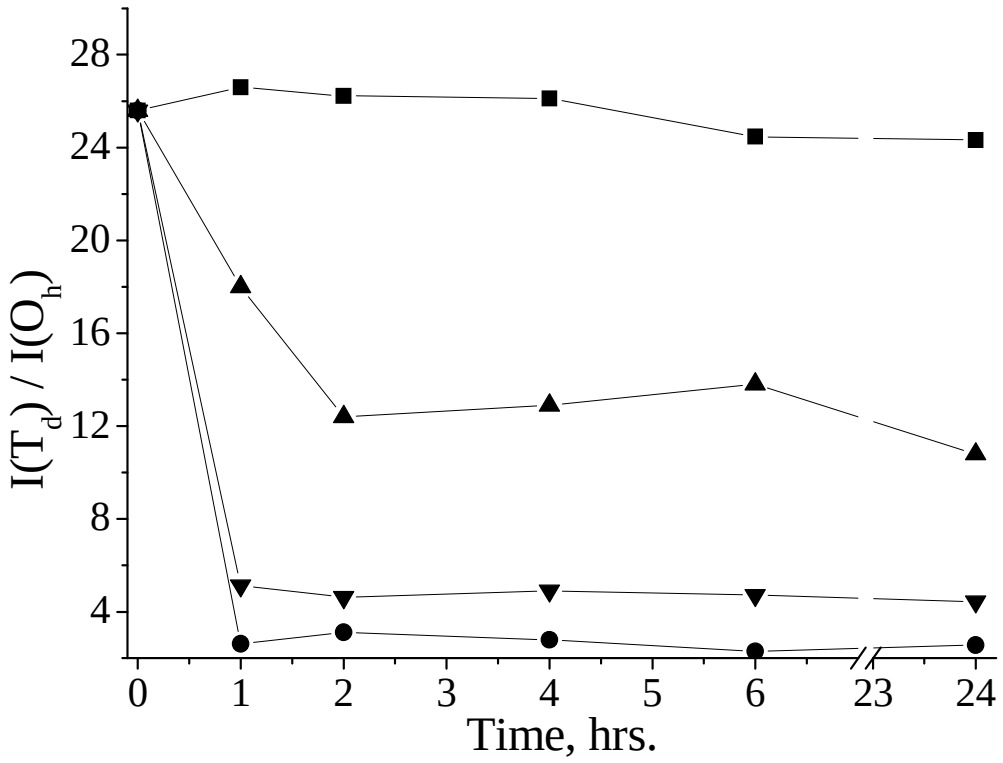

Figure 58. $I(T_d) / I(O_h)$ ratio (from ^{27}Al MAS NMR obtained at 300 MHz) vs. time of zeolite samples treated at pH 7.4 (■), 4 (▲), 2 (▼) and 1 (●).

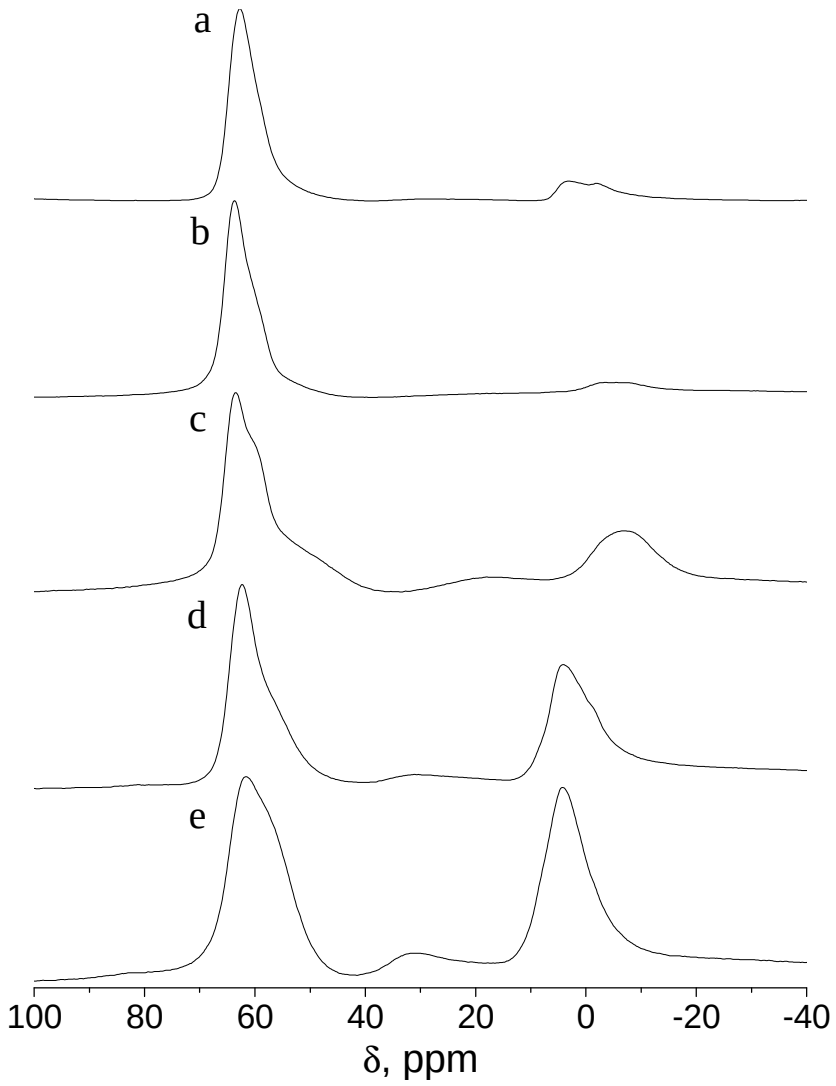

Figure 59. ^{27}Al MAS NMR spectra of parent NaY zeolite (a) and samples treated at pH = 7.4 (b), 4 (c), 2 (d) and 1 (e) for 24 hours.

aluminum. Treatment at pH = 4, 2 and 1 for 24 hours is accompanied by broadening of the peak at 60 ppm and development of a shoulder at ~58 ppm. This indicates the formation of another tetrahedral site that is distorted and the intensity of this site increases at lower pH values.[239] A marked increase in the spectral intensity at ~5 ppm is observed at lower pH values indicating the formation of octahedrally coordinated aluminum just as was observed at lower magnetic field.

One feature absent in the spectra recorded at the lower field is a peak at ~30 ppm. This peak can be assigned to pentacoordinated or disordered tetrahedral coordinated extra-framework species, which are typically formed during hydrothermal treatment of zeolites.[239, 240] This peak is particularly evident in the spectrum obtained for the sample treated at pH=1 for 24 hours (Figure 59e). Further work is in progress to obtain MQMAS spectra for these samples so that more detailed information about the aluminum sites can be obtained.

6.4.3 Silicon to aluminum ratio of solids and supernatants in dissolution experiments.

ICP-OES analysis was performed on solid samples before and after dissolution treatment as well as on supernatants of the solutions used in the study. The variation in the silicon to aluminum ratio (Si/Al) in solid samples was of particular interest and was used to determine which element is preferentially removed from the zeolite framework under different pH conditions. ICP-OES analysis of the supernatants allowed quantification of the amount of silicon and aluminum released from the zeolite framework upon dissolution.

Based on the elemental analysis of supernatants, the four series of NaY samples fall in two major categories (Table 9). The samples treated at pH 7.4 and 4 release low amounts of aluminum (6 to 25 ppm/g) and moderate amounts of silicon into solution: 145 to 235 ppm/g at pH 7.4 and 189 to 497 ppm/g pH 4. However, ^{27}Al MAS NMR of the

Table 9. Concentration of Si and Al in the supernatants after NaY dissolution measured by ICP/OES.

Treatment time, hrs	pH = 7.4		pH = 4		pH = 2		pH = 1	
	Al, ppm/g	Si, ppm/g	Al, ppm/g	Si, ppm/g	Al, ppm/g	Si, ppm/g	Al, ppm/g	Si, ppm/g
1	21.0 (0.3)	235 (3)	8.2 (0.2)	189 (9)	306 (7)	355 (13)	2651 (16)	3789 (23)
2	24.0 (0.2)	195 (3)	7.80 (0.01)	246. (0.4)	264 (5)	329 (6)	2833 (39)	3700 (71)
4	16.0 (0.3)	145 (2)	7.90 (0.01)	318 (2)	344 (4)	371 (5)	2945 (48)	3809 (75)
6	18.00 (0.04)	160.0 (0.3)	6.40 (0.01)	315.0 (0.2)	247 (4)	300 (4)	2489 (30)	3075 (27)
24	17.00 (0.03)	168.0 (0.8)	7.00 (0.02)	497 (2)	488 (4)	443 (3)	2661 (19)	2631 (19)

[a] Standard deviations from 3 measurements are provided in parenthesis.

solids suggests that two different explanations are required to explain the low amount of aluminum detected in these solutions at different pH values. At pH 7.4, most of the aluminum atoms remain in the framework as suggested by the similarity of ^{27}Al MAS NMR spectra of the two solid samples and discussed in the previous section. At pH 4, aluminum cations are released into the solution and then react with phosphate anions to form insoluble phosphate salt that precipitates from the supernatant. The presence of aluminum phosphate salt in the pH 4 series of NaY zeolite samples contributes to the low Si/Al ratio detected in solids.

The second category of NaY samples was treated at pH 2 and 1. These two series of samples are characterized by high amounts of both silicon and aluminum in solution. Notably, at pH=1, the aluminum concentration is >2500 ppm/g and the silicon concentration is >2600 ppm/g indicating a large extent of dissolution. 7.1% of the starting sample mass is removed at pH 2, and 62% is removed at pH 1.

It should also be noted that the % mass loss for each of the samples was also measured. After 24 h, approximately 2%, 4%, 10% and 55% of the zeolite mass was lost for pH=7.4, 4, 2, and 1, respectively. From this data, it is clear that significant zeolite NaY dissolution occurs at pH=1 which is consistent with the observed loss of silicon and aluminum as measured by ICP/OES.

The change of Si-to-Al ratio in the solids (Table 10) was measured by both ICP/OES and by XPS. The ICP/OES results provide a measurement of the bulk Si/Al and the XPS provides a measurement of the surface Si/Al (penetration depth of ~1 nm). The bulk Si/Al ratio from ICP/OES increased from 1.74 in the parent NaY to 2.42 after treatment at pH 1 for 24 h. This suggests that stoichiometrically more aluminum is removed from the framework than silicon. Different results were obtained at pH 7.4 and 4 in which slight decreases in Si/Al to 1.60 and 1.32, respectively, were observed. This is attributed to partial dissolution of the zeolite and subsequent precipitation of aluminum phosphate on the zeolite as suggested by the P-31 MAS NMR results.

Table 10. Si-to-Al ratio in parent NaY and remaining solid samples after dissolution treatment.

Treatment time, h.	pH = 7.4	pH = 4	pH = 2	pH = 1
ICP/OES				
parent[a]	1.74 (0.03)	1.74 (0.03)	1.74 (0.03)	1.74 (0.03)
1[a]	1.66 (0.09)	1.6 (0.2)	2.0 (0.2)	2.8 (0.3)
2[a]	1.6 (0.2)	1.44 (0.01)	1.7 (0.2)	2.3 (0.2)
4[a]	1.58 (0.05)	1.41 (0.03)	1.77 (0.03)	2.40 (0.05)
6[a]	1.53 (0.06)	1.43 (0.05)	1.74 (0.04)	2.43 (0.03)
24[a]	1.60 (0.08)	1.32 (0.09)	1.80 (0.02)	2.42(0.03)
XPS				
parent[b]	2.0	--	--	--
24[b]	1.4	1.3	2.6	3.0

[a] Standard deviations from 3 ICP/OES measurements are provided in parenthesis.

[b] Si/Al measured by XPS. Estimated %error of 5%.

Similar trends were observed by XPS (Table 10) in which the Si/Al ratio relative to the parent decreased after treatments at pH=7.4 and 4 and increased after treatments at pH=1 and 2. The main differences between the ICP and XPS measurements are at the low pH values where the Si/Al measured by XPS is systematically higher than the Si/Al measured by ICP/OES. This suggests that the aluminum depletion is greater at the surface of the zeolite relative to the bulk.

ICP analysis of solids after treatment revealed that the trend in Si-to-Al ratio upon treatment with hydrochloric acid solutions is similar to what was observed for large NaY zeolite crystals previously.[235] Hartman and Fogler suggested that the dissolution behavior in zeolites is governed by the Si/Al. They concluded that at Si/Al ratios greater than 1, aluminum is preferentially removed from the zeolite framework under acidic conditions. They showed that the Si/Al ratio in the solid samples treated with 8M HCl at 5.4°C increased from 2.09 to ~10 in case of analcime zeolite and from 2.56 to several hundred in case of NaY zeolite. However, for zeolite 4A with Si/Al=1.06, stoichiometric dissolution was observed.

In our study of nanocrystalline NaY treated at pH 1, the change in Si/Al ratio was rather modest (Si/Al=1.74 to 2.42 after 24 h at pH 1) indicating that the nanocrystalline NaY used in our study exhibits behavior intermediate between zeolite 4A and NaY which is not unreasonable given that the Si/Al of our NaY is 1.74 which is between the Si/Al of the 4A (Si/Al=1.06) and NaY (Si/Al=2.56) samples used by Hartman and Folger. There are several differences between our study and Hartman and Fogler's that should be noted. In our study, 64 nm NaY crystals were used and for the dissolution studies, the pH was adjusted with HCl to 2 and 1 and with phosphate buffer for pH 7.4 and 4. Hartman and Fogler used 8M HCl at 5.4°C for the dissolution studies. The smaller crystal size will increase the external crystal surface of the zeolites. A systematic study of the effect of crystal size on framework stability is in progress.

6.4.4 Effect of pH on nanocrystalline NaY dissolution.

At pH=7.4 and 60°C, conditions that were chosen to represent a typical biological system, nanocrystalline NaY with a size of 66 nm was quite stable for 24 h. The structural integrity of the zeolite framework was retained to a large extent. The framework of NaY is shown in Figure 60a. A moderate decrease in the relative crystallinity was observed by powder XRD, but very little change in the TEM images was observed. The tetrahedral to octahedral aluminum ratio measured by ^{27}Al NMR remained approximately constant. These results suggest that nanocrystalline NaY with a size of 66 nm is stable under physiological conditions for at least 1 day indicating that it is feasible to use nanocrystalline zeolites in biomedical applications such as imaging and drug delivery.

At the intermediate pH values investigated (pH 4 and 2), partial degradation of the zeolite framework was observed resulting in a loss of approximately 50% of the crystallinity as measured by powder XRD and a decrease in the intensity of the tetrahedral aluminum peak in the NMR spectra which also coincided with an increase in dissolved aluminum as measured by ICP. At pH=4, formation of a phosphate-containing species, most likely an aluminum phosphate on the surface was confirmed by ^{31}P NMR. The Si/Al ratio measured by XPS decreases after treatment at pH=7 and 4 which is consistent with enrichment of aluminum on the surface. This supports the idea of dissolution followed by precipitation of an aluminum phosphate species as depicted in Figure 60b.

At the lowest pH investigated, the zeolite framework completely degraded in 1 h. Powder XRD showed a complete loss of crystallinity, which was supported by the TEM images which indicated a loss of lattice fringes and a decrease in average crystal size. The Si-to-Al ratio of the solid remaining after treatment at pH=1 showed a moderate increase in Si-to-Al ratio from 1.74 for the parent to 2.42 suggesting that more aluminum was removed from the zeolite framework relative to silicon. The loss of crystallinity and

increase in Si/Al ratio is illustrated in Figure 60c. The Si/Al increased slightly more as analyzed by XPS suggesting that the amorphous material present after dissolution has a slightly higher Si/Al on the surface (Si/Al=3.0) relative to the bulk material (Si/Al=2.4). The results were supported by increasing amounts of dissolved silicon and aluminum as measured by ICP and a substantial loss of tetrahedral aluminum as monitored by ^{27}Al MAS NMR spectroscopy. The results observed for the lowest pH values in this study are consistent with what has been observed previously by Hartman and Fogler in which preferential loss of aluminum from zeolite Y was observed during acid treatments.[235]

6.5 Conclusions

Framework stability of nanocrystalline NaY zeolite in aqueous solutions was investigated under different pH conditions and for time periods extending to 24 hours. The dissolution was investigated using powder XRD, TEM, ICP/OES and ^{27}Al MAS NMR. It was found that the major change to the sample elemental composition, surface area and crystallinity occurred during the first hour of the experiment. Further treatment did not have a significant effect on the zeolite properties. The pH of the medium has a strong effect on the stability of nanocrystalline NaY samples. NaY nanocrystals were found to be relatively stable at pH 7.4 and T=60°C for 24 hours and the amount of silicon and aluminum released into the reaction solution was small. NaY framework stability diminished as the acidity of the medium increased. NaY nanocrystals were unstable at pH 1 and complete loss of crystallinity was observed by powder XRD and TEM. ^{27}Al MAS NMR provided direct evidence for the loss of tetrahedral aluminum sites and the growth of octahedral aluminum species. XPS and ICP/OES results indicate that aluminum was removed from the framework nonstoichiometrically causing an increase in Si/Al of the solid material after treatment at pH=1. Further studies are in progress on nanocrystalline zeolites with different sizes and with surface functionalization. This work has implications for future biomedical applications of these materials. The results were

published in Langmuir, 2010, volume 26, pages 6695-6701, and authored by Petushkov, Freeman and Larsen.

a) Parent NaY

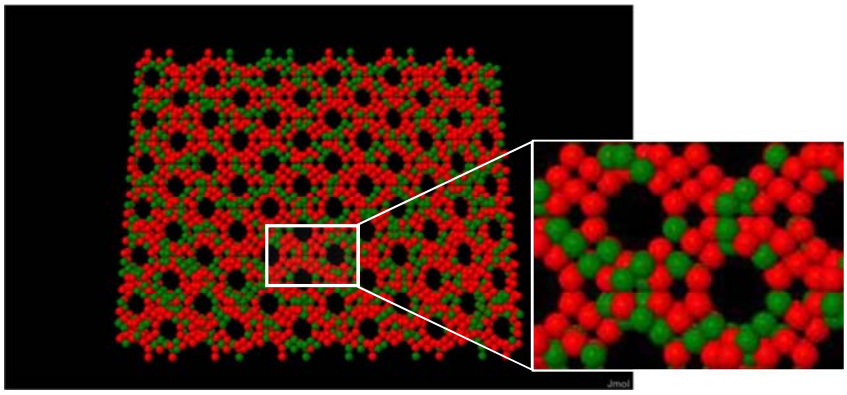

b) NaY treated at pH = 4

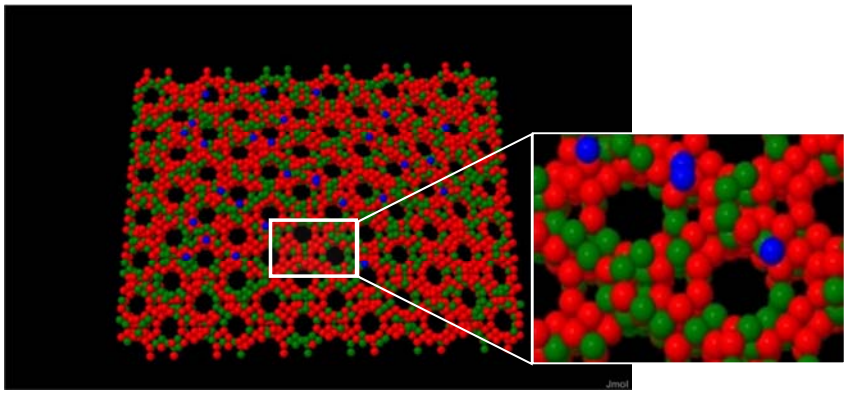

c) NaY treated at pH = 1

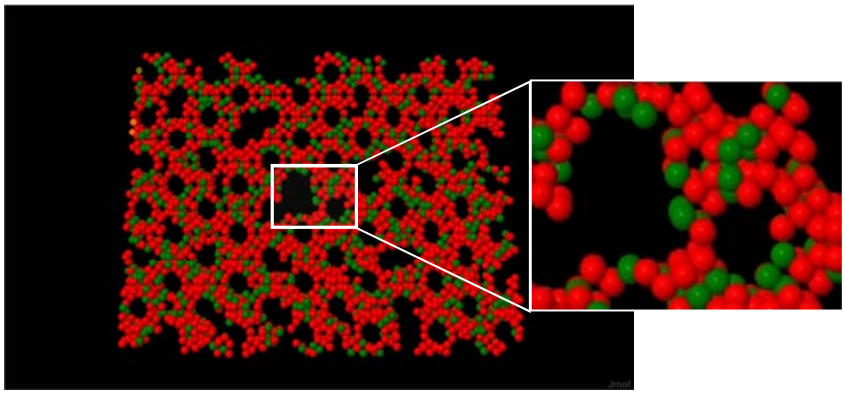

Figure 60. Schematic representation of the NaY(Si/Al=1.74) framework structure after treatment at various pH values: a) parent NaY, b) NaY treated at pH=4 for 24 h. and c) pH=1 for 24 h. The red represents silicon atoms, green represents aluminum atoms and blue phosphorous.

CHAPTER 7. CONCLUSIONS AND FUTURE WORK

7.1 Conclusions

This thesis describes several studies involving nanocrystalline and mesoporous zeolites. There are two major parts in the thesis. The first part is synthesis and characterization of mesoporous zeolites with two different frameworks, which were then used for preparation of catalytically active materials containing various transition metals. The study of mesoporous zeolites synthesis has shown that the degree of mesoporosity can be controlled by adjusting the size of nanocrystals assembled in aggregates. Multiple factors, such as the concentration of the reaction mixture, pH, temperature, and synthesis time affect the particle size and the degree of their aggregation in mesoporous composites. Different zeolites require a specific set of reaction conditions in order to achieve the desired parameters, and this difference has been shown for ZSM-5 and β zeolites. The starting pH value had a strong effect on the crystallization and the mesoporosity of ZSM-5 zeolite, while the increasing the concentration of the reaction mixture turned out to be an important parameter in achieving formation of mesoporous β zeolite.

The mesoporous ZSM-5 and β zeolites as well as nanocrystalline NaY zeolite were ion-exchanged with a series of transition metal ions. Single- and bimetal-exchanged zeolite samples have been produced and structural properties of the materials have been studied. It has been shown that the surface area and pore volume characteristics of the metal-exchange zeolites are similar to those of parent zeolite samples, which indicates that the zeolite framework remains intact after the ion-exchange. In the case of bimetal-exchanged zeolites, the difference between the metal-ion affinities to the exchange sites on the zeolite surface resulted in preferred binding of one of the metal ions. In order to achieve the desired composition, the ratio between the metal ions in the ion-exchanged solutions had to be adjusted accordingly.

The second part of the thesis describes the study of nanocrystalline Silicalite-1 (MFI framework) cytotoxic activity as a function of multiple parameters, such as the particle size, type of surface functional groups, concentration, and the cell line type. The study has revealed a complex dependence of cytotoxicity on these parameters. The larger zeolite particles can be internalized only by specific cells, e.g. macrophage cells. This resulted in different cytotoxicity of the particles with the same size depending on the cell type. Increasing the concentration of smaller zeolite nanocrystals typically led to higher cytotoxicity, which was not functional group dependent, and was probably due to the higher uptake of these crystals by the cells. Higher toxicity of larger Silicalite-1 nanocrystals functionalized with carboxypropyl groups may have resulted from enhanced generation of reactive oxygen species on the zeolite surface, which was confirmed by EPR.

The study of nanocrystalline NaY zeolite framework stability is relevant to the potential biomedical applications of this large pore zeolite. The zeolite stability has been studied in the range of pH values between 7.4 and 1, which are typical for human body. NaY zeolite was found to be stable at near neutral pH, and its stability decreases at lower pH values, when a larger fraction of the zeolite framework is dissolved. These results mean that while the zeolite would not be stable in the upper gastrointestinal tract, direct injection into the blood stream or tissue would not degrade the nanocrystals.

7.2 Future work

Formation of mesoporous aggregates of zeolites in a single step process is economically attractive, as it decreases the amount of time and labor required for obtaining the product. The use of single template for the synthesis is another important factor that would further decrease of the production costs. Improvement of mesoporous ZSM-5 and zeolite β synthesis would include the increase of the aggregate size while maintaining the mesopore volume and mesopore surface area at the same level, especially

in the case of β zeolite. Several strategies that can be used for improving the properties of zeolite β are the further change of the water to silica ratio in the reaction mixtures, use of a larger amount of alkaline cations in the synthesis gel, and change of the stirring rate during the synthesis.

Nanocrystalline zeolites were ion-exchanged under conditions similar to those used in the case of conventional large zeolite crystals. The ion-exchange process can be optimized by studying the temperature and time required for the metal ion loading. Because of the smaller crystal size, the ion-exchange process can be expected to proceed faster and at a lower temperature than for large zeolite crystals. Wet impregnation technique can also be used for bi-metal loading, as it provides and easier control over ratio between the metal ions.

Biomedical applications of zeolites require their surface modification with different organic functional groups for targeted delivery to specific cells or sensing. Zeolites modified with such organic groups may have a different stability in comparison with non-functionalized zeolites. Furthermore, stability of organic groups on the surface is a separate subject that needs to be investigated. Accurate quantification of the organic group concentration on the zeolite surface and its change under relevant conditions can be studied by using multiple techniques. These techniques include but are not limited to thermogravimetric analysis coupled with IR, mass spectrometry or gas chromatography as well as high performance liquid chromatography. Solution NMR can be used for monitoring the structural changes in the organic groups.

REFERENCES

1. 1. Ji, Z.; Warzywoda, J.; Sacco, A., Jr. *Microporous and Mesoporous Materials* **2008**, *109*, 1-11.

2. Phonthammachai, N.; Krissanasaeranee, M.; Gulari, E.; Jamieson, A. M.; Wongkasemjit, S. *Materials Chemistry and Physics* **2006**, *97*, 458-467.

3. Krzhizhanovskaya, M. G.; Bubnova, R. S.; Depmeier, W.; Filatov, S. K.; Ugolkov, V. L. *Microporous and Mesoporous Materials* **2008**, *116*, 569-574.

4. Elomari, S.; Burton, A. W.; Ong, K.; Pradhan, A. R.; Chan, I. Y. *Chemistry of Materials* **2007**, *19*, 5485-5492.

5. Arean, O. C.; Palomino, T. G.; Geobaldo, F.; Zecchina, A. *Journal of Physical Chemistry* **1996**, *100*, 6678-6690.

6. Dorset, D. L.; Strohmaier, K. G.; Kliewer, C. E.; Corma, A.; Diaz-Cabanas, M. J.; Rey, F.; Gilmore, C. J. *Chemistry of Materials* **2008**, *20*, 5325-5331.

7. Lazar, K. C., A. J.; Fejes, P.; Cejka, J.; Ramaswamy, A. V. *Journal of Radioanalytical and Nuclear Chemistry* **2000**, *246*, 143-148.

8. Tusar, N. N. M., Gregor; Arcon, Iztok; Kaucic, Venceslav; Ghanbari-Siahkali, Afshin; Dwyer, John. . *Microporous and Mesoporous Materials* **2002**, *55*, 203-216.

9. Bennett, J. M.; Dytrych, W. J.; Pluth, J. J.; J. W. Richardson, J.; Smith, J. V. *Zeolites* **1986**, *6*,

10. Masih, D.; Kobayashi, T.; Baba, T. *Chemical Communications* **2007**, 3303.

11. Flanigen, E. M.; Patton, R. L., *Silica polymorph*. 1978: U.S. p. 7.

12. Guth, J. L.; Kessler, H.; Higel, J. M.; Lamblin, J. M.; Patarin, J.; Seive, A.; Chezeau, J. M.; Wey, R. *ACS Symposium Series* **1989**, *398*, 176-195.

13. Sulikowski, B. K., Jacek. *Journal of Physical Chemistry* **1992**, *96*, 5030-5035.

14. Pine, L. A.; Maher, P. J.; Watcher, W. A. *Journal of Catalysis* **1984**, *85*, 466.

15. Li, X.; Li, C.; Zhang, J.; Yang, C.; Shan, H. *Journal of Natural Gas Chemistry* **2007**, *16*, 92-99.

16. Subbiah, A. C., Byong K.; Blint, Richard J.; Gujar, Amit; Price, Geoffrey L.; Yie, Jae E. *Applied Catalysis, B: Environmental* **2003**, *42*, 155-178.

17. Guisnet, M. *Methods and Reagents for Green Chemistry* **2007**, 231-249.

18. Larsen, S. C. *Journal of Physical Chemistry C* **2007**, *111*, 18464-18474.

19. Sakthivel, A.; Iida, A.; Komura, K.; Sugi, Y.; Chary, K. *Microporous and Mesoporous Materials* **2009**, *119*, 322-330.

20. Hassani, S. S.; Salehirad, F.; Aghabozorg, H. R.; Sobat, Z. *Crystal Research and Technology* **2010**, *45*, 183-187.

21. Yang, H. C., Honglin; Du, Hongbin; Hawkins, Randall; Craig, Fairbridge; Ring, Zbigniew; Omotoso, Oladipo; Munoz, Vicente; Mikula, Randy. . *Microporous and Mesoporous Materials* **2008**, *117*, 33-40.

22. Song, W.; Grassian, V. H.; Larsen, S. C. *Chemical Communications* **2005**, 2951.

23. Kecht, J.; Mihailova, B.; Karaghiosoff, K.; Mintova, S.; T., B. *Langmuir* **2004**, *20*, 5271-5276.

24. Tago, T. A., Daichi; Iwakai, Kazuyuki; Masuda, Takao. *Topics in Catalysis* **2009**, *52*, 865-871.

25. Mohamed, R.; Fouad, O.; Ismail, A.; Ibrahim, I. *Materials Letters* **2005**, *59*, 3441-3444.

26. Hsu, C.-Y.; Chiang, A. S. T.; Selvin, R.; Thompson, R. W. *Journal of Physical Chemistry B* **2005**, *109*, 18804-18814.

27. Song, W.; Justice, R. E.; Jones, C. A.; Grassian, V. H.; Larsen, S. C. *Langmuir* **2004**, *20*, 8301-8306.

28. Morales-Pacheco, P.; Alvarez-Ramirez, F.; Del Angel, P.; Bucio, L.; Dominguez, J. M. *Journal of Physical Chemistry C* **2007**, *111*, 2368-2378.

29. Camblor, M. A.; Corma, A.; Valencia, S. *Microporous and Mesoporous Materials* **1998**, *25*, 59–74.

30. Hould, N. D.; Lobo, R. F. *Chemistry of Materials* **2008**, *20*, 5807-5815.

31. Kuechl, D. E. B., Annabelle I.; Knight, Lisa M.; Abrevaya, Hayim; Wilson, Stephen T.; Sinkler, Wharton; Mezza, Thomas M.; Willis, Richard R. *Microporous and Mesoporous Materials* **2009**, *127*, 104-118.

32. Song, W.; Grassian, V. H.; Larsen, S. C. *Chemical Communications* **2005**, 2951.

33. Schoeman, B. J.; J.;, S.; Otterstedt, J.-E. *Zeolites* **1994**, *14*, 110-116.

34. Li, Q.; Creaser, D.; Sterte, J. *Chemistry of Materials* **2002**, *14*, 1319-1324.

35. Cundy, C. S.; Lowe, B. M.; Sinclair, D. M. *Journal of Crystal Growth* **1990**, *100*, 189.

36. Cundy, C. S.; Henty, M. S.; Plaisted, R. J. *Zeolites* **1995**, *15*, 342-.

37. Covarrubias, C.; Quijada, R.; Rojas, R. *Microporous and Mesoporous Materials* **2008**, *117*, 118-125.

38. Jung, K. T.; Shul, Y. G. *Chemistry of Materials* **1997**, *9*, 420-422.

39. Ismagilov, Z. R.; Yashnik, S. A.; Startsev, A. N.; Boronin, A. I.; Stadnichenko, A. I.; Kriventsov, V. V.; Kasztelan, S.; Guillaume, D.; Makkee, M.; Moulijn, J. A. *Catalysis Today* **2009**, *144*, 235-250.

40. Takahashi, A.; Yang, R. T.; Munson, C. L.; Chinn, D. *Langmuir* **2001**, *17*, 8405-8413.

41. Prasanth, K. P. P., Renjith S.; Bajaj, H. C.; Jasra, R. V.; Chung, H. D.; Kim, T. H.; Song, S. D. *International Journal of Hydrogen Energy* **2008**, *33*, 735-745.

42. Fernandes, D. R.; Rosenbach, N.; Mota, C. J. A. *Applied Catalysis, A: General* **2009**, *367*, 108-112.

43. Eichelbaum, M.; Siemer, A. B.; Farrauto, R. J.; Castaldi, M. J. *Applied Catalysis B: Environmental* **2010**, *97*, 98-107.

44. Fedeyko, J. M.; Chen, B.; Chen, H.-Y. *Catalysis Today* **2010**, *151*, 231-236.

45. Ismagilov, Z. R.; Yashnik, S. A.; Startsev, A. N.; Boronin, A. I.; Stadnichenko, A. I.; Kriventsov, V. V.; Kasztelan, S.; Guillaume, D.; Makkee, M.; Moulijn, J. A. *Catalysis Today* **2009**, *144*, 235-250.

46. Takahashi, A. Y., Ralph T.; Munson, Curtis L.; Chinn, Daniel. . *Langmuir* **2001**, *17*, 8405-8413.

47. Eichelbaum, M.; Siemer, A. B.; Farrauto, R. J.; Castaldi, M. J. *Applied Catalysis, B: Environmental* **2010**, *97*, 98-107.

48. Vakhmistrov, V. E.; Ponomaryov, A. B.; Shostakovsky, M. V.; Kalinin, V. N.; Solodovnikov, S. P.; Mortikov, E. S. *Inorganic Materials* **2010**, *46*, 978-982.

49. Kraushaar-Czarnetzki, B.; van Hooff, J. H. C., in *Zeolites: facts, figures, future.* , v.S.R.A. Jacobs P. A., Editor. 1989, Elsevier: Amsterdam. p. 1063.

50. Zhang, J.-Z.; Long, M. A.; Howe, R. F. *Catalysis Today* **1998**, *44*, 293-300.

51. Hong, S. B.; Mielczarski, E.; Davis, M. E. *Journal of Catalysis* **1992**, *134*, 349-358.

52. Parvulescu, V. I. C., S.; Palade, P.; Macovei, D.; Teodorescu, C. M.; Filoti, G.; Molina, R.; Poncelet, G.; Wagner, F. E. *Applied Surface Science* **1999**, *141*, 164-176.

53. Kubo, T. A., Hiromichi; Tominaga, Hiroo; Kunugi, Taiseki. *Bulletin of the Chemical Society of Japan* **1972**, *45*, 613-616.

54. Nie, Y.; Jaenicke, S.; Chuah, G.-K. *Chemistry - A European Journal* **2009**, *15*, 1991-1999.

55. Li, J. D., Robert J. *Journal of Physical Chemistry B* **2005**, *109*, 7141-7148.

56. Loiha, S.; Föttinger, K.; Zorn, K.; Klysubun, W.; Rupprechter, G.; Wittayakun, J. *Journal of Industrial and Engineering Chemistry* **2009**, *15*, 819-823.

57. Ren, L. L.; Zhang, T. *Chinese Chemical Letters* **2010**, *21*, 674-677.

58. Campos Roseno, K. T.; Baldanza, M. A. S.; Schmal, M. *Catalysis Letters* **2008**, *124*, 59-67.

59. Tamm, S.; Ingelsten, H. H.; Palmqvist, A. E. C. *Catalysis Letters* **2008**, *123*, 233-238.

60. Dedecek, J.; Capek, L.; Wichterlova, B. *Applied Catalysis A: General* **2006**, *307*, 156-164.

61. Langmi, H. W.; Book, D.; Walton, A.; Johnson, S. R.; Al-Mamouri, M. M.; Speight, J. D.; Edwards, P. P.; Harris, I. R.; Anderson, P. A. *Journal of Alloys and Compounds* **2005**, *404-406*, 637-642.

62. Ramirez-Cuesta, A. J. M., P. C. H. *Catalysis Today* **2007**, *120*, 368-373.

63. Kuwahara, Y. K., Takashi; Mori, Kohsuke; Matsumura, Yasuyuki; Yamashita, Hiromi. . *Topics in Catalysis* **2009**, *52*, 643-648.

64. Huang, L.; Xiao, H.; Ni, Y. *Separation and Purification Technology* **2006**, *49*, 264-270.

65. Smaiehi, M. G., Elisabeth; Durand, Jean-Olivier; Valtchev, Valentin P. *Journal of Materials Chemistry* **2004**, *14*, 1347-1351.

66. Zhang, X. L., Emily Sau Man; Martin-Aranda, Rosa; Yeung, King Lun. . *Applied Catalysis, A: General* **2004**, *261*, 109-118.

67. Zhang, X.-Y.; Wang, Q.-C.; Zhang, S.-Q.; Sun, X.-J.; Zhang, Z.-S. *Journal of Hazardous Materials* **2009**, *168*, 1575-1580.

68. Le-khac, B., *Direct epoxidation catalyst and process*. 2008.

69. Nishimura, G. S., Yasuhiro; Hirai, Takayuki. *Industrial & Engineering Chemistry Research* **2004**, *43*, 6064-6069.

70. Li, D. Y., Jianfeng; Wang, Huanting; Hao, Na; Zhao, Dongyuan; Ratinac, Kyle R.; Ringer, Simon P. *Microporous and Mesoporous Materials* **2007**, *106*, 262-267.

71. Wang, Y. L., Huanrong; Zhang, Wenjun; Liu, Binyuan. *Materials Letters* **2008**, *62*, 3167-3170.

72. Valentín, J. L.; López-Manchado, M. A.; Posadas, P.; Rodríguez, A.; Marcos-Fernández, A.; Ibarra, L. *Journal of Colloid and Interface Science* **2006**, *298*, 794–804

73. Sagiv, J. *Journal of the American Chemical Society* **1980**, *101*, 92-98.

74. Vassylyev, O.; Hall, G. S.; Khinast, J. G. *Journal of Porous Materials* **2006**, 5-11.

75. Cheng, C.-H.; Bae, T.-H.; McCool, B. A.; Chance, R. R.; Nair, S.; Jones, C. W. *Journal of Physical Chemistry C* **2008**, *112*, 3543-3551.

76. Mix, H.; Pfeifer, H.; Staudte, B. *Chemical Physics Letters* **1988**, *146*, 541-544.

77. Zhuravlev, L. T. *Colloids and Surfaces, A: Physicochemical and Engineering Aspects* **2000**, *173*, 1-38.

78. Antochshuk, V.; Jaroniec, M. *Chemistry of Materials* **2000**, *12*, 2496-2501.

79. Zhan, B.-Z.; White, M. A.; Fancy, P.; Kennedy, C. A.; Lumsden, M. *Macromolecules* **2004**, *37*, 2748-2753.

80. Sen, T.; Jana, S.; Koner, S.; Patra, A. *Journal of Physical Chemistry C* **2010**, *114*,

81. Pecharsky, V. K.; Zavalij, P. Y., *Fundamentals of powder diffraction and structural characterization of materials*. 2005, New York: Springer.

82. Patterson, A. L. *Physical Reviews* **1939**, *56*, 978–982.

83. Materials, A. S. f. T. a., *Standard Test Method for Determination of Relative Crystallinity of Zeolite ZSM-5 by X-Ray Diffraction.* 2001.

84. Brunauer, S.; Emmett, P. H.; Teller, E. *Journal of the American Chemical Society* **1938**, *60*, 309-319.

85. Lippens, B. C. d. B., J. H. *Journal of Catalysis* **1965**, *4*, 319-323.

86. Barrett, E. P.; Joyner, L. G.; Halenda, P. P. *Journal of the American Chemical Society* **1951**, *73*, 373-380.

87. Gore, K. U.; Abraham, A.; Hegde, S. G.; Kumar, R.; Amoureux, J.-P.; Ganapathy, S. *Journal of Physical Chemistry B* **2002**, *106*, 6115-6120.

88. Jiao, J.; Kanellopoulos, J.; Wang, W.; Ray, S. S.; Foerster, H.; Freude, D.; Hunger, M. *Physical Chemistry Chemical Physics* **2005**, *7*, 3221-3226.

89. Abraham, A.; Prins, R.; van Bokhoven, J. A.; van Eck, E. R. H.; Kentgens, A. P. M. *Solid State Nuclear Magnetic Resonance* **2009**, *35*, 61-66.

90. Biaglow, A. I.; Sepa, J.; Gorte, R. J.; White, D. *Journal of Catalysis* **1995**, 373-384.

91. Abubakar, S. M.; Lee, J. C.; Marcus, D. M.; Ehresmann, J. O.; Haw, J. F. *Journal of Physical Chemistry B* **2006**, *110*, 14598-14603.

92. Mermet, J. M. *Journal of Analytical Atomic Spectroscopy* **2005**, *20*, 11-16.

93. Mintova, S.; Valtchev, V.; Onfroy, T.; Marichal, C.; Knözinger, H.; Bein, T. *Microporous and Mesoporous Materials* **2006**, *90*, 237-245.

94. Kotrel, S.; Rosynek, M. P.; Lunsford, J. H. *Journal of Catalysis* **2000**, *191*, 55-61.

95. Yan, H. T.; Le Van Mao, R. *Applied Catalysis A: General* **2010**, *375*, 63-69.

96. Liu, C.; Deng, Y.; Pan, Y.; Gu., Y.; Qiao, B.; Gao, X. *Journal of Molecular Catalysis A: Chemical* **2004**, *215*, 195-199.

97. Liu, C. *Journal of Molecular Catalysis A: Chemical* **2004**, *215*, 195-199.

98. Aboul-Gheit, A. K.; Awadallah, A. E.; Aboul-Gheit, N. A. K.; Solyman, E.-S. A.; Abdel-Aaty, M. A. *Applied Catalysis A: General* **2008**, *334*, 304-310.

99. Modhera, B.; Chakraborty, M.; Parikh, P. A.; Bajaj, H. C. *Catalysis Letters* **2009**, *132*, 168-173.

100. Ding, L.; Zheng, Y.; Yang, H.; Parviz, R. *Applied Catalysis A: General* **2009**, *353*, 17-23.

101. Tosheva, L., Valtchev, V. *Chemistry of Materials* **2005**, *17*,

102. Serrano, D. P.; van Grieken, R.; Melero, J. A.; García, A.; Vargas, C. *Journal of Molecular Catalysis A: Chemical* **2010**, *318*, 68-74.

103. Choi, M.; Na, K.; Kim, J.; Sakamoto, Y.; Terasaki, O.; Ryoo, R. *Nature* **2009**, *461*, 246-249.

104. Firoozi, M.; Baghalha, M.; Asadi, M. *Catalysis Communications* **2009**, *10*, 1582-1585.

105. Kim, J.; Choi, M.; Ryoo, R. *Journal of Catalysis* **2010**, *269*, 219-228.

106. Pérez-Ramírez, J.; Abelló, S.; Bonilla, A.; Groen, J. C. *Advanced Functional Materials* **2009**, *19*, 164-172.

107. de A. A. Soler-Illia, G. J.; Clement, S.; Benedicte, L.; Joel, P. *Chemistry Reviews* **2002**, *102*, 4093–4138.

108. Caicedo-Realpe, R.; Pérez-Ramírez, J. *Microporous and Mesoporous Materials* **2010**, *128*, 91-100.

109. Ogura, M. *Catalysis Surveys from Asia* **2008**, *12*, 16-27.

110. Park, J.-N.; Wang, J.; Hong, S.-I.; Lee, C. W. *Applied Catalysis A: General* **2005**, *292*, 68-75.

111. Ogura, M.; Shinomiya, S.; Tateno, J.; Nara, Y.; Nomura, M.; Kikuchi, E.; Matsukata, M. *Applied Catalysis A: General* **2001**, *219*, 33-43.

112. Groen, J. C.; Abelló, S.; Villaescusa, L. A.; Pérez-Ramírez, J. *Microporous and Mesoporous Materials* **2008**, *114*, 93-102.

113. Verboekend, D.; Groen, J. C.; Pérez-Ramírez, J. *Advanced Functional Materials* **2010**, *20*, 1441-1450.

114. Mohr, G. D.; Janssen, M. J. G. 2001: US.

115. Tong, Y.; Zhao, T.; Li, F.; Wang, Y. *Chemistry of Materials* **2006**, *18*, 4218-4220.

116. Valtchev, V. P.; Smaihi, M.; Faust, A.-C.; Vidal, L. *Chemistry of Materials* **2004**, *16*, 1350-1355.

117. Lei, Q.; Zhao, T.; Li, F.; Wang, Y. F.; Hou, L. *Journal of Porous Materials* **2007**, *15*, 643-646.

118. Zhu, H.; Liu, Z.; Kong, D.; Wang, Y.; Yuan, X.; Xie, Z. *Journal of Colloid and Interface Science* **2009**, *331*, 432-438.

119. Xin, H.; Koekkoek, A.; Yang, Q.; van Santen, R.; Li, C.; Hensen, E. J. M. *Chemical Communications* **2009**, 7590.

120. Li, C.; Wang, Y.; Shi, B.; Ren, J.; Liu, X.; Guo, Y.; Lu, G. *Microporous and Mesoporous Materials* **2009**, *117*, 104-110.

121. Bagshaw, S. A.; Baxter, N. I.; Brew, D. R. M.; Hosie, C. F.; Yuntong, N.; Jaenicke, S.; Khuan, C. G. *Journal of Materials Chemistry* **2006**, *16*, 2235.

122. Xu, H.; Guan, J.; Wu, S.; Kan, Q. *Journal of Colloidal and Interface Science* **2009**, *329*, 346-350.

123. Aguado, J.; Serrano, D. P.; Rodríguez, J. M. *Microporous and Mesoporous Materials* **2008**, *115*, 504-513.

124. Srivastava, R.; Iwasa, N.; Fujita, S.; Arai, M. *Chemistry - A European Journal* **2008**, *14*, 9507-9511.

125. Serrano, D. P.; Aguado, J.; Morales, G.; Rodriguez, J. M.; Peral, A.; Thommes, M.; Epping, J. D.; Chmelka, B. F. *Chemistry of Materials* **2009**, *21*, 641-654.

126. Fang, Y.; Hu, H.; Chen, G. *Chemistry of Materials* **2008**, *20*, 1670-1672.

127. Liu, S.-P.; Chen, L.; Wang, Y. M. *Solid State Science* **2010**, *12*, 1070-1075.

128. Tao, Y.; Kanoh, H.; Abrams, L.; Kaneko, K. *Chemical Reviews* **2006**, 896-910.

129. Majano, G.; Darwiche, A.; Mintova, S.; V., V. *Industrial and Engineering Chemistry Research* **2009**, *48*, 7084-7091.

130. Serrano, D. P.; Aguado, J.; Escola, J. M.; Rodriguez, J. M.; Peral, A. *Chemistry of Materials* **2006**, *18*, 2462-2464.

131. Oldfield, E.; Haase, J.; Schmitt, K. D.; Schramm, S. E. *Zeolites* **1994**, *14*, 101-109.

132. Alma, N. C. M.; Hays, G. R.; Samoson, A. V.; Lippmaa, E. T. *Analytical Chemistry* **1984**, *56*, 729-733.

133. Petushkov, A.; Yoon, S.; Larsen, S. C. *Microporous and Mesoporous Materials* **2010**, *137*, 92-100.

134. Bourgeat-Lami, E.; Massiani, P.; Renzo, F. D.; Fajula, F.; Courrieres, T. D. *Catalysis Letters* **1990**, *5*, 265-272.

135. de Menorval, L. C.; Buckermann, W.; Figueras, F.; Fajula, F. *Journal of Physical Chemistry* **1996**, *100,* 465-467.

136. Kunkeler, P. J.; Zuurdeeg, B. J.; van der Waal, J. C.; van Bokhoven, J. A.; Koningsberger, D. C.; van Bekkum, H. *Journal of Catalysis* **1998**, *180,* 234-244.

137. Hould, N. D.; Kumar, S.; Tsapatsis, M.; Nikolakis, V.; Lobo, R. F. *Langmuir* **2010**, *26,* 1260-1270.

138. Kuechl, D. E.; Benin, A. I.; Knight, L. M.; Abrevaya, H.; Wilson, S. T.; Sinkler, W.; Mezza, T. M.; Willis, R. R. *Microporous and Mesoporous Materials* **2010**, *127,* 104-118.

139. Colombo, M.; Nova, I.; Tronconi, E. *Catalysis Today* **2010**, *151,* 223-230.

140. Li, G. H.; Jones, C. A.; Grassian, V. H.; Larsen, S. C. *Journal of Catalysis* **2005**, *235,* 431.

141. Keane, M. A. *Microporous Materials* **1996**, *7,* 51-59.

142. Wang, H. F.; Huff, T. B.; Zweifel, D. A.; He, W.; Low, P. S.; Wei, A.; Cheng, J. X. *Proceedings of the National Academy of Sciences of the United States of America* **2005**, *102,* 15752.

143. El-Sayed, I. H.; Huang, X. H.; El-Sayed, M. A. *Nano Letters* **2005**, *5,* 829.

144. Salem, A. K.; Hung, C. F.; Kim, T. W.; Wu, T. C.; Searson, P. C.; Leong, K. W. *Nanotechnology* **2005**, *16,* 484.

145. Salem, A. K.; Searson, P. C.; Leong, K. W. *Nature Materials* **2003**, *2,* 668.

146. Salem, A. K.; Chen, M.; Hayden, J.; Leong, K. W.; Searson, P. C. *Nano Letters* **2004**, *4,* 1163.

147. Kralj, M. *Periodicum Biologorum* **2003**, *105,* 99.

148. Kralj, M.; Pavelic, K. *EMBO Reports* **2003**, *4,* 1008.

149. Pavelic, K.; Hadsija, M.; Bedrica, L.; Pavelic, J.; Dikic, I.; Katic, M.; Kralj, M.; Bosnar, M.; Kapitanovic, S.; Poljak-Blazi, M.; Krizanac, S.; Stojkovic, R.; Jurin, M.; Subotic, B.; Colic, M. *Journal of Molecular Medicine* **2001**, *78,* 708.

150. Pearce, M. E.; Mai, H. Q.; Lee, N.; Larsen, S. C.; Salem, A. K. *Nanotechnology* **2008**, *19,* 175103.

151. Trewyn, B. G.; Giri, S.; Slowing, I. I.; Lin, V. S. Y. *Chemical Communications* **2007**, 3236.

152. Tsai, C. P.; Hung, Y.; Chou, Y. H.; Huang, D. M.; Hsiao, J. K.; Chang, C.; Chen, Y. C.; Mou, C. Y. *Small* **2008**, *4,* 186.

153. Matheoud, R.; Secco, C.; Ridone, S.; Inglese, E.; Brambilla, M. *Physics in Medicine and Biology* **2008**, *53,* N137.

154. Li, W. S.; Li, Z. F.; Jing, F. Y.; Yang, X. G.; Li, X. J.; Pei, F. K.; Wang, X. X.; Lei, H. *Acta Chimica Sinica* **2007**, *65*, 2029.

155. Balkus, K. J.; Shi, J. M. *Langmuir* **1996**, *12*, 6277.

156. Lin, Y. S.; Hung, Y.; Su, J. K.; Lee, R.; Chang, C.; Lin, M. L.; Mou, C. Y. *Journal of Physical Chemistry B* **2004**, *108*, 15608.

157. Colvin, V. L. *Nature Biotechnology* **2003**, *21*, 1166.

158. Li, G. H.; Larsen, S. C.; Grassian, V. H. *Catalysis Letters* **2005**, *103*, 23.

159. Li, G. H.; Larsen, S. C.; Grassian, V. H. *Journal of Molecular Catalysis A: Chem.* **2005**, *227*, 25.

160. Breck, D. W., *Zeolite Molecular Sieves: Structure, Chemistry, and Use*. 3rd Print edition ed. 1974, New-York: John Wiley & Sons Inc.

161. Galownia, J.; Martin, J.; Davis, M. E. *Microporous and Mesoporous Materials* **2006**, *92*, 61.

162. Bresinska, I.; Balkus, K. J. *Journal of Physical Chemistry* **1994**, *98*, 12989.

163. Young, S. W.; Qing, F.; Rubin, D.; Balkus, K. J.; Engel, J. S.; Lang, J.; Dow, W. C.; Mutch, J. D.; Miller, R. A. *Journal of Magnetic Resonance Imaging* **1995**, *5*, 499.

164. Platas-Iglesias, C.; Elst, L.; Zhou, W.; Muller, R. N.; Geraldes, C.; Maschmeyer, T.; Peters, J. A. *Chemistry - A European Journal* **2002**, *8*, 5121.

165. Huh, S.; Wiench, J. W.; Trewyn, B. G.; Song, S.; Pruski, M.; Lin, V. S. Y. *Chemical Communications* **2003**, 2364.

166. Liong, M.; Lu, J.; Kovochich, M.; Xia, T.; Ruehm, S. G.; Nel, A. E.; Tamanoi, F.; Zink, J. I. *ACS Nano* **2008**, *2*, 889.

167. Rieter, W. J.; Kim, J. S.; Taylor, K. M. L.; An, H. Y.; Lin, W. L.; Tarrant, T.; Lin, W. B. *Angewandte Chemie International Edition* **2007**, *46*, 3680.

168. Slowing, I. I.; Trewyn, B. G.; Giri, S.; Lin, V. S. Y. *Advanced Functional Materials* **2007**, *17*, 1225.

169. Song, W.; Woodworth, J. F.; Grassian, V. H.; Larsen, S. C. *Langmuir* **2005**, *21*, 7009.

170. Barquist, K.; Larsen, S. C. *Microporous and Mesoporous Materials* **2008**, *116*, 365.

171. Zhan, B. Z.; White, M. A.; Lumsden, M. *Langmuir* **2003**, *19*, 4205.

172. Lerouge, F.; Melnyk, O.; Durand, J.-O.; Raehm, L.; Berthault, P.; Huber, G.; Desvaux, H.; Constantinesco, A.; Choquet, P.; Detour, J.; Smaïhi, M. *Journal of Materials Chemistry* **2009**, *19*, 379.

173. Lew, C. M.; Li, Z. J.; Li, S.; Hwang, S. J.; Liu, Y.; Medina, D. I.; Sun, M. W.; Wang, J. L.; Davis, M. E.; Yan, Y. S. *Advanced Functional Materials* **2008**, *18*, 3454.

174. Fenoglio, I.; Croce, A.; Di Renzo, F.; Tiozzo, R.; Fubini, B. *Chemical Research in Toxicology* **2000**, *13*, 489-500.

175. Fubini, B.; Zanetti, G.; Altilia, S.; Tiozzo, R.; Lison, D.; Saffiotti, U. *Chemical Research in Toxicology* **1999**, *12*, 737.

176. Fubini, B. *Environmental Health Perspectives* **1997**, *105*, 1013.

177. Fubini, B. *Annals of Occupational Hygiene* **1998**, *42*, 521.

178. Fubini, B.; Arean, C. O. *Chemical Society Reviews* **1999**, *28*, 373.

179. Elias, Z.; Poirot, O.; Daniere, M. C.; Terzetti, F.; Marande, A. M.; Dzwigaj, S.; Pezerat, H.; Fenoglio, I.; Fubini, B. *Toxicology in Vitro* **2000**, *14*, 409.

180. Giovine, M.; Pozzolini, M.; Fenoglio, I.; Scarfi, S.; Ghiazza, M.; Benatti, U.; Fubini, B. *Toxicology and Industrial Health* **2002**, *18*, 249.

181. Donaldson, K.; Borm, P. J. A. *Annals of Occupational Hygiene* **1998**, *42*, 287.

182. Grce, M.; Pavelic, K. *Microporous and Mesoporous Materials* **2005**, *79*, 165.

183. Giri, S.; Trewyn, B. G.; Stellmaker, M. P.; Lin, V. S. Y. *Angewandte Chemie International Edition* **2005**, *44*, 5038.

184. Radu, D. R.; Lai, C. Y.; Jeftinija, K.; Rowe, E. W.; Jeftinija, S.; Lin, V. S. Y. *Journal of the American Chemical Society* **2004**, *126*, 13216.

185. Chung, T. H.; Wu, S. H.; Yao, M.; Lu, C. W.; Lin, Y. S.; Hung, Y.; Mou, C. Y.; Chen, Y. C.; Huang, D. M. *Biomaterials* **2007**, *28*, 2959.

186. Di Pasqua, A. J.; Sharma, K. K.; Shi, Y. L.; Toms, B. B.; Ouellette, W.; Dabrowiak, J. C.; Asefa, T. *Journal of Inorganic Biochemistry* **2008**, *102*, 1416.

187. Tao, Z. M.; Morrow, M. P.; Asefa, T.; Sharma, K. K.; Duncan, C.; Anan, A.; Penefsky, H. S.; Goodisman, J.; Souid, A. K. *Nano Letters* **2008**, *8*, 1517.

188. Slowing, I.; Trewyn, B. G.; Lin, V. S. Y. *Journal of the American Chemical Society* **2006**, *128*, 14792.

189. Song, W.; Justice, R. E.; Jones, C. A.; Grassian, V. H.; Larsen, S. C. *Langmuir* **2004**, *20*, 4696.

190. Maynard, A. D.; Aitken, R.; Butz, T.; Colvin, V. L.; Donaldson, K.; Oberdorster, G.; Philbert, M.; Ryan, J.; Seaton, A.; Stone, V.; Tinkle, S.; tran, L.; Walker, N.; Warheit, D. *Nature* **2006**, *444*, 267.

191. Sayes, C. M.; Wahi, R.; Kurian, P.; Liu, Y.; West, J.; Ausman, K.; Warheit, D.; Colvin, V. L. *Toxicological Sciences* **2006**, *92*, 174.

192. Lewinski, N.; Colvin, V.; Drezek, R. *Small* **2008**, *4*, 26-49.

193. Warheit, D. *Toxicological Sciences* **2008**, *101*, 183.

194. Kanduc, D.; Mittelman, A.; Serpico, R.; Sinigaglia, E.; Sinha, A. A.; Natale, C.; Santacroce, R.; Di Corcia, M. G.; Lucchese, A.; Dini, L.; Pani, P.; Santacroce, S.; Simone, S.; Bucci, R.; Farber, E. *International Journal of Oncology* **2002**, *21*, 165.

195. Proskuryakov, S. Y.; Gabai, V. L.; Konoplyannikov, A. G.; Zamulaeva, I. A.; Kolesnikova, A. I. *Biochemistry (Moscow)* **2005**, *70*, 1310.

196. Li, H., ;; van Berlo, D.; Shi, T.; Speit, G.; Knaapen, A. M.; Borm, P. J. A.; Albrecht, C.; Schins, R. P. F. *Toxicology and Applied Pharmacology* **2008**, *227*, 115-124.

197. Singh, R. J.; Karoui, H.; Gunter, M. R.; Beckman, J. S.; Mason, R. P.; Kalyanarman, B. *Proceedings of the National Academy of Sciences of the United States of America* **1998**, *95*, 6675-6680.

198. Shi, X.; Dalal, N. S.; Vallyathan, V. *Journal of Toxicology and Environmental Health* **1988**, *25*, 237-245.

199. Vallyathan, V.; Shi, X.; Dalal, N. S.; Irr, W.; Castranova, V. *American Review of Respiratory Disease* **1988**, *138*, 1213-1219.

200. Lison, D.; Thomassen, L. C. J.; Rabolli, V.; Gonzalez, L.; Napierska, D.; Seo, J. W.; Kirsch-Volders, M.; Hoet, P.; Kirschhock, C. E. A.; Martens, J. A. *Toxycological Sciences* **2008**, *104*, 155.

201. Oberdorster, G.; Oberdorster, E.; Oberdorster, J. *Environmental Health Perspectives* **2005**, *113*, 823.

202. Schins, R. P. F.; Duffin, R.; Hohr, D.; Knaapen, A. M.; Shi, T. M.; Weishaupt, C.; Stone, V.; Donaldson, K.; Borm, P. J. A. *Chemical Research in Toxicology* **2002**, *15*, 1166.

203. Marquis, B. J.; Love, S. A.; Braun, K. L.; Haynes, C. H. *Analyst* **2009**, *134*, 425.

204. Marsh, M.; McMahon, H. T. *Science* **1999**, *285*, 215.

205. Waters, K. M.; Masiello, L. M.; Zangar, R. C.; Karin, N. J.; Quesenberry, R. D.; Bandyopadhyay, S.; Teeguarden, J. G.; Pounds, J. G.; Thrall, B. D. *Toxicological Sciences* **2009**, *107*, 553.

206. Intra, J.; Glasgow, J. A.; Mai, H. Q.; Salem, A. K. *Journal of Controlled Release* **2008**, *127*, 280.

207. Intra, J.; Salem, A. K. *Journal of Controlled Release* **2008**, *130*, 129.

208. Zhang, X. Q.; Dahle, C. E.; Weiner, G. J.; Salem, A. K. *Journal of Pharmaceutical Sciences* **2007**, *96*, 3283.

209. Zhang, X. Q.; Intra, J.; Salem, A. K. *Bioconjugate Chemistry* **2007**, *18*, 2068.

210. Zhang, X. Q.; Intra, J.; Salem, A. K. *Journal of Microencapsulation* **2008**, *25*, 1.

211. Borutaite, V.; Brown, G. C. *Free Radical Biology and Medicine* **2003**, *35*, 1457.

212. Kumar, K. S.; Singh, V. K.; Jackson, W.; Seed, T. M. *Experimental and Molecular Pathology* **2003**, *74*, 68.

213. Zamora, R.; Matthys, K. E.; Herman, A. G. *European Journal of Pharmacology* **1997**, *321*, 87.

214. Ryman-Rasmussen, J. P.; Riviere, J. E.; Monteiro-Riviere, N. A. *Journal of Investigative Dermatology* **2007**, *127*, 143.

215. Clift, M. J. D.; Rothen-Rutishauser, B.; Brown, D. M.; Duffin, R.; Donaldson, K.; Proudfoot, L.; Guy, K.; Stone, V. *Toxycology and Applied Pharmacology* **2008**, *232*, 418.

216. Park, E. J.; Park, K. *Toxicology Letters* **2009**, *184*, 18.

217. Reitmeier, S. J.; Gobin, O. C.; Jentys, A.; Lercher, J. A. *Angewandte Chemie International Edition* **2009**, *48*, 533-538.

218. Tang, Z.; Dong, J.; Nenoff, T. M. *Langmuir* **2009**, *25*, 4848-4852.

219. Zou, W.; Han, R.; Chen, Z.; Jinghua, Z.; Shi, J. *Colloids and Surfaces A: Physicochemical and Engineering Aspects* **2006**, *279*, 238-246.

220. Haiyan, W.; Jing, Z.; Guojing, C.; Liang, Z.; Min, W.; Jun, M. *Petroleum Science and Technology* **2008**, *26*, 499-506.

221. Liu, Q.; Wang, T.; Qiu, J.; Cao, Y. *Chemical Communications* **2006**, 1230.

222. Doussineau, T.; Smaïhi, M.; Balme, S.; Janot, J.-M. *ChemPhysChem* **2006**, *7*, 583-589.

223. Huang, Y.; Shan, W.; Liu, B.; Liu, Y.; Zhang, Y.; Zhao, Y.; Lu, H.; Tang, Y.; Yang, P. *Lab on a Chip* **2006**, *6*, 534.

224. Panyam, J.; Labhasetwar, V. *Advanced Drug Delivery Reviews* **2003**, *55*, 329-347.

225. Petushkov, A.; Intra, J.; Graham, J. B.; Larsen, S. C.; Salem, A. K. *Chemical Research in Toxicology* **2009**, *22*, 1359-1368.

226. Inagaki, S.; Ogura, M.; Inami, T.; Sasaki, Y.; Kikuchi, E.; Matsukata, M. *Microporous and Mesoporous Materials* **2004**, *74*, 163-170.

227. Tanaka, S.; Nakatani, N.; Miyake, Y. *Chemistry Letters* **2009**, *38*, 780-781.

228. Cruciani, G. *Journal of Physics and Chemistry of Solids* **2006**, *67*, 1973-1994.

229. Greaves, G. N.; Meneau, F.; Sankar, G. *Nuclear Instruments and Methods in Physics Research Section B* **2009**, *199*, 98-105.

230. Xu, M.; Liu, X.; Mason, R. J. *Journal of Catalysis* **2002**, *207*, 237-246.

231. Cizmek, A.; Komunjer, L.; Subotic, B.; Siroki, M.; Roncevic, S. *Zeolites* **1991**, *11*, 258-264.

232. Cizmek, A.; Komunjer, L.; Subotic, B.; Siroki, M.; Roncevic, S. *Zeolites* **1991**, *11*, 810-815.

233. Cizmek, A.; Komunjer, L.; Subotic, B.; Siroki, M.; Roncevic, S. *Zeolites* **1992**, *12*, 190-196.

234. Hartman, R. L.; Fogler, H. S. *Industrial & Engineering Chemistry Research* **2005**, *44*, 7738-7745.

235. Hartman, R. L.; Fogler, H. S. *Langmuir* **2007**, *23*, 5477-5484.

236. Larsen, S.; Grassian, V.; Song, W.; Li, G. 2009: US.

237. Baltrusaitis, J.; Usher, C. R.; Grassian, V. H. *Physical Chemistry Chemical Physics* **2007**, *9*, 3011-3024.

238. Klinowski, J. *Chemical Reviews* **1991**, *91*, 1459-1479.

239. Zhuang, J.; Ma, D.; Yang, G.; Yan, Z.; Liu, X.; Han, X.; Bao, X.; Xie, P.; Liu, Z. *Journal of Catalysis* **2004**, *228*, 234-242.

240. Chen, T.-H.; Wouters, B. H.; Grobet, P. J. *Eur. J. Inorg. Chem.* **2000**, 281-285.